

**ANALYSIS OF CHARGED AEROSOLS IN THE MESOSPHERE DURING THE MASS/ECOMA
ROCKET CAMPAIGN**

By

SCOTT ROBERT KNAPPMILLER

B.S. & B.A., UNIVERSITY OF COLORADO AT BOULDER, 2004

A thesis submitted to the
Faculty of the Graduate School of the
University of Colorado in partial fulfillment
of the requirements for the degree of
Doctor of Philosophy
Department of Physics

2010

This thesis entitled:
Analysis of Charged Aerosol Particles in the Mesosphere during the MASS/ECOMA
Rocket Campaign
written by Scott Robert Knappmiller
has been approved for the
Department of Physics

(Scott Robertson)

(Zoltan Sternovsky)

Date _____

The final copy of this thesis has been examined by the signatories, and we find that both the content and the form meet acceptable presentation standards of scholarly work in the above-mentioned discipline.

ABSTRACT

Scott Knappmiller (Ph.D. Physics)

Analysis of Charged Aerosol Particles in the Mesosphere during the MASS/ECOMA
Rocket Campaign

Directed by Scott Robertson, Professor, Department of Physics, University of Colorado
at Boulder

In the polar summer mesosphere ice particles grow sufficiently large to scatter sunlight, giving rise to visible cloud displays called Noctilucent Clouds (NLC). In August of 2007, two sounding rockets were launched from the Andoya Rocket Range, Norway carrying the newly developed MASS instrument (Mesospheric Aerosol Sampling Spectrometer) to study NLC. The instrument detects charged aerosols in four different mass ranges on four pairs of biased collector plates, one set for positive particles and one set for negative particles. The first sounding rocket was launched into a Polar Mesospheric Summer echo (PMSE) and into a NLC on 3 August. The solar zenith angle was 93 degrees and NLC were seen in the previous hour at 83 km by the ALOMAR RMR lidar. NLC were also detected at the same altitude by rocket-borne photometer measurements. The data from the MASS instrument shows a negatively charged population with radii >3 nm in the 83-89 km altitude range, which is collocated with PMSE detected by the ALWIN radar. Smaller particles, 1-2 nm in radius with both positive and negative polarity were detected between 86-88 km. Positively charged

particles <1 nm in radius were detected at the same altitude. This is the first time the charge number densities of positive and negative NLC particles have been measured simultaneously.

A charging model is developed to investigate the coexistence of positively and negatively charged aerosols in the NLC environment as measured by the MASS instrument. Natanson's rate equations are used for the attachment of free electrons and ions and the model includes charging by photo-electron emission and photo-detachment. Although the MASS flight occurred during twilight conditions, the solar UV flux was still sufficient to affect the charge state of the aerosols. The calculations are done assuming three types of particles with different photo-electron charging properties: 1) Icy NLC particles, 2) Hematite particles of meteoric origin as condensation nuclei, and 3) Hematite particles coated with ice. The charge model results are consistent with the MASS rocket data, displaying both positively and negatively charged aerosols for small radii and only negatively charged particles for large radii.

ACKNOWLEDGEMENTS

The work covered in this thesis would not have been possible without funding from NASA to develop and launch the Mesospheric Aerosol Sampling Spectrometer (MASS) instrument. In addition, I am grateful to have received the NASA Earth and Space Science Fellowship, which allowed me the freedom to focus on my research interests as well as travel internationally for scientific collaborations. I owe my deepest gratitude to my advisor, Professor S. Robertson, for giving me the great opportunity to join his lab. Professor S. Robertson's encouragement and guidance over the years was crucial to my learning and training while also making my experience at the University of Colorado very enjoyable. I would like to show my gratitude to Professor Z. Sternovsky for his endless support and advice in the laboratory. I am indebted to Dr. M. Rapp for the opportunity to spend a summer working at the Institute for Atmospheric Physics in Kuhlungsborn, Germany. I am also grateful for the many fruitful discussions with Dr. M. Rapp and Dr. J. Gumbel regarding my numerical charge model. It has been an honor for me to have worked on the MASS rocket campaign with R. Kohnert and W. Handley. I also need to thank Professor M. Horanyi, Professor C. Randall, and Professor T. Munsat for serving on my thesis committee and providing additional feedback and guidance. Rocket campaigns and graduate research require many collaborators, so I offer my regards and blessings to everyone else who supported me during my graduate career including the rest of the Robertson lab. I am grateful to be surrounded by such a loving and caring set of friends and family. I am especially thankful for A. Light, A. Poppe and C. Bauer's assistance and friendship during our time at the University of Colorado. Lastly, I would like to thank my girlfriend, Micaela, for her devotion and patience throughout this project.

TABLE OF CONTENTS

CHAPTER 1: NOCTILUCENT CLOUDS	1
1.1 NLC Nucleation	2
1.2 NLC Measurement Techniques	6
1.3 The Present Study	8
CHAPTER 2: The MASS Instrument.....	11
2.1 Mechanical Design.....	12
2.2 Electrical Design.....	15
2.3 Laboratory Calibration.....	18
2.4 Numerical Calibration.....	20
2.4.1 <i>Electric Field</i>	20
2.4.2 <i>Direct Simulation Monte Carlo Model</i>	21
2.4.3 <i>Particle Trajectory Program</i>	25
2.5 Numerical Calibration Results.....	31
CHAPTER 3: MASS FLIGHT DATA	37
3.1 MASS Payload	37
3.1.1 <i>Faraday Rotation Antennas</i>	38
3.1.2 <i>Colorado Dust Detectors</i>	41
3.1.3 <i>Electric Field Booms</i>	42

3.1.4 <i>Photometer</i>	42
3.2 MASS Launch Site.....	43
3.3 MASS Flight 1 Data.....	44
3.3.1 <i>Channels 1+ and 1-</i>	46
3.3.2 <i>Channels 2+ and 2-</i>	50
3.3.3 <i>Channels 3+ and 3-</i>	52
3.3.4 <i>Channels 4+ and 4-</i>	53
3.4 MASS Flight 2 Data.....	56
3.4.1 <i>Upleg Data: Channels 1± through 4±</i>	57
3.4.2 <i>Downleg Data: Channels 1± through 4±</i>	60
3.5 Quasi-neutrality Check	61
3.6 Photometer Data	64
3.7 Comparison to SOFIE Limb Scans.....	66
3.8 MASS Flight Performance	68
3.8.1 <i>Microphonic Noise</i>	69
3.8.2 <i>Spurious Charge Generation</i>	69
3.8.3 <i>Photoelectric Currents</i>	70
3.9 MASS Data Discussion and Conclusions	71
CHAPTER 4: CHARGE MODEL.....	73
4.1 Kinetic charge model.....	76
4.1.1 <i>Electron and ion attachment coefficients</i>	79
4.1.2 <i>Photodetachment and photoemission rates</i>	81

4.2 Low aerosol density results	85
4.2.1 <i>IceParticles</i>	85
4.2.2 <i>Meteoric Smoke Particles</i>	88
4.2.3 <i>Composite particles</i>	89
4.3 High aerosol density results	92
4.3.1 <i>Pure ice Particles</i>	93
4.3.2 <i>Composite particles</i>	95
4.4 Conclusion and Discussion	97
CHAPTER 5: CONCLUSION AND DISCUSSION	100
BIBLIOGRAPHY	103
Appendix A: Aerodynamic Simulation Results	112
Appendix B: MASS Calibration Results	115

LIST OF TABLES

Table 1. DSMC simulations were done at six altitudes. The initial conditions for each simulation are listed above. The velocity is the averaged rocket velocity from the two MASS launches. The density and temperature values are interpolated values from Lübken [1999] and then averaged over the two launch dates.	23
Table 2. Numerical calibration results at 6 altitudes with and without a payload potential of -1 V. The plate numbers correspond to the graphite collection plates where 1 is the top collection plate in the MASS instrument. The last line in the table is the laboratory calibration results.	33

LIST OF FIGURES

- Figure 1. Photograph of MASS instrument (left) and mechanical drawing of the MASS instrument (right). Both images have a set of graphite plates removed to show the inside of the instrument. The mechanical drawing includes a set of mesh grid holders on the air exit windows, which are biased to prevent electron and ion collection..... 12
- Figure 2. Circuit diagrams for the current to voltage electronics used in the MASS instrument. Circuit I is for the second, third and fourth graphite collection plates. Circuit II has two gains and is for the first collection plate. 16
- Figure 3. Experimental calibration curves for the MASS instrument. A laboratory calibration was performed using an argon ion source simulating the charged aerosols particles in the mesosphere. The numbers 2, 3, and 4 refer to the graphite collection plates as numbered from the top of the instrument. 19
- Figure 4. The above plot displays the potential contours in the MASS instrument and lists the voltages on the collection plates. The instrument is viewed on its side such that the top of the instrument is on the right and the bottom on the left. 21
- Figure 5. This shows the results of the DSMC computer model for the (A) air number density, (B) the air temperature, and (C) the air flow velocity in and around the MASS instrument for conditions at 85km. 24

Figure 6. Trajectories of particles within the MASS instrument for four different masses each with four different initial spatial coordinates and thermal velocities. The masses were selected to have a high probability of being collected. They alternate in polarity: $M = 30$ amu and $M = 11,000$ are positive, while $M = 1500$ and $M = 90,000$ are negative. A large fraction of the 30 amu particles are lost to the wall before collection due to their high thermal velocity or collisions..... 31

Figure 7. Engineering drawing of the forward payload section consisting of four instruments: MASS, Faraday rotation antennas, Colorado Dust Detectors (CDD), and the forward set of electric field booms..... 39

Figure 8. Engineering drawing of the aft payload section consisting of two instruments: the aft set of electric field booms and the photometer. 40

Figure 9. ALWIN radar and ALOMAR RMR-Lidar data for the first MASS launch occurring on August 3, 2007 at 22:51:20 UTC. The two plots on the left show the radar data for the fifteen minute period nearest the MASS1 launch for the zenith beam and the north-west beam. The plot in the middle shows the radar data for the two radar beams at the launch time. The plot on the right shows ALOMAR RMR Lidar measurements of aerosol backscatter coefficients (green) integrated over one minute for the MASS1 launch. 46

Figure 10. The electron density from Faraday rotation and the positive ion density measured by the MASS instrument channel 1+ during the MASS1 upleg. 47

Figure 11. Data from the 8 channels of the MASS instrument for the upleg of the first flight. Channels 4+ and 4- are offset from zero for clarity and their sum is plotted with no offset. 49

Figure 12. Data from the eight channels of the MASS instrument for the downleg of the first flight. Channels 4+ and 4- are offset from zero for clarity and their sum is plotted with no offset. 51

Figure 13. ALWIN radar and ALOMAR RMR Lidar data for the second MASS launch occurring on August 6, 2007 at 22:56:00 UTC. The two plots on the left show the radar data for the 15 minute period nearest the MASS launch for the zenith beam and the north-west beam. The plot in the middle shows the radar data for the two beams at the launch time. The plot on the right shows the RMR Lidar backscatter coefficient integrated over a 14 minute period closest to the MASS launch. 57

Figure 14. Data from the 8 channels of the MASS instrument for the downleg of the first flight. Channels 4+ and 4- are offset from zero for clarity and their sum is plotted with no offset. 58

Figure 15. The electron density from the Faraday rotation experiment and the positive ion density measured by the MASS instrument channel 1+ during the upleg of the second MASS flight. 59

Figure 16. Data from the 8 channels of the MASS instrument for the downleg of the second flight. Channels 4+ and 4- are offset from zero for clarity and their sum is plotted with no offset. 61

Figure 17. These plots display the upleg of MASS1 and MASS2, the + line is a sum of all positive channels, the - line is a sum of all negative channels, and the Sum line is the sum of all channels. The negative channel includes the electron density measured by the Faraday rotation antennas. A zero sum implies all charges have been collected, which occurred during the MASS1 upleg between 83 and 86 km... 63

Figure 18. SOFIE observations on August 3, 2007 nearest to the first MASS flight, 20:35 UTC at 71.3 N, 30.4 E (left panel) and at 22:12 UTC at 71.3 N, 6.3 E (right panel). Horizontal dotted lines indicate Z_{top} , Z_{max} , and Z_{bottom} determined from $H_2O(ice)$ 67

Figure 19. SOFIE observations on August 6, 2007 closes to the second MASS flight: 21:02 UTC at 72.0° N, 22.6° E (left panel) and 22:39 UTC at 72.0° N, 358.4° E (right panel). The horizontal dotted lines indicate Z_{top} , Z_{max} , and Z_{bottom} determined by $H_2O(ice)$ 68

Figure 20. A plot of the Mie absorption cross-section as a function of wavelength for four types of spherical particles: a 1 nm in radius particle of hematite, a 2 nm in radius particle of ice, and a 1 nm in radius composite particle with a core of hematite covered in 1 nm of ice and 99 nm of ice for total radii of 2 nm and 100 nm. The plot shows that the hematite core increases the absorption cross-section for a composite NLC particle thus increasing photoemission and photodetachment rates. 84

Figure 21. The average charge number on an ice particle as a function of radius for three different conditions: no photodetachment, photodetachment with a SZA of 93°, and

photodetachment with a SZA of 0° . The average charge becomes less negative with increasing photoemission. 86

Figure 22. (A) the charge probability distribution for an ice particle with no photodetachment for several different radii is shown. The electron and ion density is 3162 cm^{-3} . (B) shows the charge probability distribution for an ice aerosol particle for several different radii. Photodetachment is included for a SZA of 93° . For both cases, the number density of ice particles is assumed much smaller than the electron and ion density of 3162 cm^{-3} 87

Figure 23. The charge probability distribution for hematite particles of several different radii including photoemission and photodetachment rates with a SZA of 93° . If the SZA is 0° , the charge probability is nearly unchanged..... 88

Figure 24. Two plots of the charge probability for a 1 nm radius hematite particle coated in layers of ice with an outer radius of 2, 10, 20, 60, 100 nm. In (A) the charge probability is calculated using the volume averaged model for the photodetachment rate and with a SZA of 93° . In (B) the charge probability is calculated using the hematite model for the photodetachment rate..... 90

Figure 25. Plot of the number density of ice particles as a function of radius assuming a monomodal distribution for three water vapor mixing ratios: 1, 5, and 10 ppm..... 92

Figure 26. Model result for the high number density model of ice particles with 5 ppm water vapor. Plots A and B show the charge probability distribution and charge number densities for pure ice particles. Plots C and D show the charge probability distribution and charge number densities for composite particles using the volume

averaged model for photo-charging. Plots B and D display the number densities a function of particle radius for the electrons, the ions, the positive NLC particles, and the negative NLC particles.	94
Figure 27. The number density results from the DSMC calculations for all 6 altitudes. The plot is a 2-D slice through the MASS instrument. Note: the scale differs on each graph.	112
Figure 28. The temperature results from the DSMC calculations for all 6 altitudes. The plot is a 2-D slice through the MASS instrument. Note: the scale differs on each graph.	113
Figure 29. The air flow speed results from the DSMC calculations for all 6 altitudes. The plot is a 2-D slice through the MASS instrument. Note: the scale differs on each graph.	114
Figure 30. Calibration curves for an altitude of 75 km.	115
Figure 31. Calibration curves for an altitude of 80 km.	115
Figure 32. Calibration curves for an altitude of 82.5km.	116
Figure 33. Calibration curves for an altitude of 85km.	116
Figure 34. Calibration curves for an altitude of 87.5 km.	117
Figure 35. Calibration curves for an altitude of 90 km.	117
Figure 36. Calibration curves for positive particles at an altitude of 75 km with a payload potential of -1 V.	118
Figure 37. Calibration curves for negative particles at an altitude of 75 km with a payload potential of -1 V.	118

Figure 38. Calibration curves for positive particles at an altitude of 80 km with a payload potential of -1 V.....	119
Figure 39. Calibration curves for negative particles at an altitude of 80 km with a payload potential of -1 V.....	119
Figure 40. Calibration curves for positive particles at an altitude of 82.5 km with a payload potential of -1 V.....	120
Figure 41. Calibration curves for negative particles at an altitude of 82.5 km with a payload potential of -1 V.....	120
Figure 42. Calibration curves for positive particles at an altitude of 85 km with a payload potential of -1 V.....	121
Figure 43. Calibration curves for negative particles at an altitude of 85 km with a payload potential of -1 V.....	121
Figure 44. Calibration curves for positive particles at an altitude of 87.5 km with a payload potential of -1 V.....	122
Figure 45. Calibration curves for negative particles at an altitude of 87.5 km with a payload potential of -1 V.....	122
Figure 46. Calibration curves for positive particles at an altitude of 90 km with a payload potential of -1 V.....	123
Figure 47. Calibration curves for negative particles at an altitude of 90 km with a payload potential of -1 V.....	123

CHAPTER 1: NOCTILUCENT CLOUDS

In the polar summer mesosphere ice particles grow sufficiently large to scatter sunlight, giving rise to visible cloud displays called Noctilucent Clouds (NLC), often called Polar Mesospheric Clouds (PMC) [Witt, 1969; Hunten et al., 1980; Turco et al., 1982]. NLC form between 80 and 90 km as a result of the extremely low temperatures at the mesopause of ~ 130 K [Lübken, 1999] and the marginal availability of water vapor [Seele and Hartogh, 1999]. The low temperatures are due to the adiabatic expansion of up-drafted air caused by the mean meridional circulation [Karlsson et al., 2009]. NLC occur in the D-region of the ionosphere. The charging of ice particles by electron attachment can create steep gradients in the electron density, resulting in strong radar returns called Polar Mesospheric Summer Echoes (PMSE) [Cho and Kelley, 1993; Cho and Röttger, 1997; Rapp and Lübken, 2004].

NLC have been suggested as sensitive tracers for climate change in the mesosphere [Thomas, 1996; Thomas and Olivero, 2001]. In order to use NLC as indicators for climate change the physical forcing mechanisms that drive their formation and variability must be understood. The two main drivers of NLC formation are water vapor and cold temperatures, which may be enhanced by the long term changes in atmospheric methane and carbon dioxide [Thomas, 1996]. Increased methane production may lead to an increase in water vapor in the mesosphere and an

increase in carbon dioxide may lead to decreased temperatures in the mesosphere. The result of more water vapor and lower temperatures would be larger sized NLC particles with larger densities; hence brighter clouds would form more frequently [Thomas, 1995]. A recent satellite study has observed a long-term increase in NLC brightness; however, the exact cause is unknown [DeLand et al., 2006; 2007]. The connection between NLCs and climate change remains controversial [von Zahn, 2003], as it is difficult to separate natural forcing from anthropogenic forcing, especially when many questions about the formation of NLC exist.

1.1 NLC NUCLEATION

The microphysics involved in the formation of NLC ice particles is poorly understood. It has been suggested that NLC form via homogeneous nucleation at very low temperatures, $T < 120$ K [Murray and Jensen, 2010]. The mean temperature in the mesosphere is 130 K with local deviations up to ± 15 K [Lübken, 1999]. The formation of ice particles via heterogeneous nucleation is possible at higher temperatures (140 K) and becomes more likely at lower temperatures [Keese, 1989]. Thus, heterogeneous nucleation is considered the dominant mechanism for NLC formation, even though the condensation nucleus for heterogeneous nucleation remains unknown. Several types of particles have been suggested as the condensation nuclei for NLC: sulphate aerosols [Mills et al., 2005], soot particles [Pueschel et al., 2000], water cluster ions [Witt, 1969; Balsiger et al. 1996], or meteoric smoke particles (MSP) [Hunten et al., 1980].

Mills et al. [2005] suggested that sulfate aerosols survived transport into the mesosphere in sufficient numbers to be considered possible condensation nuclei for NLC; whereas previously, it was thought that sulfate aerosols were destroyed by UV in the stratosphere, limiting the abundance of sulfate aerosols in the mesosphere [Rinsland et al., 1995]. From a laboratory study on the photolysis of sulfuric acid, it was predicted that sulfate aerosols are stable against UV dissociation even in the environment of the mesosphere [Burkholder et al., 2000]. Mills et al. [2005] also hypothesized that sulfate aerosols would be better condensation nuclei than meteoric smoke particles as sulfate aerosols are expected to have a crystalline structure similar to water ice. Evidence for sulfate aerosols as condensation nuclei could be examined using correlations between volcanic eruptions and changes in NLC brightness or frequency. NLC were first observed in 1885, two years after the eruption of Krakatoa [Schröder, 2001]. However, since then several volcanic eruptions have occurred without a significant effect on NLC: Mt. Agung, El Chichon, and Mt. Pinatubo [Thomas and Olivero, 2001]. Presently, more information is required to address the claim that sulfate aerosols serve as condensation nuclei for NLCs.

Pueschel et al. [2000] put forth soot particles as possible condensation nuclei for NLC. It has been theorized that soot particles originating from airplane exhaust will be lifted by photophoresis into the mesosphere. At an altitude of 20 km, soot particles are observed to have a size range between 150 nm to 1000 nm in radius. It has been suggested that the largest soot particles (~1000 nm) are the particles lifted into the mesosphere. A typical NLC particle is 20 - 100 nm in radius, implying these lifted soot

particles are too large to be condensation nuclei [Rapp and Thomas, 2006]. It is possible for the soot particles to fragment into ~ 50 nm as they are transported into the mesosphere, but even this is still too large. Although soot particles have predicted sizes and number densities equivalent to NLC particles, they have never been observed by lidars [Rapp and Thomas, 2006].

Water cluster ions of the form $H^+(H_2O)_n$ where n is an integer have been suggested as possible condensation nuclei for NLCs [Witt, 1969]. In the mesosphere water cluster ions have been observed to grow as large as $n = 21$ by in-situ mass spectrometers [Björn and Arnold, 1981]. However, numerical models of water cluster ion growth and stability have shown that water cluster ions require $n > 100$ (a radius $> \sim 1$ nm) for further growth in the mesosphere [Gumbel et al., 2003]. In addition, proton hydrates can undergo dissociative electron recombination destroying the growth of the cluster [Rapp and Thomas, 2006]. Therefore, under typical mesospheric conditions, water cluster ions have a low probability of nucleating NLCs.

Meteoric smoke particles (MSP) are considered the most likely condensation nuclei for NLCs [e.g., Rapp and Thomas, 2006; Megner and Gumbel, 2009]. MSP are formed after meteors ablate in the upper atmosphere and the resulting vapor condenses to form nanometer sized particles in the altitude range between 75 and 115 km [Rosinski and Snow, 1961; Hunten et al., 1980]. Therefore, MSP consist of meteoric elements: silicon, iron, magnesium, potassium, aluminum, and calcium [Plane, 2003]. Saunders and Plane [2006] demonstrated in the laboratory that iron-rich vapor particles, like ablated meteors, will condense to form MSP due to the attraction between their

magnetic dipole moments. A recent laboratory experiment demonstrated that iron oxide particles with a radius of ~ 15 nm can be effective ice condensation nuclei at 180 K [Saunders et al., 2010]. The laboratory studies of MSP formation and the nucleation of NLC on MSP is limited, especially for mesospheric conditions of 130 K and MSP radii below 15 nm. In the mesosphere, MSPs charge due to electron and ion attachment and possibly photo-charging due to solar irradiation. The charged fraction of MSPs has been measured by in-situ experiments [Schulte and Arnold, 1992; Gelinias et al., 1998; Croskey et al., 2001; Lynch et al., 2005]; Amyx et al., 2008], but the total MSP number density and size distribution remain unresolved.

Hunten et al. [1980] derived a theoretical MSP size distribution that has been used for multiple numerical simulations of NLC [e.g. Jensen, 1989; Rapp and Thomas, 2006]. Recently, two separate three-dimensional global climate models were developed to study the formation of NLC on MSP [Bardeen et al., 2008; Megner et al, 2008a; Megner et al., 2008b]. These two models suggest that MSP are transported away from the polar summer mesosphere, lowering the concentration of viable MSP to be condensation nuclei. By the time the MSP form and grow to $\sim 1-2$ nm in radius they are transported away from the polar summer mesosphere by meridional circulation. This predicted decrease in large MSP in the polar summer mesosphere has been confirmed by recent observations from the Aeronomy for Ice in the Mesosphere (AIM) satellite [Hervig et al., 2009]. Although the > 1 nm in radius MSP are transported away, there still remains a large population of MSP with radii below 1 nm. For typical mesospheric conditions, the critical radius needed to be considered a condensation nucleus for NLC

is 1 nm. This critical radius is reduced if the condensation nucleus is charged. Thus, Megner et al. [2009] suggested that charged MSP are the condensation nuclei for NLC, possibly solving this dilemma.

1.2 NLC MEASUREMENT TECHNIQUES

NLC ice particles are often observed using remote sensing techniques: cameras [DeLand et al., 2006], lidars [von Cossart et al., 1999], and satellites [Gordley et al., 2009; Hervig et al., 2009]. Optical observations have measured NLC size ranges between 20 – 100 nm in radius with number densities of the order of 100 cm^{-3} [Baumgarten et al., 2008]. The formation of these large ($> 20 \text{ nm}$) NLC ice particles is dependent upon a large population of subvisual particles about which less is known. Both populations of ice particles may charge in the D-region of the ionosphere. If the number density of ice particles is large enough, then under the right conditions electron bite-outs can occur. These electron bite-outs have been measured by in-situ rocket instruments [Pedersen et al., 1970; Ulwick et al., 1988; Croskey et al., 2004]; in addition, ion bite-outs have also been measured [Balsiger, 1996]. The smaller ice particles tend to have larger number densities, which are then more likely to cause gradients in the electron density, and thus cause PMSE. The occurrence of PMSE does not imply a NLC will form and vice versa.

Due to the high altitude of the mesosphere, in-situ measurements to study NLC can only be made by sounding rockets. The majority of rocket-borne particle detectors measure the deposition of charge from impacting particles on an exposed collection surface, taking advantage of particle charging in the mesosphere. Several types of

charged particle detectors have been flown: Faraday cups [Havnes et al., 1996], magnetically shielded detectors [Smiley et al., 2003], Gerdien condensers [Croskey et al., 2001], and active photoionization instruments [Croskey et al., 2003; Rapp and Strelnikova, 2008]. All of the above instruments have a means of limiting electron and ion collection. The Faraday cup uses a set of biased grids to repel electrons and ions. A magnetically shielded detector like the Colorado Dust Detector (CDD) deflects electrons using a set of permanent magnets and a biased voltage to repel positive ions [Smiley, 2006]. These first two instruments have a single detection channel measuring the summed current from both positively and negatively charged particles; as a result a larger population of negative charged particles can mask a smaller population of positive particles. In addition, single channel instruments have limited mass resolution and often particles below 2 nm in radius are carried away from the detector by aerodynamic effects [Horányi et al., 1999; Hedin et al., 2007]. Some instruments like the Gerdien condenser have mitigated aerodynamic effects by adding ventilation. The Gerdien condenser is a cylindrically symmetric instrument with a center electrode, which is swept in voltage to collect charged particles with a wide range of masses [Croskey et al., 2001; Mitchell et al., 2001]. The Gerdien condenser therefore has better mass resolution than single channel detectors. It can also measure both positive and negatively charged particles, if the sweeping voltage changes polarity. However, the trade-off for these two advantages is altitude resolution, limited by the sweeping time and the rocket velocity. One of the more recent instruments is the ECOMA (Existence and Charge state Of meteor smoke particles in the Middle Atmosphere) instrument,

which is a ventilated Faraday cup combined with a xenon flashlamp for active photoionization [Rapp and Strelnikova, 2009]. The ECOMA instrument detects electrons from photoemission and photodetachment to measure the total NLC volume density. Although the ECOMA instrument measures the total NLC volume density, it has limited altitude resolution due to the pulsed nature of the xenon lamp and limited mass resolution due to the Faraday cup design.

1.3 THE PRESENT STUDY

In this work, (1) a new rocket-borne instrument, the Mesospheric Aerosol Sampling Spectrometer (MASS), is described and modeled, (2) the resulting MASS data are presented and discussed and (3) a numerical charge model is developed to explain the MASS data. The MASS instrument is designed to study the mass distribution of charged aerosol particles of both polarities simultaneously in the mesosphere. This instrument is an electrostatic mass spectrometer consisting of four pairs of collection plates. Each pair of plates collects a specific mass range and each pair is able to collect particles with both polarities of charge. In Chapter 2, the MASS instrument is described in more detail and the instrument's calibration. Many in-situ particle detectors are unable to detect particles below 2 nm in radius due to aerodynamic effects; the MASS instrument was specifically designed to have no such lower detection limit. The instrument's collection range varies from molecular ions to particles with radii of hundreds of nanometers. The MASS instrument was flown on two sounding rockets as part of the MASS/ECOMA rocket campaign. The two MASS flights were combined

with one ECOMA flight, ground-based observations from Lidar and radar, and an overpass by the AIM (Aeronomy of Ice in the Mesosphere) satellite. In Chapter 3, the MASS payload, the ground-based observations, the MASS data, and the AIM data are presented. The first MASS launch on August 3, 2007 was flown into a NLC and a PMSE, while the second flight on August 6, 2007 was just flown into a PMSE. The MASS instrument successfully returned data for both the upleg and the downleg of each flight. For the first time the charge number densities of positive and negative NLC particles were measured simultaneously. In addition, the MASS instrument measured for the first time a low resolution mass distribution of NLC particles. The MASS results show the coexistence of negative and positively charged particles at the same altitude.

In order to better understand the MASS data a charge model was also developed. The charge model includes charging of meteoric smoke particles, as the charge on MSP determines if they can be effective condensation nuclei. The charge model is based on the traditional electron and ion attachment rates [Natanson, 1960] and photo-charging rates. Previously, it was expected that NLC particles would only charge negatively due to the electron thermal velocity being larger than the ion thermal velocity [Jensen and Thomas, 1991]. The inclusion of photo-charging in the model was motivated by the unexpected positive charge layer measured by the MASS instrument. The details of the charge model and the results are shown in Chapter 4. The results from the MASS flights and the charge model are summarized in Chapter 5, along with a discussion of possible future work. Many of the results in this work have been published: a review of the MASS instrument can be found in Knappmiller et al. [2009], a review of the MASS

launch and data results can be found in Robertson et al. [2009], and the charge model results can be found in Knappmiller et al. [in press].

CHAPTER 2: The MASS Instrument

The Mesospheric Aerosol Sampling Spectrometer (MASS) is a rocket-borne instrument for detecting charged nanometer sized aerosols, see Figure 1. The instrument collects both positively and negatively charged aerosols from a continuously admitted volume of air sampled by four pairs of biased graphite collection plates. The particles are separated by their charge to mass ratio by the instrument's static electric field. The number density of charged particles in each size bin is calculated from the current collected on each graphite plate. Assuming that the particles collected are composed of ice with a density of 931 kg m^{-3} , then the approximate collection ranges for the four plates are $< 0.5 \text{ nm}$, $0.5 - 1 \text{ nm}$, $1 - 2 \text{ nm}$, and $> 3 \text{ nm}$ in radius. The collection ranges change with altitude as the rocket velocity, air density, and temperature vary. The collection range is modeled at six altitudes from 75 to 90 km using three computer models: an electric field model, a Direct Simulation Monte Carlo (DSMC) aerodynamics model, and a particle trajectory model. The trajectory simulation includes collisions with the background gas and the deflection from the electric field. The instrument's modeled mass sensitivity closely matches an experimental calibration using an argon ion source. The mechanical and electrical design of the instrument will be described in sections 2.1 and 2.2. The experimental calibration and the associated numerical calculations will be presented in section 2.3 and 2.4. The numerical calibration results

will be presented and discussed in section 2.5. The MASS instruments design and calibration are also summarized in Knappmiller et al. [2009].

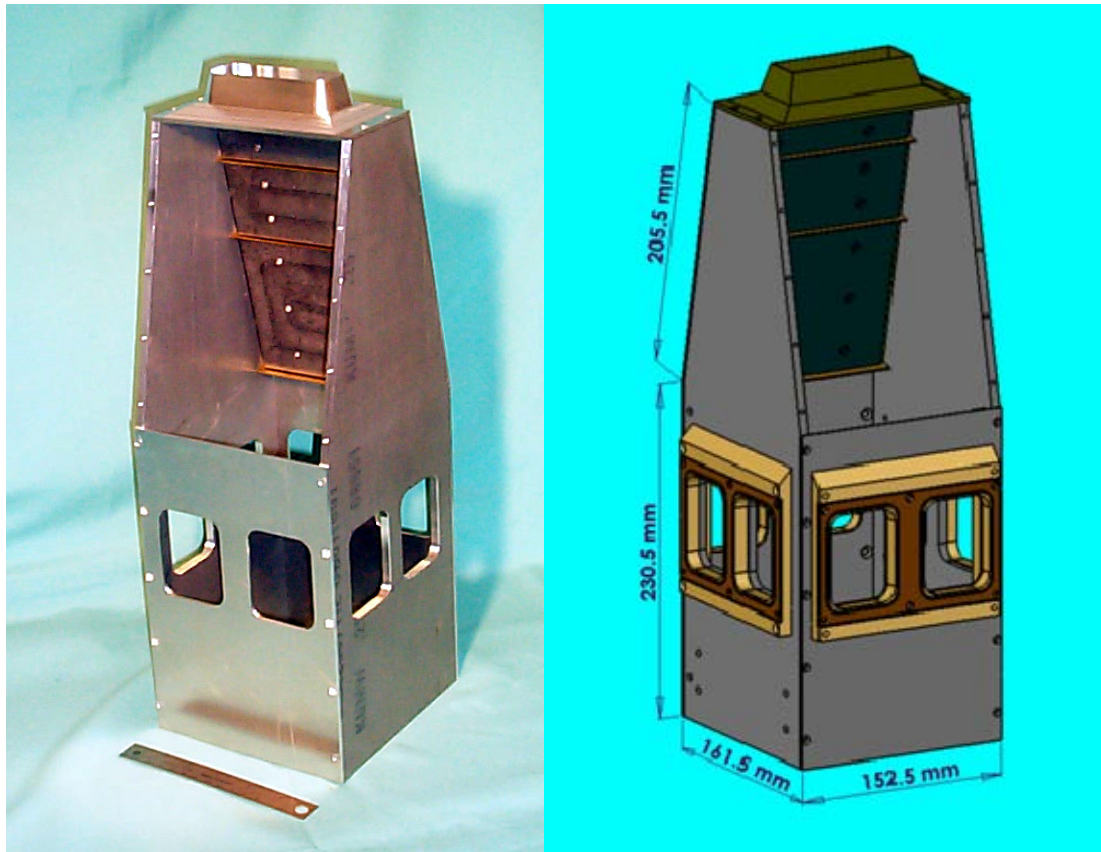


Figure 1. Photograph of MASS instrument (left) and mechanical drawing of the MASS instrument (right). Both images have a set of graphite plates removed to show the inside of the instrument. The mechanical drawing includes a set of mesh grid holders on the air exit windows, which are biased to prevent electron and ion collection.

2.1 MECHANICAL DESIGN

The MASS analyzer is flown supersonically on the top deck of a sounding rocket where a shock wave forms above the instrument. The MASS instrument's mechanical structure was designed to mitigate aerodynamic effects that would prevent the collection of charged aerosols. Previous numerical simulations have shown that the

shock wave above the entrance of a rocket-borne instrument can prevent the collection of particles less than 1 – 2 nm in radius [Horányi et al., 1999; Rapp et al., 2005; Hedin, J., et al., 2007; Amyx et al., 2008]. Hence, small particles are carried away by the shock, while large particles are able to penetrate the shock and enter the instrument for collection. The entrance to the MASS instrument was specifically designed to minimize the shock wave and allow the collection of small particles. The condition for eliminating a shock is given by $M \sin(\theta) < 1$, where M is the Mach number and θ is the angle between the incoming air flow and the deflected air around the instrument [Bird, 1988]. The opening of the MASS analyzer has a knife-like aperture with a slope of $\theta=15^\circ$. This slope was chosen to meet the above requirement for nominal rocket velocities of 1000 m/s.

The mechanical design of the instrument included additional features to enhance the collection efficiency of charged aerosol particles. For example, four pairs of windows were added near the bottom of the instrument to alleviate air density stagnation. Previous rocket-borne instruments had limited particle collection due to stagnation, which increases collisions within the instrument scattering particles away from detectors [Hedin, J., et al., 2007].

The addition of the windows to the MASS instrument made it possible for unwanted electrons and light ions to be collected through the windows opposite to the air flow. To prevent the collection of electrons and light ions through the windows, biased mesh screens were added. The polarity of the bias was selected to collect positive ions and to repel electrons. The bias voltage of -10 V was selected so that the

radius of the effective cross-section of the mesh wires (1.4 mm) was larger than the wire separation (1.2 mm). The radius of the effective cross-section is calculated using cylindrical probe theory [Mott-Smith and Langmuir, 1925]. The effective radius is increased by a factor of $(1 - q\Phi/k_B T)^{1/2}$ where q is the ion charge, Φ is the potential on the wire, k_B is Boltzmann's constant and T is the temperature of the ions, assumed to be in equilibrium with the mesosphere ($T = 140$ K).

Another MASS feature that improved collection efficiency was the sloping of the graphite collection plates away from the MASS entrance to prevent them from being bombarded by the neutral background gas. The entrance has an increased area (25.2 cm²) compared to the previous Colorado Dust Detector (7.25 cm²), which flew on several rocket campaigns [Smiley et al., 2003; Amyx et al., 2008]. The increased area is needed to increase the collected current, which is split between eight collection surfaces. The graphite collection surface width is 140 mm parallel to the entrance slit, which was chosen to be wider than the width of the entrance to ensure a uniform electric field across the flux of incoming charged particles. Graphite was chosen for the collection plates since graphite has a high workfunction and low photoelectric yield [Feuerbacher, 1972]. The graphite plates are attached to insulating blocks of Noryl, used for its low moisture absorption. Each graphite plate at the top of the instrument is separated by a grounded brass spacer. These grounded surfaces better define the electric field distribution near each graphite plate enhancing particle collection.

2.2 ELECTRICAL DESIGN

The electronics for the MASS instrument is based on the Colorado Dust Detectors (CDD) [Smiley et al., 2003]. The electronics are composed of batteries and current-to-voltage amplifiers. The graphite collection plates are connected to batteries providing the bias for the deflecting electric field. The bias voltages for the top three plates are ± 1.7 V, ± 5.4 V, and ± 54 V. The bottom most graphite collecting plates have no bias voltage. The batteries are connected to current-to-voltage amplifiers to measure the deposited charge from impacting particles.

The MASS instrument had two circuit designs: the first has a gain of 1 V/nA (Circuit I) and the second has two channels with a gain of 0.1 V/nA and a gain of 1 V/nA (Circuit II). These sensitive electrometers consist of a two stage circuit: a current-to-voltage amplifier and a buffer. The electrical circuits for the MASS instrument are displayed in Figure 2. Both designs use an operational amplifier (OPA129) with a 10 M Ω resistor in the feedback loop connected to a 100 times or 10 times voltage divider providing the high current-to-voltage gain. After the amplifier, a low pass filter with a cut off frequency of 640 Hz is connected to a buffer amplifier (BUF634) to drive the signals to the telemetry system. Circuit I is used for the second, third, and fourth graphite plates; while circuit II is used for the first graphite plate. Having an additional channel with a lower gain on the first graphite plate allows for a larger signal without saturation, implying a higher detectable charge number density. The first pair of graphite plates in the MASS instrument collects electrons and light ions, whose density

increases exponentially in the mesosphere from $\sim 100 \text{ cm}^{-3}$ at 70 km to $\sim 10,000 \text{ cm}^{-3}$ at 90 km [Brasseur and Solomon, 1986].

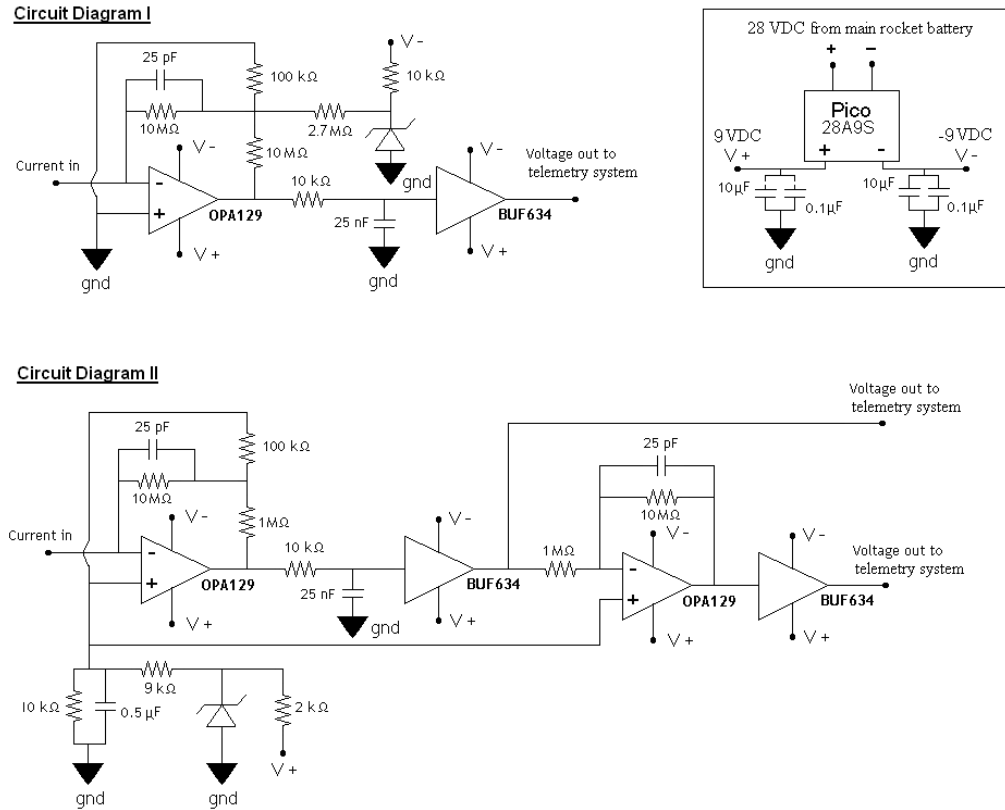


Figure 2. Circuit diagrams for the current to voltage electronics used in the MASS instrument. Circuit I is for the second, third and fourth graphite collection plates. Circuit II has two gains and is for the first collection plate.

The telemetry system for the rocket had inputs designed for signals from 0-5 volts. To allow for negative signals, the outputs of circuits I and II have an offset of 2.5 V, allowing for $\pm 2.5 \text{ nA}$ of current to be recorded when the gain is 1 V/nA . The telemetry was sampled at a rate of 1 kHz with a resolution of 12 bits, which corresponds to a current resolution of 1.25 pA. The altitude resolution is one meter at the nominal rocket velocity of 1000 m/s. The root-mean-square noise level on the circuits is 3 pA sampled at 1 kHz. Therefore, the minimum detectable density of charged aerosols

corresponds to ~ 8 particles per cm^3 . The returned rocket data were averaged using a Gaussian window with a width of 10 ms to reduce high frequency noise. Both circuits I and II were powered by the telemetry system battery pack at 28 V. The OPA129 and the BUF634 require a power supply of ± 9 V. The 28 V battery voltage was stepped down using a DC/DC converter (PICO28A9S). A pair of capacitors was added to filter the noise from the DC/DC converter.

All of the electronics for the MASS instrument were calibrated before launch. A *LabView* program was written to step a voltage across a gigaohm resistor, providing a known current to the input and then the output voltage was recorded. The gain of each circuit was measured by plotting the output voltage versus input current and performing a linear regression to obtain the slope. The gain is used to convert the telemetry signal to a current, which is used in calculating the charge number density. The measured current (I) is equal to the number density of charged aerosols (n) entering the MASS instrument:

$$I = fqnvA, \tag{2.1}$$

where f is the collection efficiency, q is the electron charge, v is the rocket velocity, and A is the area of the opening into the MASS instrument. The collection efficiency is calculated using a numerical particle trajectory program presented in section 2.4. The maximum detectable signal is ± 2.5 nA of current, which corresponds to a maximum detectable charge number density of ± 5850 cm^{-3} assuming the collection efficiency is 100%.

2.3 LABORATORY CALIBRATION

In the MASS analyzer the detection of a given particle is dependent upon its charge to mass ratio and its velocity. The higher the velocity the further a charged aerosol will penetrate into the instrument before being deflected by the static electric field and collected. The main contribution to the charged aerosol's velocity is the rocket velocity. The MASS instrument separates aerosols by their charge to mass ratio, since all the charged aerosols have approximately the same velocity. The collection efficiency is affected by the additional thermal velocity of the collected charged aerosols, especially for the smallest particles. The effect of the thermal velocity will be discussed in the numerical calibration section.

Before launching the MASS instrument, it was necessary to calibrate the instrument's mass range and collection efficiency for each graphite collection plate. The MASS analyzer was calibrated in the laboratory using a radio frequency (RF) argon ion beam. The kinetic energy of the ion beam was varied to simulate charged aerosols with different masses. The beam energy was varied from 20 eV to 200 eV with a mean current of 100 nA. The ion beam energy and distribution were measured using a gridded Faraday cup. The energy of the ion beam is converted into an effective mass and radius assuming the aerosol is singly charged, has an ice density of 931 kg/m^3 and has a speed equal to the nominal rocket velocity of 1000 m/s. The results of the laboratory calibration are shown in Figure 3 and the mass collection ranges are displayed in Table 1. The first collection plate in the MASS instrument was not calibrated using the argon ion beam due to the limited beam current at the lowest

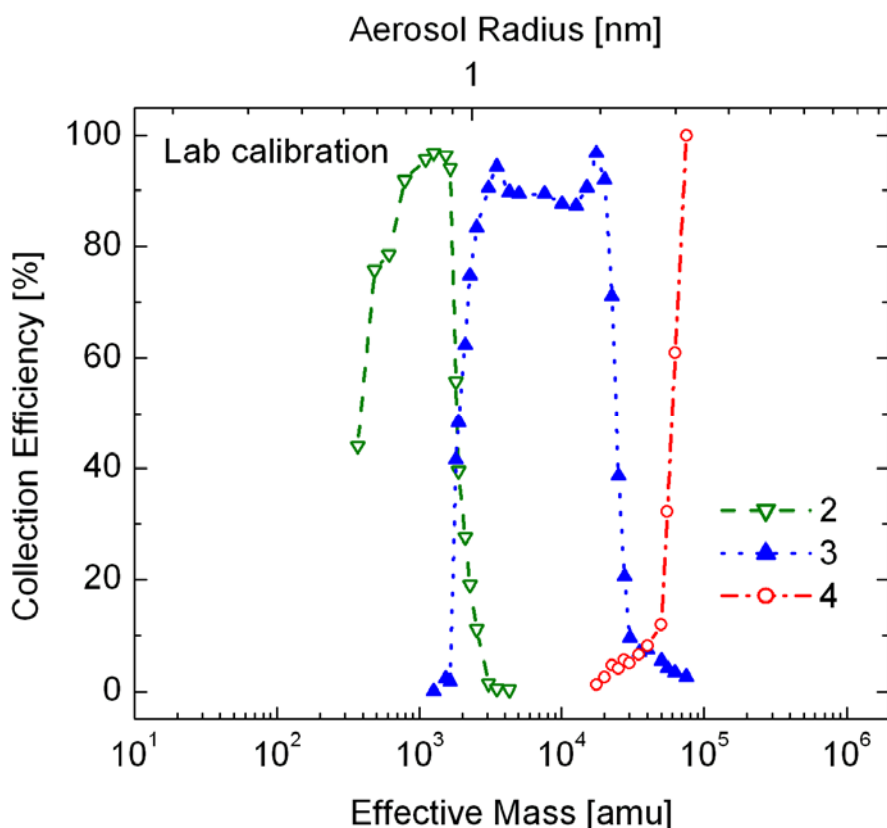


Figure 3. Experimental calibration curves for the MASS instrument. A laboratory calibration was performed using an argon ion source simulating the charged aerosols particles in the mesosphere. The numbers 2, 3, and 4 refer to the graphite collection plates as numbered from the top of the instrument.

energies. In the laboratory calibration, the air number density in the vacuum chamber is significantly lower than the density in the mesosphere. The mean free path in the vacuum chamber at a pressure of 10^{-6} Torr is approximately the length of the chamber, while the mean free path in the mesosphere at 90 km at a pressure of 1 mTorr is approximately 1 cm. Thus, the laboratory calibration is considered collisionless, while the actual measurement is affected by collisions with the background gas. In order to quantify the effect of collisions a numerical calibration was also performed.

2.4 NUMERICAL CALIBRATION

The numerical calibration is used to determine the collection efficiency and mass range for each graphite collection plate in the MASS instrument as a function of altitude. The numerical calibration of the MASS instrument is done with a combination of three computer programs: an electric field simulation, a Direct Simulation Monte Carlo (DSMC) aerodynamics calculation, and a particle trajectory simulation. The outputs of the electric field simulation and the DSMC calculation are inputs used in the third simulation; which calculates a test particle's trajectory through the MASS instrument. The electric field is needed to calculate the acceleration of the test particle towards the graphite collection plates. The DSMC calculates the air density, temperature, and velocity in order to simulate the effects of collisions. The trajectory program calculates the position of the test particle by integrating its equation of motion using Runge-Kutta and includes collisions using a Monte Carlo routine. All three of the simulations will be described in detail in the following three sections.

2.4.1 ELECTRIC FIELD

The electric field within the MASS instrument is calculated by taking the negative gradient of the electrostatic potential in MASS. The electrostatic potential is found by solving Laplace's equation using a relaxation method [Press et al., 1986]. The calculation is done on a three dimensional rectangular grid with grid spacing of 1 mm x 2.5 mm x 2.5 mm. The bias voltages on each graphite collection plate are included as boundary conditions: ± 1.7 , ± 5.4 and ± 54 V. The bias voltage of -10 V on the air exit

windows is also included in the simulation. All other MASS surfaces are grounded on the boundary including the brass spacers between the graphite collection plates. The electrostatic potential contours in MASS are shown in Figure 4. The contours would be perfectly antisymmetric (and are above $x = 250$ mm); however, the bias voltage from the

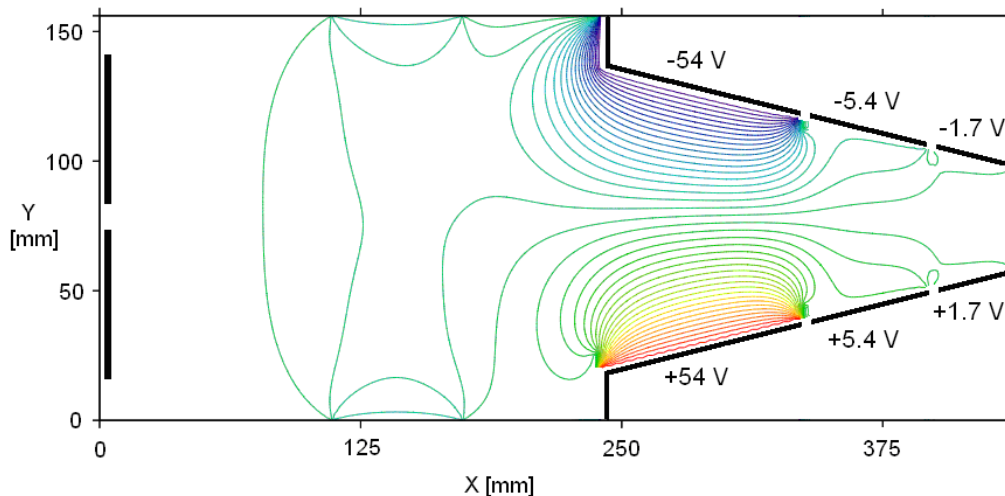


Figure 4. The above plot displays the potential contours in the MASS instrument and lists the voltages on the collection plates. The instrument is viewed on its side such that the top of the instrument is on the right and the bottom on the left.

air exit windows is symmetric. The added electric field from the air exit windows does not have a significant influence on the charged aerosol trajectories; however, it is included in the numerical calibration for completeness.

2.4.2 DIRECT SIMULATION MONTE CARLO MODEL

A Direct Simulation Monte Carlo (DMSC) three-dimensional computer code was used to quantify the air flow in and around the MASS instrument. Specifically, the air temperature, number density, and velocity field were calculated using the DSMC code.

These parameters are used to calculate collisions between the background gas and charged aerosol particles in the subsequent particle trajectory simulation.

The air flow around the payload changes from a continuum regime to a free molecular flow regime due to the exponential decrease in air density with increasing altitude. The Knudsen number, the ratio of the mean free path to the representative length scale of the instrument, is used to determine which air flow model is applicable. In the region of interest, between 80 and 90 km, the Knudsen number is approximately one, representing the transition regime between the continuum and the free molecular flow regime [Hedin et al., 2007]. As a result, the aerodynamic simulations are rather complex, i.e. the collisions with the background gas cannot be neglected nor modeled as a continuous drag force. The DSMC computer code is specifically designed to model and follow large numbers of colliding air molecules in the transition regime.

The MASS instrument and its surrounding payload support structure were modeled in the DSMC simulations using a three-dimensional CAD program (*SolidWorks*). The three-dimensional model of the instrument included the air exit windows and the knife-like opening; however, the mesh grids over the air exit windows were not included due to limited resolution. The exclusion of the mesh window grids in the simulation are justified since they are 85% transparent. The simulation volume starts 82 mm above the MASS instrument and ends after a bulkhead, which supports the MASS instrument. A total of six altitudes were simulated: 75, 80, 82.5, 85, 87.5, and 90 km. The variables that are dependent upon altitude include the rocket velocity, the background air density, and the background air temperature. The values used for these

variables at each altitude are shown in Table 1. Lübken [1999] compiled polar mesospheric temperature and air density measurements from 89 rocket flights over ten years and then fit a spline curve to the data to obtain averaged temperatures and densities for each day of the NLC season. The temperatures and air densities used in the DSMC calculation are interpolated values from Lübken [1999] and then averaged over the launch dates of the MASS instrument.

Altitude [km]	Velocity [m/s]	Density [m^{-3}]	Temperature [K]
75	1135	1.4×10^{21}	189
80	1092	5.4×10^{20}	161
82.5	1069	3.4×10^{20}	149
85	1047	2.0×10^{20}	140
87.5	1024	1.1×10^{20}	135
90	1000	6.1×10^{19}	139

Table 1. DSMC simulations were done at six altitudes. The initial conditions for each simulation are listed above. The velocity is the averaged rocket velocity from the two MASS launches. The density and temperature values are interpolated values from Lübken [1999] and then averaged over the two launch dates.

The results from the DSMC simulations for 85 km are shown in Figure 5, and the results for the other altitudes are shown in appendix A. The results show an enhanced air number density within the MASS instrument, approximately 1.5 times greater than the ambient density at an altitude of 85 km. The temperature inside the MASS instrument is near 300 K at 85 km. The flow velocity gradually decreases to zero at the bottom of the MASS instrument for all altitudes. The DSMC simulation results vary with altitude as expected, i.e. the air density within MASS and the flow velocity

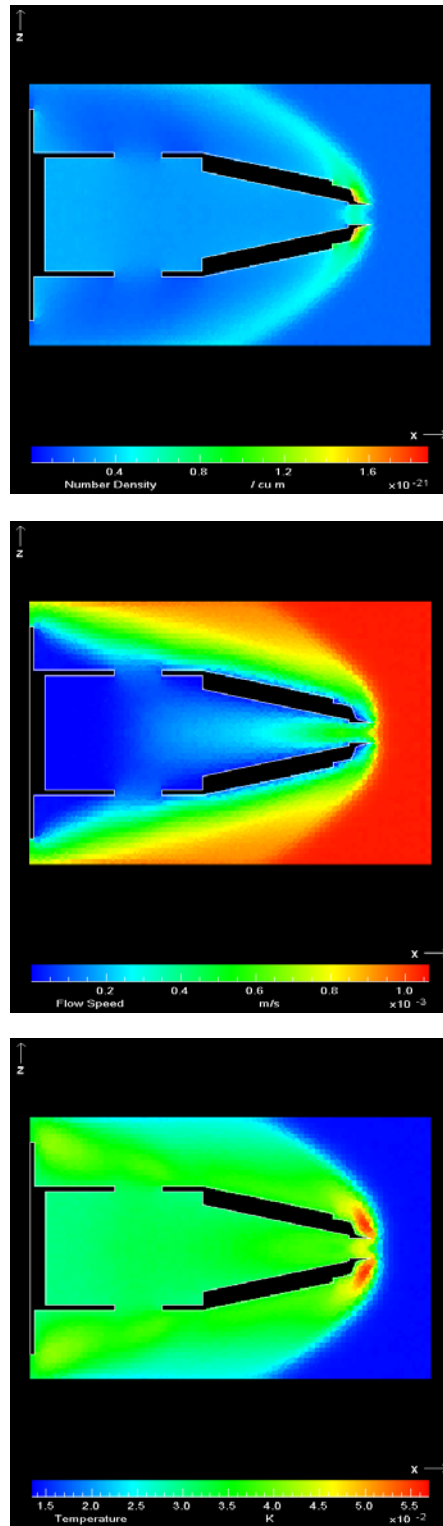


Figure 5. This shows the results of the DSMC computer model for the (A) air number density, (B) the air temperature, and (C) the air flow velocity in and around the MASS instrument for conditions at 85km.

decrease with increasing altitude. This dependence upon altitude is readily seen in the calculated collection efficiencies, which are discussed in section 2.5.

2.4.3 PARTICLE TRAJECTORY PROGRAM

The particle trajectory program follows a test particle through the MASS instrument and records where it is detected. The electric field model is used to calculate the deflection of the charged aerosols, while the DSMC temperature, flow velocity, and density are used to calculate the effect of collisions with the background air on the charged aerosol's trajectory. The deflection of the charged aerosols is determined by calculating the acceleration of the particle from the static electric field, then updating the velocity and position accordingly. The effect of collisions is adapted from a Monte Carlo method developed by Robertson and Sternovsky [2003] with basic principles modeled after Epstein [1924]. Epstein developed several models for the slowing of particles for subsonic particles in a gas. Hayes and Probstein [1959] and Probstein [1969] extended Epstein's work to include supersonic particles. Hayes, Probstein, and Epstein's models are all continuous drag models, which are not valid for small aerosol particles in the MASS instrument. The small aerosol particles have collisions with the background gas too infrequently to consider the gas as a continuum, yet not sufficiently infrequent to be neglected [Hedin et. al., 2007].

The fundamental basis for the collision model is momentum conservation. An air molecule collides inelastically with a charged aerosol particle and is then re-emitted randomly into 4π steradians. Epstein did not consider particle rotation and therefore

only emitted the air molecule into 2π steradians. Let M be the mass of the charged aerosol particle with initial velocity \vec{V}_0 , a velocity \vec{V}_1 after the collision, and a velocity \vec{V}_2 after the air molecule has been re-emitted. Let the air molecule have a mass m , an initial velocity \vec{u}_0 and an emitted velocity \vec{u}_2 . The momentum equations for the collision are shown below.

$$M\vec{V}_0 + m\vec{u}_0 = (M + m) \vec{V}_1 \quad (2.2)$$

$$(M + m) \vec{V}_1 = M\vec{V}_2 + m\vec{u}_2. \quad (2.3)$$

In the rest frame of the rocket, the initial velocity of the air molecule is composed of a random thermal velocity $\vec{u}_{random}^{(0)}$ and the air flow velocity from the DSMC simulations \vec{u}_{flow} such that $\vec{u}_0 = \vec{u}_{random}^{(0)} + \vec{u}_{flow}$. The random thermal velocity is chosen using the method of rejection from a Gaussian distribution centered at the local thermal velocity according to the DSMC temperature calculations [Press et al., 2007]. The emitted velocity of the air molecule in the rest frame of the charged aerosol particle is a random thermal velocity $\vec{u}_{random}^{(2)}$. In the rest frame of the MASS instrument, the total velocity for the emitted air molecule is the sum of the random thermal velocity plus the velocity of the charged aerosol particle just before the air molecule is emitted, $\vec{u}_2 = \vec{u}_{random}^{(2)} + \vec{V}_1$. Using the above velocities and solving for the final velocity of the charged aerosol particle, one obtains

$$\vec{V}_2 = \frac{M}{M + m} \vec{V}_0 + \frac{m}{M + m} (\vec{u}_{flow} + \vec{u}_{random}^{(0)}) - \frac{m}{M} \vec{u}_{random}^{(2)} \quad (2.4)$$

The velocity of the charged aerosol particle is determined by the above equation in combination with the change in its velocity due to the electric field within MASS.

In the particle trajectory program, a Monte Carlo approach is used to determine when a collision has occurred. A collision probability is calculated at every time step by multiplying the collision frequency by the program's differential time step. A random number is chosen between 0 and 1. If the random number is below the probability then the collision condition has been met.

The collision frequency is calculated by summing a subsonic and a supersonic collision frequency in quadrature:

$$\nu = \sqrt{\nu_{sub}^2 + \nu_{sup}^2} \quad (2.5)$$

where ν is the total collision frequency, ν_{sub} is the subsonic collision frequency, and ν_{sup} is the supersonic collision frequency. The subsonic case takes into account the random flux of air molecules to the aerosol particle's surface, while the supersonic case takes a projected view of the aerosol's cross-section in the flow. By adding the two collision frequencies in quadrature, the two limiting cases are smoothly connected. This collision frequency is required within the simulation as the aerosol's velocity at the entrance to MASS is supersonic and then slows gradually reaching subsonic levels at the bottom of the instrument. The collision is modeled as instantaneous; the velocity vector is changed by a small increment in a subroutine called between time steps. The collision frequency for a subsonic particle is:

$$\nu_{sub} = 4n\pi r^2 \sqrt{\frac{k_B T}{2\pi M}}, \quad (2.6)$$

where r is the radius of the aerosol, n is the local air number density, k_B is Boltzmann's constant, and T is the local temperature. In the particle trajectory program, the mass of the aerosol is specified and the radius of the particle is calculated assuming a spherical particle and a density for water ice of 931 kg/m^3 . The formula for a supersonic collision frequency is given by:

$$v_{sub} = n\pi r^2 U_{rel} = n\pi r^2 \left| \vec{V}_0 - \vec{u}_{flow} \right|, \quad (2.7)$$

where U_{rel} is the relative velocity between the aerosol particle and the air flow within MASS.

The particle trajectory simulation was compared to Epstein's [1924] subsonic continuous drag model for an aerosol particle with a radius of $\sim 3 \text{ nm}$ (10^5 amu). The two models were compared by finding the time required for the aerosol's velocity to drop by one e -folding. Epstein's subsonic continuous drag model gave half the time of the particle trajectory simulation. The longer slowing time for the particle trajectory time can be caused by two factors: the reduced number of collisions compared to a continuous drag model or the emission of the air molecule having no preferred direction in our collision model due to particle rotation.

The particle trajectory simulation starts with a set of initial conditions for each of the 35 different masses simulated. The masses are logarithmically spaced by factors of $\sqrt{2}$ and span $30 - 1.3 \times 10^6 \text{ amu}$. Each particle is started with a velocity that is the sum of the rocket velocity and a random thermal velocity. The random thermal velocity is dependent upon the particle's mass and the upstream temperature. The starting

position of the test particle is 82 mm above the entrance to the MASS instrument, which is chosen so that it is above the shock wave for all six simulated altitudes listed in Table 1.

The initial conditions for the simulations are split into two categories: large particles (> 1000 amu) and small particles (< 1000 amu). The large particles have 80 initial positions on a uniform grid. A larger number of initial positions are used for the smaller particles as their larger thermal velocity causes more particles to be scattered in and out of the entrance to the MASS instrument. For the small particles, 806 initial positions were used on a uniform grid with 198 of those positions directly above the entrance to the MASS instrument. The collection efficiency is defined by the number of particles falling on a collection plate divided by the total number of particles starting directly above the MASS instrument (198 for the small particles and 80 for the large particles).

The main particles simulated are ice particles; however, nitric oxide ions (NO^+) and water cluster ions were also simulated as they are the major components of the mesospheric ion density. The water cluster ions simulated are those for $H^+(H_2O)_n$, where n is 3, 4, 5, and 6 monomers corresponding to masses of 55, 73, 91, and 109 amu. The collision cross-sections used for the water cluster ions and the nitric oxide are taken from Sternovsky et al. [2001] and Viehland et al. [1995]. Below 82 km, the main component of the ion density is water cluster ions [Gumbel et. al., 2003]. During most mesospheric conditions, the growth of water cluster ions is limited to values between $n = 4$ and $n = 6$; however, during cold summer mesosphere conditions water cluster ions

have been measured in-situ to grow to a maximum of $n = 21$ [Björn and Arnold, 1981; Yang and Castleman, 1991].

Nitric oxide is a common ion in the mesosphere and is the dominant ion species above 82 km [Brasseur and Solomon, 1986]. The second most common ion above 82 km is O_2^+ . Adding these densities together for these two species gives approximately the total ion density at 85 km during the day of $n_i \sim 10^3 \text{ cm}^{-3}$, which increases rapidly with altitude [Keneshea et al., 1970]. The main source of these ions is photoionization from Lyman alpha radiation and complex ion chemistry in the mesosphere. At night the ion density drops by two to three orders of magnitude as the flux of Lyman alpha is only maintained by diffuse scattering by the hydrogen geocorona [Brasseur and Solomon, 1986].

Examples of simulated trajectories of charged aerosol particles in the MASS instrument are displayed in Figure 6. The trajectories of the lighter particles show more variation than the heavier particles as their thermal velocity is larger and they are scattered more by collisions with the background gas. The trajectories for the larger particles are rather smooth as collisions have a smaller impact on the aerosols momentum. Although a large particle's direction of propagation is largely unaffected by collisions, the cumulative drag of collisions nevertheless affects where the charged particles are collected. In Figure 6, a slight focusing effect can be seen for the trajectories corresponding to mass 1500 amu and 11,000 amu as the particles are collected on the second and third plates.

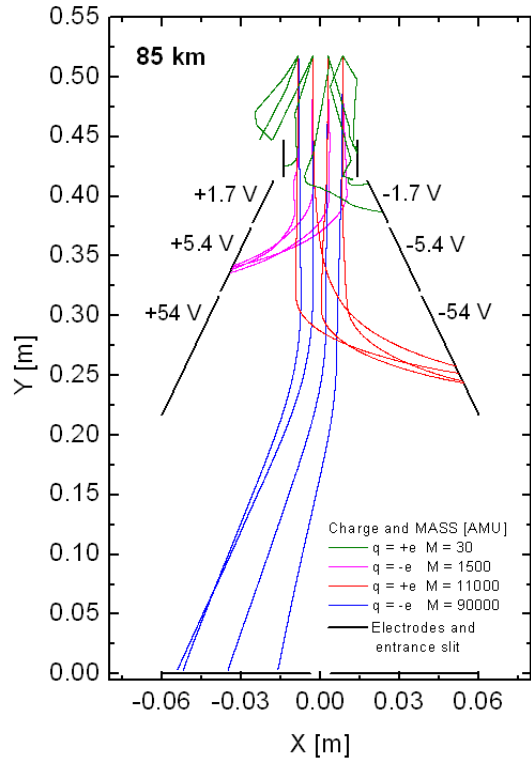


Figure 6. Trajectories of particles within the MASS instrument for four different masses each with four different initial spatial coordinates and thermal velocities. The masses were selected to have a high probability of being collected. They alternate in polarity: $M = 30$ amu and $M = 11,000$ are positive, while $M = 1500$ and $M = 90,000$ are negative. A large fraction of the 30 amu particles are lost to the wall before collection due to their high thermal velocity or collisions.

2.5 NUMERICAL CALIBRATION RESULTS

Collection efficiencies are calculated using the particle trajectory code, which requires inputs from the electric field simulation and the DSMC calculation. The trajectory program calculates collection efficiencies at six different altitudes for 35 masses each averaged over 80 to 806 different initial spatial conditions. The collection efficiencies are defined as the probability that a particle of a given size will be collected by a specific collection plate. Each collection efficiency is the total number of particles

to reach the collection plate divided by the total number of particles with initial positions directly above the entrance to the MASS instrument. The collection efficiency results are listed in Table 2 as a range of particle sizes detected by each graphite collection plate labeled 1-4, where 1 is the collection plate at the top of the MASS instrument. The ends of the collection ranges listed in Table 2 are calculated at the points where the maximum collection efficiency has dropped by a factor of two. The collection efficiencies are plotted as a function of mass and radius in Appendix B for all six altitudes.

Rocket payload potentials on the order of negative one volt relative to the ambient plasma occur commonly in the mesosphere [Friedrich et. al., 1997]. The rocket payload potential has a non-negligible affect on particles collected by the first two MASS collection plates, since their bias voltages are the same order of magnitude as the rocket potential. Collection efficiencies were calculated with a payload potential by including a negative one volt potential drop over a distance of 1 cm above the entrance to the MASS instrument. In both Table 2 and in Appendix B, collection efficiencies are shown in which a payload potential was included. As expected, the payload potential significantly affects the collection efficiency of the first two collection plates within the MASS instrument. The main result of adding a negative payload potential is an increased collection efficiency for small (<1000 amu) positively charged aerosols and a decreased efficiency for small (<1000 amu) negatively charged aerosols. The negative potential leads to a lower detection limit for negatively charged aerosols with a mass of 50 amu at 82.5 km and 200 amu at 90 km. Although electrons were not simulated in the

Altitude [km]	1 [amu]	2 [amu]	3 [amu]	4 [amu]
75	< 120	50-700	700-25,000	> 50,000
75 (+) -1 V	< 130	40-700	700-25,000	> 50,000
75 (-) -1 V	< 80	50-700	600-35,000	> 50,000
80	< 200	200-1,500	1,500-30,000	> 50,000
80 (+) -1 V	< 300	180-1,500	1,500-30,000	> 95,000
80 (-) -1 V	< 250	160-1,500	1,600-22,000	> 90,000
82.5	< 350	350-2,000	2,000-30,000	> 90,000
82.5 (+) -1 V	< 350	300-2,000	2,000-30,000	> 90,000
82.5 (-) -1 V	60-300	300-2,000	2,000-30,000	> 80,000
85	< 600	600-3,000	3,000-30,000	> 90,000
85 (+) -1 V	< 500	500-3,000	3,000-30,000	> 90,000
85 (-) -1 V	< 200	200-1500	1,500-30,000	> 50,000
87.	< 200	200-1500	1,500-30,000	> 50,000
87.5 (+) -1 V	< 200	200-1500	1,500-30,000	> 50,000
87.5 (-) -1 V	< 200	200-1500	1,500-30,000	> 50,000
90	70-800	800-3,000	3,000-25,000	> 85,000
90 (+) -1 V	35-600	600-3,000	3,000-25,000	> 80,000
90 (+) -1 V	200-900	900-3,000	3,000-28,000	> 90,000
Laboratory	N/A	300-2000	2,000-20,000	> 60,000

Table 2. Numerical calibration results at 6 altitudes with and without a payload potential of -1 V. The plate numbers correspond to the graphite collection plates where 1 is the top collection plate in the MASS instrument. The last line in the table is the laboratory calibration results.

particle trajectory program, the above detection limit implies that electrons are not collected. For particles larger than 1000 amu there is no significant effect.

The calibration results are dependent upon multiple variables including the rocket velocity, the air density and the air temperature. The variation of the collection efficiencies with altitude can be explained using these altitude dependent variables. One important variation in the collection efficiencies is the shift of the collection efficiency peaks to heavier masses with increasing altitude (see figures in Appendix B).

The MASS instrument's range of collection for each graphite plate is dependent upon the initial velocity of the entering charged aerosols. If the charged aerosol particle has a low velocity, then it spends more time in the MASS instrument's electric field. As the rocket velocity decreases with increasing altitude, the detection range for each plate is shifted to heavier masses, since the charged particles spend more time in the electric field. This phenomenon occurs for all of the plates with the greatest shift occurring for the first collection plate.

The second important variation in the collection efficiencies with altitude is the change in collection range for each plate: broad range at lower altitudes and narrow range at higher altitudes. At lower altitudes the broad collection range of plates 1, 2, and 3 overlap, while at higher altitudes they do not (see figures in Appendix B). Thus the mass resolution increases with increasing altitude. The broadening of the collection efficiency is best demonstrated by collection plates two and three. As the altitude increases the air density and temperature both decrease, until 90 km, where the temperature begins to increase again. The combination of decreased air density and temperature leads to a decrease in collisions with the background gas. With fewer collisions there is a lower probability for particles to be scattered into or out of their trajectory. As the collision frequency decreases with increasing altitude, the overlap in mass range between collection plates lessens, giving better mass resolution.

All of the collection efficiencies overlap to some extent, except for the third and fourth plates. This gap is due to the large physical separation between plates three and four where the air exit windows are located in the instrument. Also, the collection

efficiencies for plates 1, 2, and 3 start at zero, rise to a peak, and then go back to zero; however, the fourth plate's geometry within the instrument limits the collection efficiency to below fifty percent after its peak collection. The large particles collected on the bottom two plates of MASS are not deflected by the static electric field and thus fall directly onto the plates, where each one of the plates collects half of the current. In the limit of no deflection, the collection efficiency for the bottom two plates would be 37.5%. This percentage is the ratio of the area of the collection plate directly below the opening of the mass instrument to the area of the opening.

The first collection plate shows the most variation in collection efficiency as a function of altitude. At 75 km, the first plate has limited collection efficiency as most of the particles are being collected by the second plate. At lower altitudes it is more difficult to deflect charged aerosols towards the graphite collection plates as they spend less time in the static electric field due to the increased rocket velocity. The collection efficiency improves with altitude, reaching a maximum value at 85 km. The first plate's collection efficiency decreases with increasing altitude above 85 km. For example, the collection efficiency for a 30 amu ice particle at 90 km is 26%. This drop in collection efficiency is related to the thermal velocity of the lightest particles carrying the majority of the particles into the walls at the entrance to the MASS instrument as seen in Figure 6.

In addition to ice particles, water cluster ions and nitric oxide were modeled in the particle trajectory code as these particles are the two main components of the mesospheric ion density. The water cluster ions have a collision cross-section that is

typically three times larger than an ice particle with the same mass. As a result, the water cluster ions collection is shifted from the first plate at 90 km to the second plate at 80 km. The increase of collisions at lower altitudes causes the water cluster ions to be more fixed to the flow field and harder to deflect. In contrast, the nitric oxide collision cross-section is half as large as an ice particle with the same mass. Therefore, the collection efficiency of nitric oxide is less affected by the changing collision frequency with altitude and is collected by the first plate even at an altitude of 75 km.

The calibration results for the MASS instrument show that the collection efficiencies for each mass range vary as a function of many parameters, including rocket velocity, air density and air temperature. The effects of collisions and payload potentials have been included in the collection efficiency calculations. In general, it can be stated that the approximate MASS instrument collection range for ice particles is $r < 0.5$ nm for plate 1, 0.5-1 nm for plate 2, 1-2 nm for plate 3, and >3 nm for plate 4 between 80 and 90 km. Using $I = fqnvA$ (Eq. 2.1), these calculations provide us with f , the collection efficiency, and the mass range for each MASS channel. As a result the number density of charged aerosols collected by each plate can be adjusted by the peak collection efficiency to determine a more accurate charged aerosol density.

CHAPTER 3: MASS FLIGHT DATA

The NASA sponsored MASS instrument was part of a joint rocket campaign called the MASS/ECOMA (Existence and Charge state Of meteor smoke particles in the Middle Atmosphere) sounding rocket campaign which took place at the Andoya Rocket Range, Norway in August, 2007. The purpose of the MASS campaign was to provide in-situ measurements of the number density of charged aerosols responsible for NLC/PMC and PMSE. To maximize the scientific returns from the sounding rocket flights (1) a comprehensive payload was developed, (2) the flights occurred nearly coincident with the German-Norwegian ECOMA rocket campaign and with observations from the AIM (Aeronomy of Ice in the Mesosphere) satellite, and (3) the location was chosen to have simultaneous measurements from ground-based lidar and radar. In the following sections the MASS payload, the ground based support equipment at the Andoya rocket range, the flight data, the flight performance, and the coincident AIM data will be discussed.

3.1 MASS PAYLOAD

Two sounding rockets were launched with identical MASS payloads, one on August 3, 2007 and the other on August 6, 2007. The MASS payload consisted of four sections: the forward experimental section, the telemetry system, the attitude control

system (ACS), and the aft experimental section. The forward and aft experimental sections are shown in Figures 7 and 8. The forward experimental section included the MASS instrument to measure both positive and negatively charged aerosol particles in four ranges of mass, the electric field booms to measure the electric potential both in and out of the perturbed flow around the payload, the Colorado Dust Detectors to measure the charged fraction of aerosol particles, and the Faraday rotation experiment to measure the electron density. The aft experimental section included the photometer for measuring the number density and size distribution of ice particles by Mie scattering and a pair of electric field booms. The telemetry system consisted of a data acquisition system, a Global Positioning System (GPS) and a RF transmitter. The science data channels in the telemetry system included 48 high accuracy analog channels, 4 standard analog channels, and 1 counter. The ACS included a Bartington 3-axis magnetometer for improved attitude control and flight data. The fundamental operation of the MASS instrument has been previously explained in Chapter 2; however, there are several flight effects that will be discussed at the end of Chapter 3. These flight effects include microphonic noise, spurious charge generation, and photoelectric currents. The other payload instruments will be described in the following paragraphs.

3.1.1 FARADAY ROTATION ANTENNAS

The Faraday rotation experiment and an RF transmitter were provided by Martin Friedrich from Graz University of Technology to measure the electron density as a

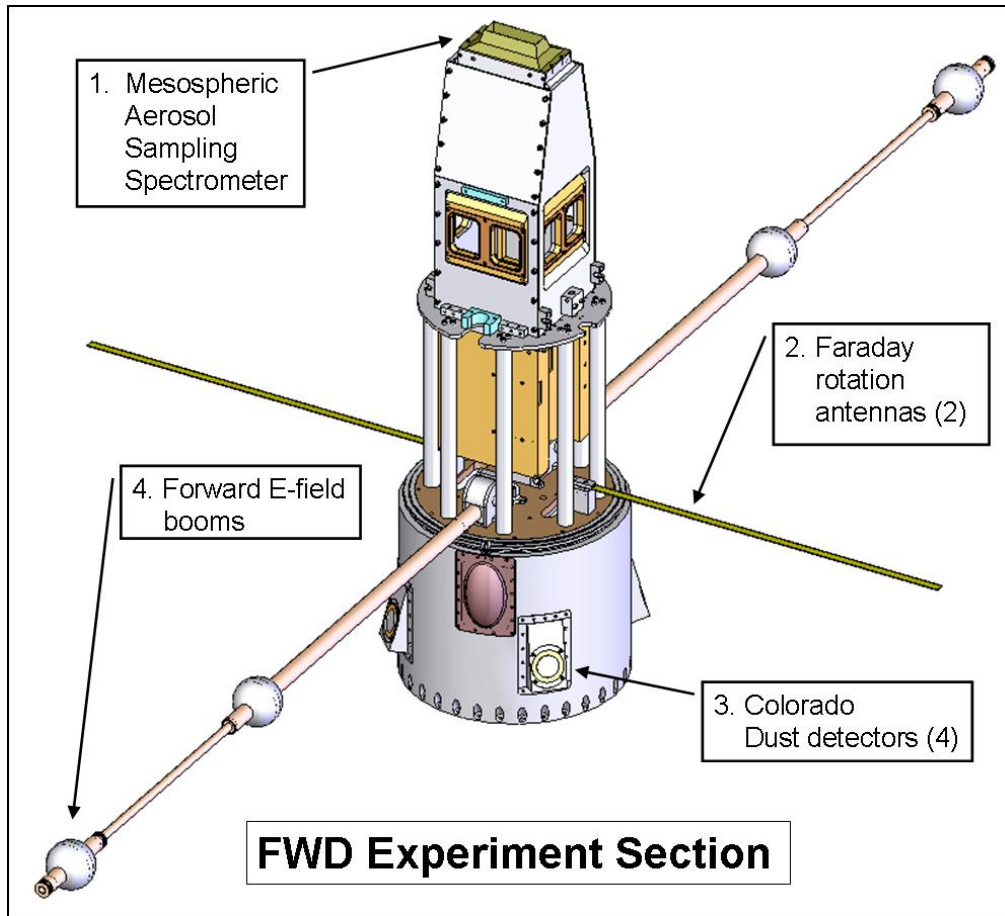


Figure 7. Engineering drawing of the forward payload section consisting of four instruments: MASS, Faraday rotation antennas, Colorado Dust Detectors (CDD), and the forward set of electric field booms.

function of altitude. The RF transmitter sends four linearly polarized waves of different frequencies between 1.3 and 7.835 MHz to the rocket Faraday rotation antennas. The pair of receiving dipole antennas rotate with the rocket at 2 Hz, which results in a received signal with two maximum and two minimum each spin period. The linearly polarized wave can be deconstructed into two circularly polarized waves, one right handed and the other left handed. The circularly polarized wave propagating with the electric field vector rotating in the same direction as the electrons travels faster than the

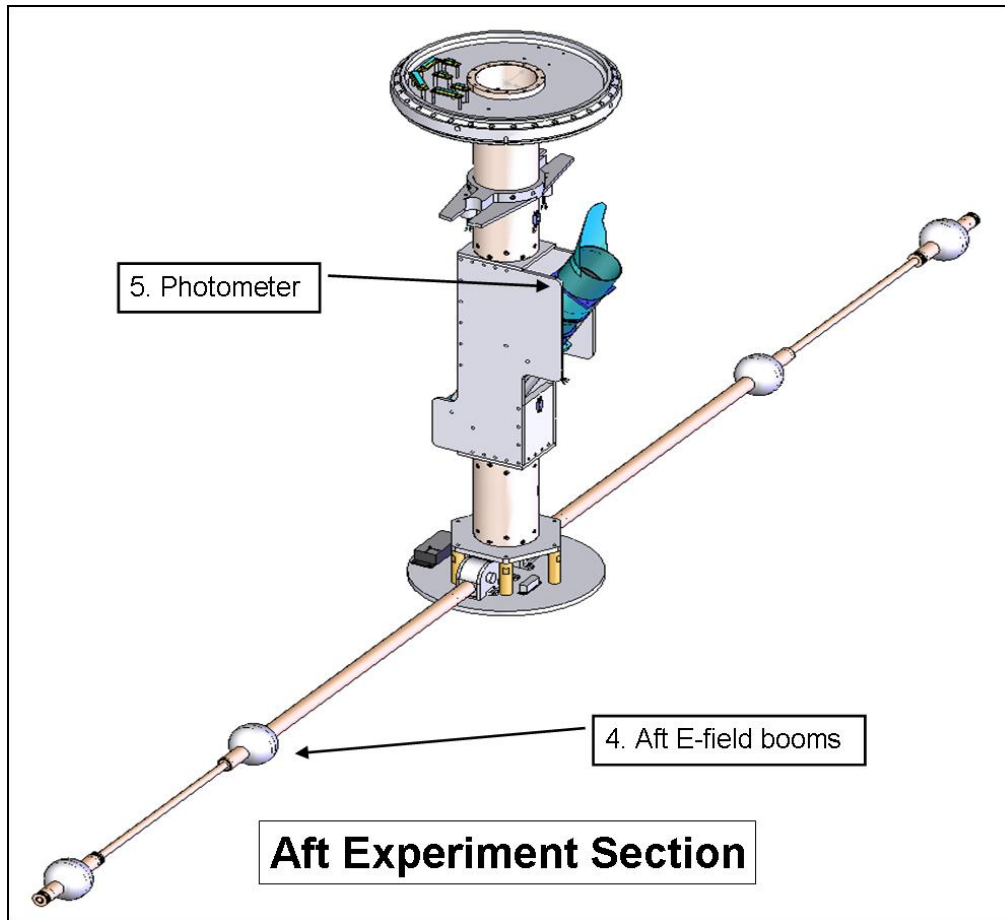


Figure 8. Engineering drawing of the aft payload section consisting of two instruments: the aft set of electric field booms and the photometer.

circularly polarized wave traveling opposite the electrons, resulting in a rotated linearly polarized wave. The amount of Faraday rotation is proportional to the strength of the magnetic field and the integrated electron density over the propagation length [Mechtly, 1974; Jacobsen and Friedrich, 1979]. The magnetic field is well characterized in the ionosphere, and therefore the electron density can be calculated. The Faraday rotation measurement is also compared to the differential absorption of the four propagation waves [Bennett et al., 1972; Mechtly et al., 1967]. Once the frequency of the propagating wave is less than the plasma frequency the wave is reflected and does not

reach the rocket. At the point where the signal reaches zero, the plasma frequency is thus known and the electron density can be calculated. The Faraday rotation experiment has been flown on eight previous rockets at the Andoya Rocket Range [Friedrich et al., 2009] and many more at other locations.

3.1.2 COLORADO DUST DETECTORS

Four Colorado Dust Detectors (CDD) were provided by the University of Colorado at Boulder. The CDD are charged dust detectors that utilize a permanent magnet to deflect electron collection and can be biased to repel light ions. On the MASS payload, two CDD had zero bias and two CDD were biased +2 V. The CDD measure the current produced by the incident charged particles, which is used to determine the charged number density of particles as a function of altitude. The charge number density is calculated similarly to the MASS charge number density using: the rocket velocity, the area of the collector, and the assumption that the particles have a single charge. The CDD have been flown on seven successful flights including MIDAS/SOLSTICE [Smiley et. al, 2003] and MIDAS/MaCWAVE [Smiley et. al, 2006]. In previous flights, the CDD were mounted flush to the rocket skin. For the MASS payload the CDD were mounted on holders that extended them 15° out from the rocket skin to expose the detectors to the air flow. The attitude control system for MASS keeps the rocket pointed in the ram direction limiting the exposure of the CDD if they were not extended into the flow. The CDD data will not be discussed as large unexplained charge number densities were measured.

3.1.3 *ELECTRIC FIELD BOOMS*

The electric field booms are a set of four high impedance Langmuir probes provided by Bob Holzworth and Michael Shimogawa from the University of Washington. Two probes were in the forward payload section and two in the aft payload section. The mechanical design for the spherical probes and the booms were identical to those used during the DROPPS rocket campaign [Holzworth et al., 2001], while the electronics were slightly modified from the DROPPS configuration. The electronics consisted of a high-impedance preamp in each spherical probe connected to the electronics box which contained an amplifier module. The electric field booms were added to the payload to measure the large amplitude geophysical electric fields and to measure the smaller AC fluctuations in the electric field [Shimogawa and Holzworth, 2009]. The electric field booms also investigated electric fields created by the shock wave around the payload. Previously during the DROPPS rocket flights, large voltage fluctuations were seen by the aft probes [Holzworth and Goldberg, 2004]. These fluctuations were caused by the probes moving in and out of the rocket wake [Holzworth et al., 2001; Sternovsky et al., 2004]. During the MASS flights no large voltage fluctuations were seen by the aft probes.

3.1.4 *PHOTOMETER*

A photometer was provided by Jorg Gumbel and Linda Megner from the University of Stockholm, Sweden, to measure the scattered light from NLC particles as a function of altitude. The photometer measurement complements the ALOMAR lidar

measurements in determining the range over which the NLC particles are present. In addition, the photometer provides NLC particle size distributions and an average NLC radius derived using multiple scattering angles sampled as the photometer rotates on the rocket payload. The photometer on the MASS payload has a spin rate of 2 Hz and scanned solar scattering angles from ~40 to 110 degrees. The photometer consisted of a set of baffles, an interference filter, an objective lens, a mirror, a field lens, and a photomultiplier. The main change from previous photometers was an improved baffle system [Gumbel et al., 2001]. During the first flight an optical scattering radius of ~50 nm with 10 cm^{-3} was deduced from the scattered radiance [Megner et al., 2009]. Note, the calculations of particle radii are dependent upon scattering cross-sections which have an r^6 power dependence, where r is the radius of the particle. Therefore, optical measurements like the photometer cannot be compared to measurements like the MASS instrument as the photometer is not able to resolve the density of small particles. The photometer data will be discussed in more detail in section 3.6.

3.2 MASS LAUNCH SITE

The Andoya Rocket Range, Norway was chosen as the launch site due to the excellent ground based support equipment available at the Arctic Lidar Observatory for Middle Atmosphere Research (ALOMAR); namely, the ALOMAR WIND radar (ALWIN) and the ALOMAR Raleigh/Mie/Raman (RMR) lidar. The ALWIN radar is a VHF Mesosphere Stratosphere Troposphere (MST) radar which was installed in 1998. The radar has a peak power of 36 kW, operates at a frequency of 53.5 MHz, has a

minimum range resolution of 150 m, and is composed of 144 four-element Yagi antennas [Latteck, 1999]. The ALWIN radar provides unattended radar operations with high reliability for determining horizontal wind speeds and determining the echo power from PMSE.

The ALOMAR RMR lidar provides measurements of temperature profiles, stratospheric winds, and multiple cloud properties including their altitude, particle density, and size distribution. The lidar system is a set of two independent Nd:YAG lasers operating at three wavelengths: 355, 532, and 1064 nm in combination with two tiltable receiving telescopes [von Zahn, 2000]. Both the ALOMAR RMR lidar and the ALWIN radar were utilized on the days of the MASS launches to determine whether the launch conditions were met. The launch conditions observed by both of these instruments will be discussed in the flight data sections 3.3 and 3.4.

3.3 MASS FLIGHT 1 DATA

The MASS instrument was launched during the NLC season on two sounding rockets and returned data on both the upleg and downleg of each flight. The MASS data for the first launch will be presented in this section and the second flight in section 3.4. The MASS data channels will be presented in order of increasing mass. The lowest-mass channel collecting positive and negative charge are labeled 1+ and 1-, respectively, and the highest-mass channels are labeled 4+ and 4-. The flight requirements for the first launch were to fly into an NLC and a PMSE, while the requirements for the second flight were to fly only into a PMSE. The different flight requirements allow for a

comparison between charged particle distributions with NLC and with PMSE. The conditions for both flights were verified by the ALOMAR ground support equipment. The MASS launch window was chosen to be the first two weeks of August because it was still within the NLC season. In addition, the MASS launch coincided with the ECOMA launch and an Aeronomy of Ice in the Mesosphere (AIM) satellite flyover. The first MASS rocket was launched on August 3, 2007 at 22:51:20 UTC reaching an apogee of 133.3 km. The solar zenith angle was 93.2 degrees, corresponding to twilight conditions. The rocket velocity dropped from 1106 m/s at 80 km to 1018 m/s at 90 km. The MASS rocket was launched into a PMSE observed by the ALWIN radar and a NLC observed by the ALOMAR RMR-Lidar. The ALWIN radar data for the fifteen minute period nearest the launch are shown in Figure 9. The radar back-scatter shows a double structure PMSE with peaks at 83 and 88 km. A PMSE double structure is commonly observed [Hoffmann et al., 2005]. At the time of launch, the ALOMAR RMR-Lidar was unable to make NLC measurements due to tropospheric clouds. Approximately five minutes before launch, the RMR-Lidar measured a weak NLC at 82 - 84 km with a peak backscatter coefficient of $3.3 \times 10^{-10} \text{ (m sr)}^{-1}$ at 82.8 km. The Lidar data are also shown in Figure 9 along with the radar data. For more details on the Lidar data during the ECOMA/MASS campaign see Baumgarten et al. [2009]. Many common features appear in the radar, lidar, and MASS data, which will be discussed as the MASS data is presented.

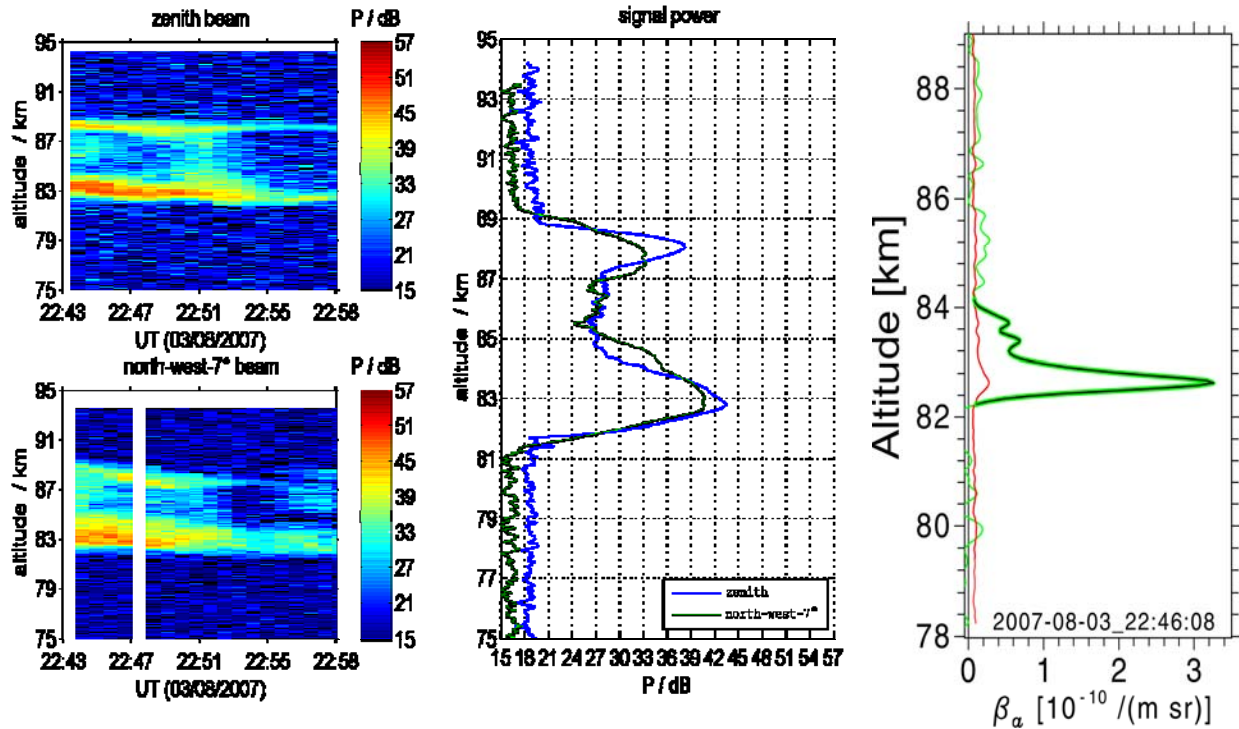


Figure 9. ALWIN radar and ALOMAR RMR-Lidar data for the first MASS launch occurring on August 3, 2007 at 22:51:20 UTC. The two plots on the left show the radar data for the fifteen minute period nearest the MASS1 launch for the zenith beam and the north-west beam. The plot in the middle shows the radar data for the two radar beams at the launch time. The plot on the right shows ALOMAR RMR Lidar measurements of aerosol backscatter coefficients (green) integrated over one minute for the MASS1 launch.

3.3.1 CHANNELS 1+ AND 1-

The MASS channels 1+ and 1- are designed to measure light molecular ions and electrons, respectively. However, electrons have a high probability of hitting the entrance of the MASS instrument due to the electron's large thermal velocity relative to the rocket velocity. In addition, the electrons are repelled by the negative payload potential as discussed in section 2.5. Therefore the collection of electrons is suppressed. Electron densities are, however, measured by the Faraday rotation experiment. The suppression of electron collection by the MASS instrument can be seen at 90 km where

the Faraday rotation antennas measured electron densities $\sim 12,600 \text{ cm}^{-3}$, while the MASS 1- channel measures densities below $\sim 200 \text{ cm}^{-3}$, see Figures 10 and 11.

Assuming that the plasma in the D-region of the ionosphere is quasi-neutral, the electron density should track the ion density as long as the number density of charged aerosols is small. The electron density measured by the Faraday rotation antennas and the positive ion density measured by the 1+ channel of the MASS instrument for the upleg of the first flight from 74 to 100 km are shown in Figure 10. The positive ion density is calculated using a collection efficiency of $f = 0.64$, which corresponds to the collection efficiency for NO^+ at 90 km. The dominant ion at this altitude is NO^+ as measured by multiple rocket-borne mass spectrometers [e.g. Bragin and Shamakhov,

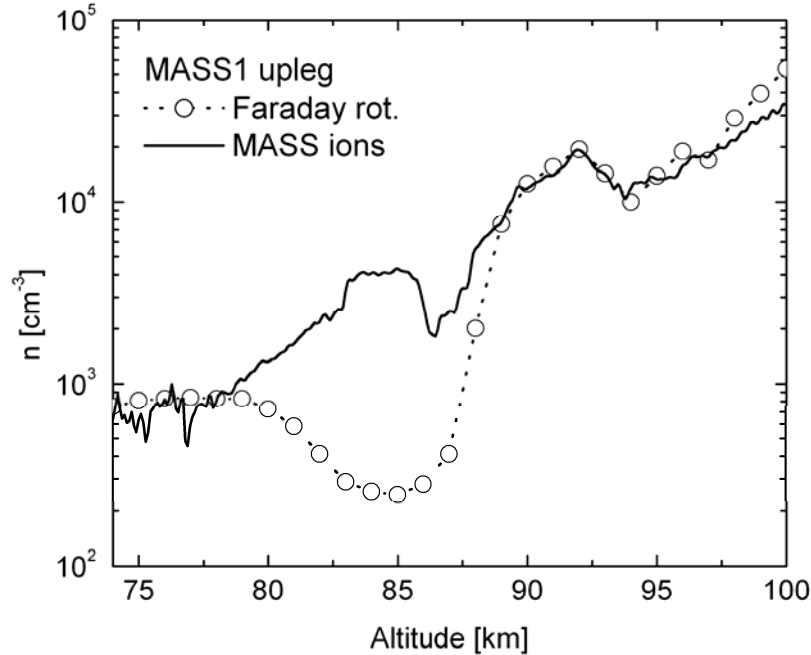


Figure 10. The electron density from Faraday rotation and the positive ion density measured by the MASS instrument channel 1+ during the MASS1 upleg.

1982; Krankowsky, 1987]. The ion density tracks the electron density both below and above the PMSE. The electron density is reduced between 78 and 88 km and there is a large bite-out between 83 and 87 km. Electron bite-outs occur during PMSE approximately 20% of the time [Blix et al., 2003]. The maximum depletion of the electron density occurs at 85 km where the electron density is $\sim 250 \text{ cm}^{-3}$, while the ion density is $\sim 4000 \text{ cm}^{-3}$. This implies that the maximum reduction in the electron density is approximately 94%. The location of the electron reductions correlates with the observed radar backscatter measured by ALWIN, shown previously in Figure 9. Although the electron reduction begins at 78 km, the PMSE radar backscatter is not prominent until 82 km. This discrepancy is likely related to the uncertainty in the electron and ion densities at these altitudes. The uncertainty in the electron density measured by the Faraday rotation antenna at lower altitudes ($\sim 80 \text{ km}$) is due to a large collision frequency [Friedrich et al., 2009]. The uncertainty in the positive ion density measured by the MASS instrument is due to the varying collection efficiency, which is dependent upon temperature, air number density, and which ion species is dominant.

The upleg data for the 1+ and 1- channels of the MASS instrument are shown in Figure 11 along with channels 2 \pm , 3 \pm , and 4 \pm . The 1+ channel collects light positive ions increasing smoothly in density below 83 km and above 88 km. Between 83 and 88 km the 1+ channel measures both an ion density enhancement (83-86 km) and an ion density deficit (86-88 km). The ion deficit overlaps with a positive charge density enhancement seen on the 2+ and 3+ channels of the MASS instrument, thus accounting

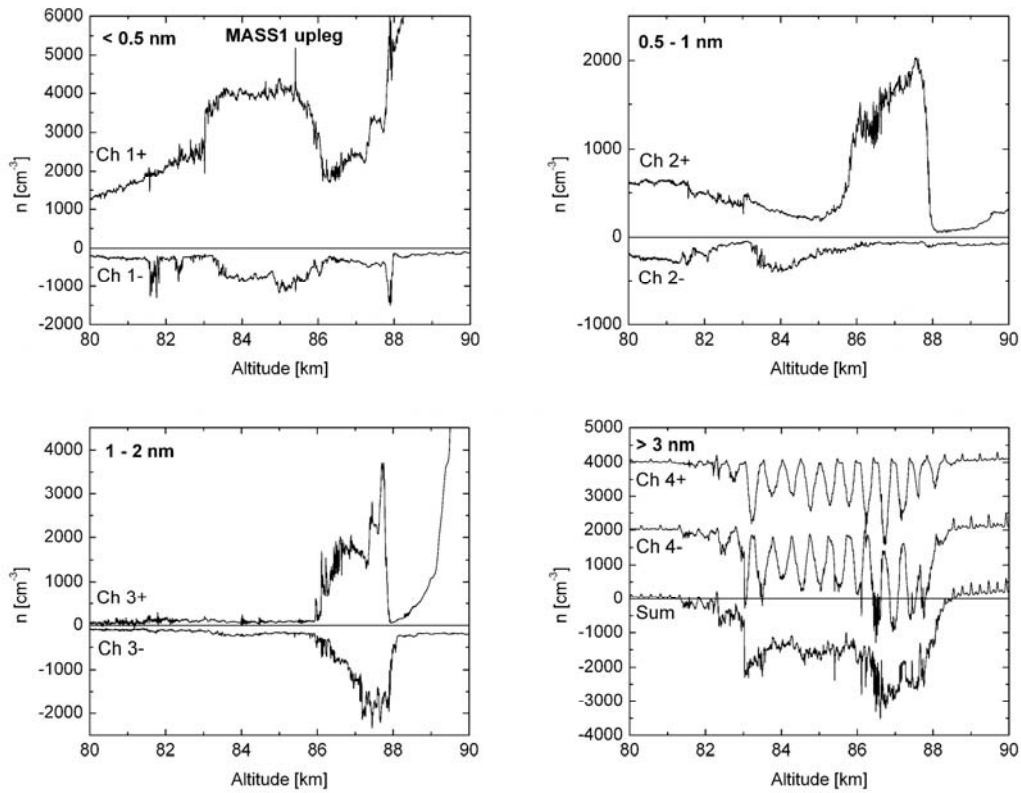


Figure 11. Data from the 8 channels of the MASS instrument for the upleg of the first flight. Channels 4+ and 4- are offset from zero for clarity and their sum is plotted with no offset.

for the missing charge. Depletion of positive ion densities has been observed within NLC before [Balsiger et al., 1996].

The downleg data for the 1+ and 1- channels of the MASS instrument are shown in Figure 12 with all of the MASS channels. The downleg data for the 1+ MASS channel shows a similar positive ion density profile as the upleg, although the downleg ion density has less of an enhancement between 83 and 85 km compared to the upleg density. There is a local deficit between 85 and 86 km in the downleg ion density, which coincides with an enhancement in positive charge density measured by the MASS 2+ channel. The downleg data shows similarities to the upleg data; however,

their signals are not expected to be identical as the volume sampled is separated horizontally by 90 km and the mesospheric environment is highly variable.

The upleg data for channel 1- show negative charge density spikes up to 1000 cm^{-3} at ~ 82 and ~ 88 km. There is also a small region of enhanced negative charge density between 83 and 86 km on the channel 1+ data. The negative ion densities at these altitudes should be negligible [e.g. Thomas and Bowman, 1985]. The measured negative charge densities cannot be electrons as their collection is suppressed; however, the negative densities could be attributed to negative molecular ions. Negative molecular ions have been measured previously by ion mass spectrometers [Schulte and Arnold, 1992]. The MASS instrument determines the charge-to-mass ratio of a charged particle, which is not enough information to distinguish molecular ions from NLC particles. Therefore these particles can not be definitively identified as negative molecular ions, NLC particles, or other charged mesospheric constituents. The downleg data from channel 1- measures negative charge densities below 200 cm^{-3} , which indicates that negative ions are nearly absent as expected.

3.3.2 CHANNELS 2+ AND 2-

The MASS channels 2+ and 2- measure positive and negative particles within the approximate range of 0.5 – 1 nm in radius assuming NLC ice particles are collected. The 2+ channel of the MASS instrument measured a distinct positive charge layer with a maximum density of 2000 cm^{-3} between 86 and 88 km, which coincides with the previously mentioned deficit in positive charge measured by the 1+ channel. Above

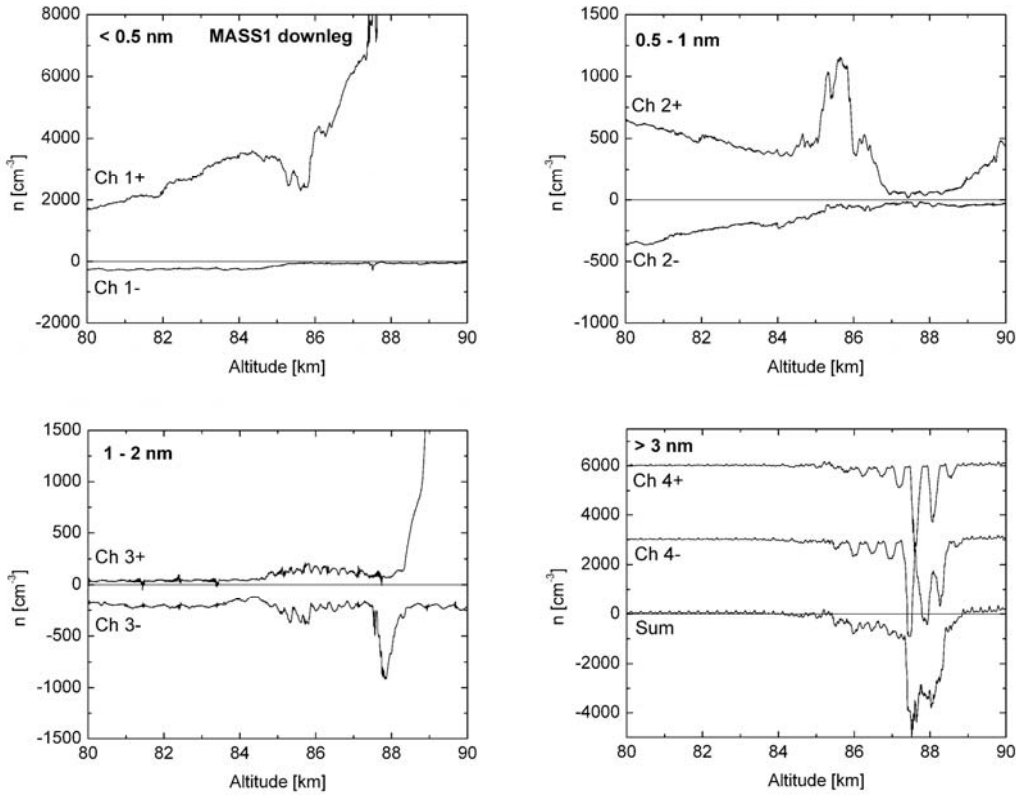


Figure 12. Data from the eight channels of the MASS instrument for the downleg of the first flight. Channels 4+ and 4- are offset from zero for clarity and their sum is plotted with no offset.

this layer the positive charge density drops below 100 cm^{-3} . Below the positive charge layer there is a nearly constant density ($\sim 500 \text{ cm}^{-3}$) of positive charge from 73 to 83 km. The collection efficiency of water cluster ions at 75 km is split between MASS channels 2+ and 3+. However, the MASS 3+ channel does not measure a positive charge density equal to the 2+ MASS channel at 75 km, implying that the positive charge density is not composed of water cluster ions. This is an interesting measurement, as typically water cluster ions are the dominant ions below 80 km. At 80 km, the collection efficiency for water cluster ions collected on channels 2+ and 3+ are 60% and 20%. At 80 km the 2+ channel measures a positive charge density of $\sim 600 \text{ cm}^{-3}$, while the 3+ channel measures

a positive density of $\sim 50 \text{ cm}^{-3}$. The positive density of particles measured on the 2+ channel can not be attributed to NO^+ (which is collected only by the 1+ MASS channel) or water cluster ions, leaving the most likely explanation being positively charged meteoric smoke particles. Especially below 80 km, the temperature is too high for ice particles. The MASS instrument is not capable of identifying specific ions, but by using the modeled collection efficiencies of the dominant ions this charge distribution below 83 km is likely charged meteoric smoke.

The 2+ channel on the downleg measured a similar profile as measured on the upleg. Again, a distinct positive charge layer was measured, but shifted to lower altitudes between 85 and 86 km. The positive charge layer again coincided with a deficit in positive charge measured by the 1+ channel on the downleg. There was also a nearly constant population of positively charged particles between 75 and 85 km with density again near $\sim 500 \text{ cm}^{-3}$.

The 2- channel of the MASS instrument measured a small population of negatively charged aerosols with a maximum density near 400 cm^{-3} at 84 km. The negative population does not mirror the positive population measured on the 2+ channel. The 2- channel on the downleg measured no signal indicating a negative charge layer.

3.3.3 CHANNELS 3+ AND 3-

Channels 3+ and 3- collect charge particles in the range of 1 – 2 nm in radius assuming ice particles are collected. The 3+ and 3- channels measured minimal number

densities below 86 km and then between 86 and 88 km a distinct layer of both positive and negative particles were measured with a charge number density of $\sim 2000 \text{ cm}^{-3}$. After 88 km the measured charge densities return to near zero density levels. Then the 3+ channel abruptly increases with altitude reaching densities above 6000 cm^{-3} at 90 km. This abrupt increase in the measured positive charge density by the 3+ channel is a result of light positive ions entering the -10 V biased window grids and being deflected towards the 3+ channel where they are collected. The 3+ channel has the largest negative bias of -54 V. The light ions are able to pass through the biased window grids due to a decreased rocket velocity and an increase in temperature. Just above 90 km, the 3+ channel saturates due to the light ions entering through the biased windows. The 3+ channel remains saturated until 90 km on the downleg as seen in Figure 12.

The channels 3+ and 3- for the downleg measure significantly lower number densities of charged aerosols than for the upleg. The 3+ channel below 89 km measured a positive density below 200 cm^{-3} with no distinct positive charge layer as measured on the upleg. The 3- channel did measure a negative charge layer similar to the upleg measurement, but with a density reduction of a factor of two and a much more narrow layer. The reduction in charge number densities is attributed to the NLC being weaker at the downleg location.

3.3.4 CHANNELS 4+ AND 4-

The MASS channels 4+ and 4- are designed to measure NLC ice particles with radii greater than 3 nm. NLC particles above 10 nm in radius may be multiply charged;

therefore, the number density of NLC particles measured by the 4+ and 4- channels may be lower than the equivalent charge density. The upleg data from the 4+ and 4- channels are shown in Figure 11 and the downleg data are shown in Figure 12. In both figures the channels are shown separated by offsets and shown combined without an offset. The 4+ and 4- channels both measure negative charge densities ($\sim 2000 \text{ cm}^{-3}$) starting abruptly at 83 km and ending abruptly at 88 km. The sudden change in negative charge densities measured by channels 4+ and 4- correlate with the peaks at 83 and 88 km in the PSME radar data. The location of the NLC as measured by the Lidar is just below 83 km where the onset of negative charged particles measured by the 4+ and 4- channels appears. The Lidar measuring volume is ~ 10 km away from the rocket trajectory [Baumgarten et al., 2009] and the Lidar measurement was made five minutes before the rocket launch.

Between 83 and 88 km, the 4+ and 4- channels are observed to oscillate $\sim 180^\circ$ out of phase at the rocket rotation frequency of 2 Hz. The most likely explanation is the charged particles entering the MASS instrument have a velocity vector pointing slightly away from the rocket axis of symmetry. This causes the charged particles to be collected on the 4+ channel and then a quarter of a second later to be collected on the 4- channel when the rocket has rotated 180° . The MASS payload included an attitude control system maintaining the pointing of the MASS instrument in the ram direction, excluding coning as an explanation for the oscillating signals. The additional velocity shifting the charged particles from the ram direction is likely due to a wind perpendicular to the rockets' trajectory. The combined meridional and zonal winds

measured by the ALOMAR meteor radar above the Andoya rocket range during the rocket flight vary from 30 to 40 m/s [Baumgarten et al., 2009]. Numerical particle trajectories through the MASS instrument were calculated including the wind velocity demonstrating the feasibility of channels 4+ and 4- being 100% modulated as measured. The numerical calculations including the wind velocity were done for all 35 previously modeled masses. Particles collected on channels 1±, 2±, and 3± are not modulated by the wind and the rocket rotation as their collection is dominated by the electric field within the MASS instrument. The particles collected on the 4+ and 4- channels are greater than 90,000 amu and have such large inertia they are not deflected. The numerical simulations revealed that particles below 7 nm in radii were not modulated completely as measured on the 4+ and 4- channels due to the MASS electric field. This indicates that the collected particles are larger than 7 nm in radius.

The channels 4+ and 4- on the downleg measure a similar modulation in negative charge number density, again implying collection of particles greater than 7 nm in radius. The altitude range over which particles were detected was diminished on the downleg. A distinct negative charge layer was measured between 87.5 and 88.5 km with charge number density of 4000 cm⁻³. The upleg measured charged particles with radii greater than 7 nm from 83 to 88 km with a density of 2000 cm⁻³ with a maximum density of 3000 cm⁻³ at 86.5 km. The difference in number densities between upleg and downleg are attributed to a weaker NLC at the downleg location.

3.4 MASS FLIGHT 2 DATA

The second MASS launch took place on August 6, 2007 at 22:56:00 UTC at the Andoya Rocket range. The launch requirements were to fly into a PMSE without the presence of a NLC. The rocket reached an apogee of 131.6 km and the rocket velocity dropped from 1077 m/s at 80 km to 985 m/s at 90 km. The second launch was also done under twilight conditions with a SZA of 94.3°. The PMSE measured by the ALWIN radar during the launch extended from 83 to 89 km with a peak at 87 km. The PMSE reflected power during the second MASS launch was 25% stronger than the PMSE during the first launch. The ALOMAR RMR lidar did not detect a NLC, the signal detected was 40 times lower than the statistical threshold for NLC [Fiedler et al., 2009]. The second MASS rocket was launched under these conditions, which are shown in Figure 13.

Before launch and during the entire flight the channel 2+ in the MASS instrument returned a saturated signal, indicating a malfunction. The rest of the MASS channels worked as expected for both the upleg and downleg. The channel 2+ typically provides a -5.4 V bias to the 2+ graphite collection plate. The malfunction on the 2+ channel indicates a possible lost bias voltage on the 2+ graphite collection plate. The collection plates above 2+ gave signals which appeared to be unaffected. The collection plates below the 2+ plate have the largest bias voltages, which are ten times larger than -5.4 V. Thus the third and fourth pairs of collection plates are assumed to have a negligible change in their collection range.

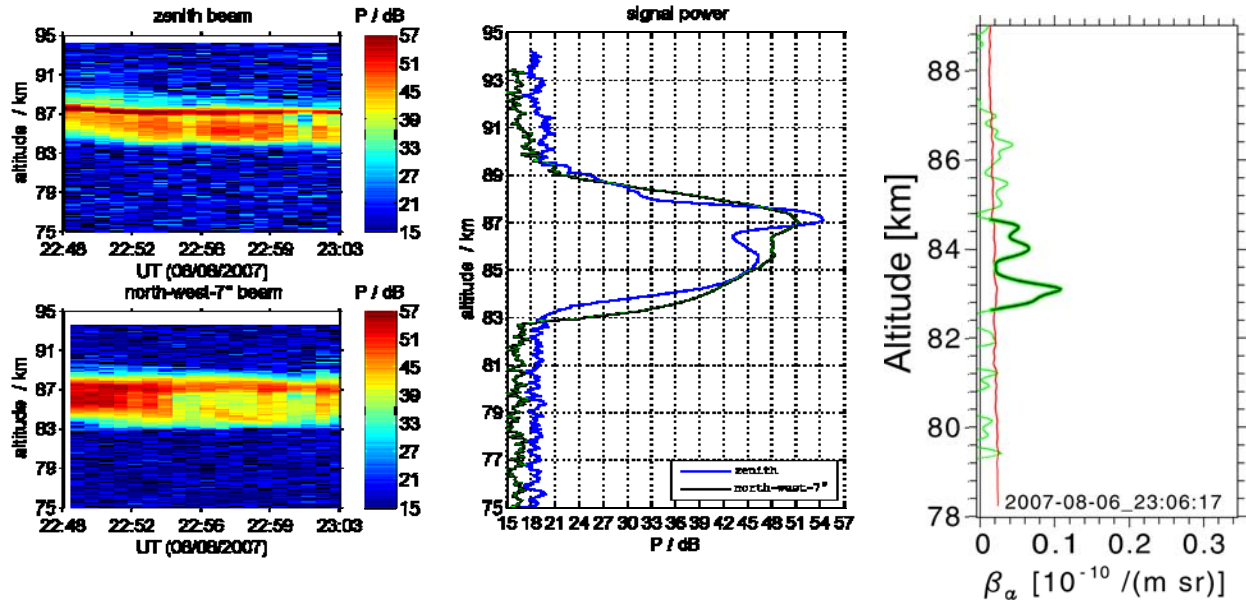


Figure 13. ALWIN radar and ALOMAR RMR Lidar data for the second MASS launch occurring on August 6, 2007 at 22:56:00 UTC. The two plots on the left show the radar data for the 15 minute period nearest the MASS launch for the zenith beam and the north-west beam. The plot in the middle shows the radar data for the two beams at the launch time. The plot on the right shows the RMR Lidar backscatter coefficient integrated over a 14 minute period closest to the MASS launch.

3.4.1 UPLEG DATA: CHANNELS 1± THROUGH 4±

The upleg data from the second MASS flight is shown in Figure 14. The channel 1+ on the upleg of the second flight measured an exponentially increasing ion current, which is in agreement with the Faraday rotation measurement of electron density above 87 km, shown in Figure 15. The discrepancies between the electron and ion measurements below 87 km are again attributed to uncertainties in the ion collection efficiencies and in the Faraday wave propagation due to large collision frequencies. Both measured electron and ion densities were monotonically increasing and never indicated a bite-out, unlike the first MASS flight. There is a sharp increase in ion and

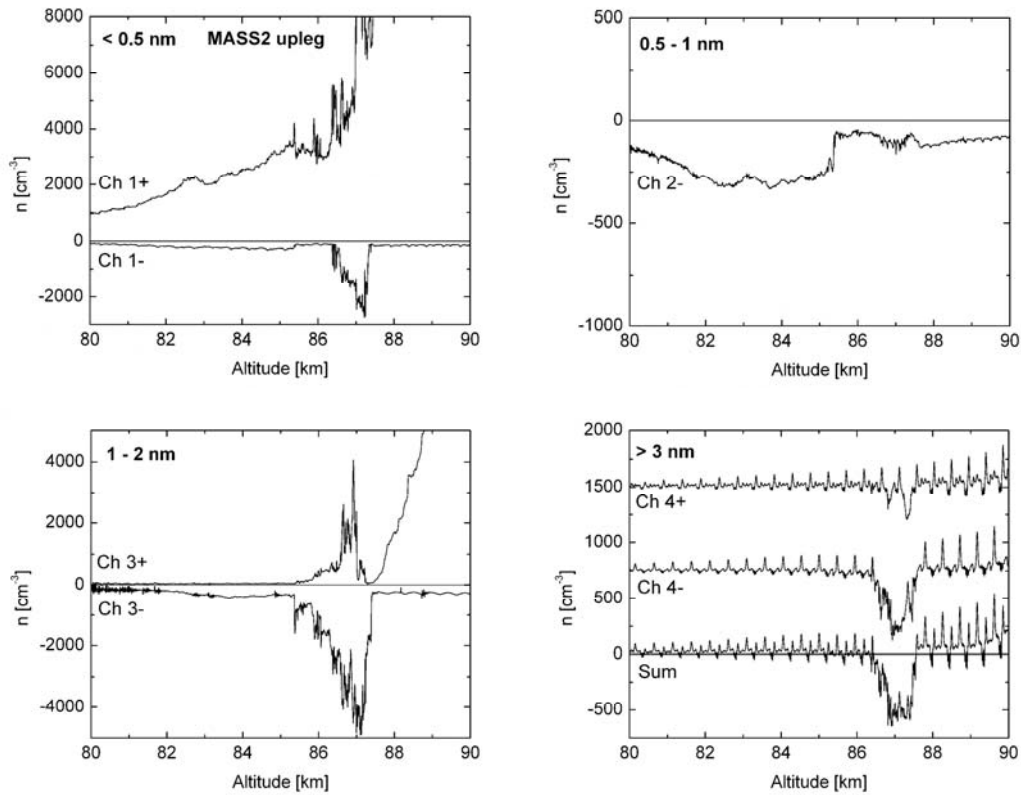


Figure 14. Data from the 8 channels of the MASS instrument for the downleg of the first flight. Channels 4+ and 4- are offset from zero for clarity and their sum is plotted with no offset.

electron density at 87 km, which coincides with the peak ALWIN radar signal. The MASS channel 1- measured a small charge layer between 86 and 87.5 km. The MASS channel 2- appeared to be unaffected by the malfunction on channel 2+. The channel 2- measured a small charged density ($\sim 250 \text{ cm}^{-3}$) similar to that measured during the first MASS flight, which again dropped off near 86 km.

The third pair of collection plates on the MASS instrument both measured charge layers between 85 and 87 km. The 3- channel measured a large negative layer with peak density near 5000 cm^{-3} , which is nearly twice the measured density during the first

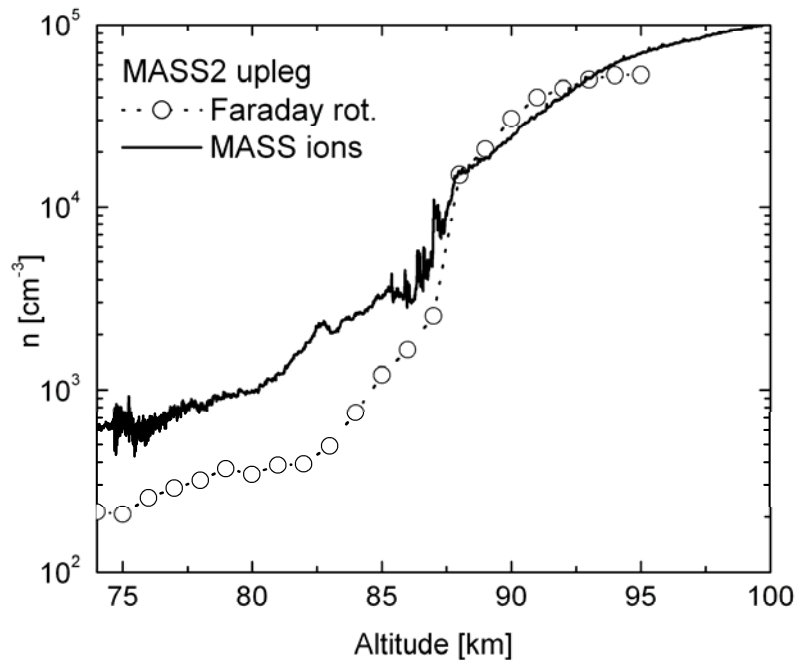


Figure 15. The electron density from the Faraday rotation experiment and the positive ion density measured by the MASS instrument channel 1+ during the upleg of the second MASS flight.

MASS flight. The 3+ channel measured a positive layer with average density near 1000 cm^{-3} with a very narrow layer reaching a density of 4000 cm^{-3} .

The bottom pair of collection plates 4+ and 4- measured a significantly smaller charge layer than that of the first MASS flight, $\sim 500 \text{ cm}^{-3}$ versus $\sim 3000 \text{ cm}^{-3}$. For the second MASS flight the thickness of the charge layer measured by the bottom plates was also significantly smaller, 1 km versus 5 km. The residual oscillation on the bottom plates is assumed to be from photo-charging from Lyman Alpha radiation. The smaller layer of $> 3 \text{ nm}$ in radius particles during the second flight correlates with the absence of NLC measured by both the lidar and the onboard photometer. The smaller 1 – 2 nm

sized particles measured by channels 3+ and 3- are likely responsible for the measured PMSE.

3.4.2 DOWNLEG DATA: CHANNELS 1± THROUGH 4±

The downleg data from the second MASS flight are shown in Figure 16. The number densities and vertical extent of the charge layers measured on the downleg are smaller than the upleg measurements. The downleg positive ion density measured by MASS channel 1+ is one of the only channels that match the upleg data. The MASS channel 1- on the downleg measured approximately a zero charge density unlike the upleg which measured a small charge layer. The 2- channel measured nearly the same structure on upleg and downleg with slightly lower number densities on the downleg. On the upleg the 3+ channel measured a distinct positive charge layer, while the downleg measurement did not detect a charge layer. For both the upleg and downleg the MASS channel 3+ signal grew exponentially at 87 km as light positive ions leaked into the MASS instrument through the air exit windows. The 3- MASS channel measured a very narrow negative charge layer between 86 and 87 km with a peak density of $\sim 3000 \text{ cm}^{-3}$. Compared to the upleg data the negative charge layer measured by the 3- channel was smaller in vertical extent and in number density. The bottom two channels of the MASS instrument measured two distinct negative charge layers on the downleg, unlike the upleg data with one distinct layer. The first downleg layer between 84 km and 85.5 km resembles a smaller version of the negative charge layer measured on the upleg by channels 4+ and 4-. The second downleg layer between 86.5

and 87 km coincides with the negative charge layer measured on the downleg by the 3-channel.

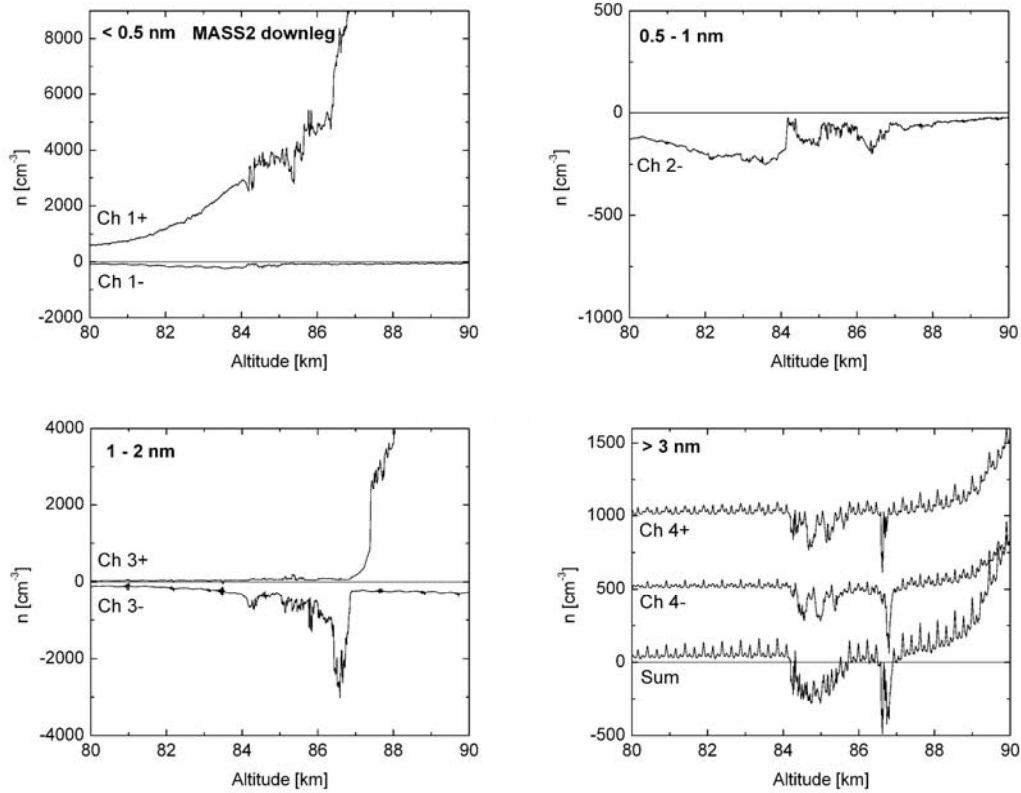


Figure 16. Data from the 8 channels of the MASS instrument for the downleg of the second flight. Channels 4+ and 4- are offset from zero for clarity and their sum is plotted with no offset.

3.5 QUASI-NEUTRALITY CHECK

The MASS instrument detects charged particles from molecular sizes (therefore excluding electrons) to micron sized particles with either polarity of charge. Therefore if all of the MASS channels charged densities are summed with the electron density measured by the Faraday rotation experiment, then the net sum would be zero due to quasi-neutrality condition. The addition of the MASS channels with the Faraday

electron density for both the MASS1 upleg and the MASS2 upleg are shown in Figure 17. This figure includes the total positive charge density, the total negative charge density, and the summed positive and negative charge density. The positive charge density is the addition of the three MASS channels with negative bias. The negative charge density is the addition of the three MASS channels with positive bias, the channels 4+ and 4-, and the Faraday electron density. Figure 17 only displays the upleg signals since the Faraday rotation antennas are inoperable on the downleg.

During the MASS1 upleg the summed charge density is near zero between 83 and 86 km. Below 83 km the summed charge density is positive. The net positive signal could be due to light negative ions being repelled by the payload potential or from a reduced electron density detected by the Faraday rotation antennas due to a high collision frequency. Between 86 and 88 km the summed charge density goes negative, which coincides with the increased negative charge densities detected on channels 3-, 4-, and 4+. Above 88 km the summed charged density turns positive and increases until the signal saturates near 90 km. The positive signal corresponds to the exponential growth of positive density measured by channel 3+, since the ion density tracks the electron density and all of the other MASS channels approach zero. The positive signal is assumed to be the collection of positive ions entering through the air exit windows. Above 88 km the summed charge density quickly diverges from zero due to these positive ions.

During the second MASS flight the summed current was near zero with a small positive signal below 86 km. The positive signal below 86 km may be due to missing

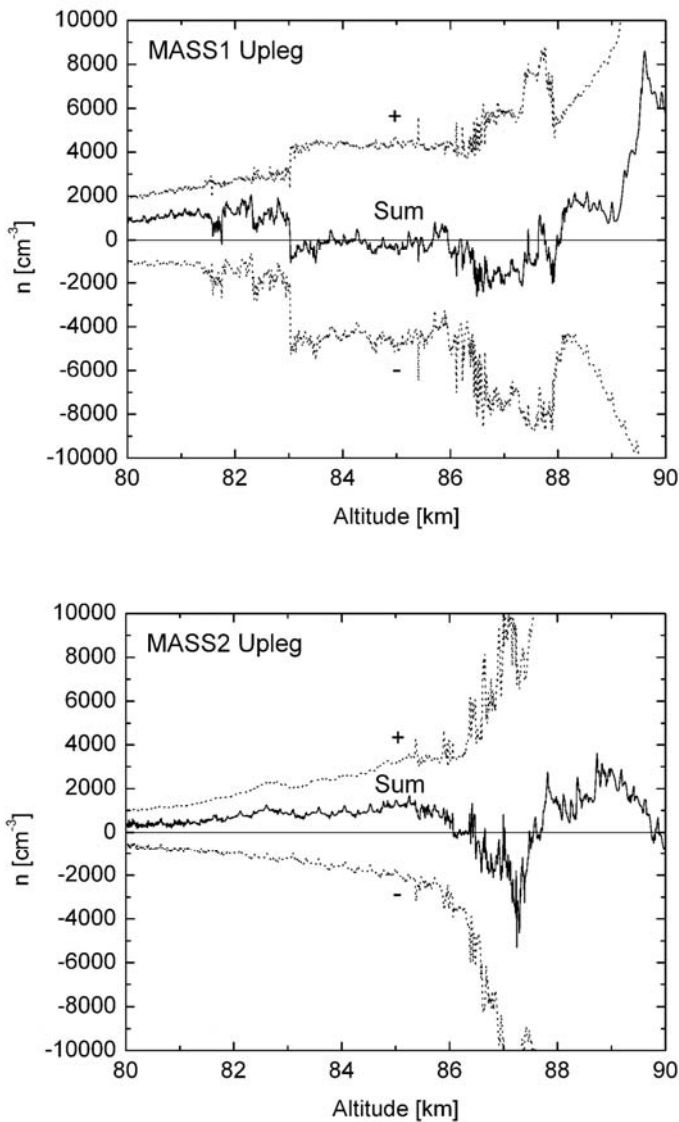


Figure 17. These plots display the upleg of MASS1 and MASS2, the + line is a sum of all positive channels, the - line is a sum of all negative channels, and the Sum line is the sum of all channels. The negative channel includes the electron density measured by the Faraday rotation antennas. A zero sum implies all charges have been collected, which occurred during the MASS1 upleg between 83 and 86 km.

small negatively charged particles repelled by the payload potential or an underestimate of the electron density from the Faraday rotation measurement. Between 86 and 88 km the summed charge density is negative, which may be caused by the missing signal from channel 2+. Above 90 km, the summed charge density again goes positive due to the ions collected through the air exit windows by channel 3+. Overall, the quasi-neutrality condition is met during both flights of the MASS instrument, demonstrating that the MASS instrument is able to collect charged particles of all sizes.

3.6 PHOTOMETER DATA

The analysis of the photometer data was performed by Megner et al. [2009] and will be reviewed below. The photometer measures the scattered irradiance from NLC particles as a function of altitude. From the photometer data, the height and extent of the NLC are determined along with an optically derived number density and an effective mean NLC particle radius. The optical number density and the effective mean particle radius are determined using the scattering phase function, the angular dependence of the scattering signal [Gumbel and Witt, 2001]. Both the optical number density and the effective mean particle radius are strongly weighted by large particles as the scattering intensity from a particle is proportional to its radius to the sixth power in the Rayleigh limit. Furthermore, both the optical size distribution and the effective mean particle radius are sensitive to the assumed particle distribution used in the optical analysis [Rapp and Thomas, 2006]. Two model particle distributions were used

in the optical analysis: a monodispersed distribution of spherical particles and a Gaussian distribution.

During upleg of the MASS1 flight the photometer observed an NLC layer extending from ~81 to ~88 km, which agrees with the ALOMAR RMR lidar measurement, shown previously in Fig. 8. The altitude extent of this NLC is broader than any previously reported in-situ measurement. The observed NLC had three distinct peaks at 82 km, 84 km, and the brightest signal at 86 km. At these altitudes the scattering phase function was determined by comparison to a theoretical phase function modeled using both above particle distributions. For the bottom layer, an effective mean particle radius and particle density was indeterminable due to inhomogeneity of the layer. The top two layers at 84 and 86 km were nearly identical, both being represented by an effective mean particle radius of 50 nm and a density of $\sim 10 \text{ cm}^{-3}$, assuming a monodisperse distribution. Using a Gaussian distribution, the top layers were represented best by a mean particle radius of 30 nm with a distribution width of 14 nm and a particle density of $\sim 30 \text{ particles cm}^{-3}$. The MASS instrument measured densities on the order of 1000 ice particles cm^{-3} , while the photometer particle densities are two orders of magnitude lower. This is due to limited sensitivity of optical measurements to small particles. During the downleg of the MASS1 flight, the photometer saturates from lower atmospheric scattering, as expected and hence is unusable. The MASS2 flight is not discussed as it was flown during a PMSE without NLC.

3.7 COMPARISON TO SOFIE LIMB SCANS

The Solar Occultation for Ice Experiment (SOFIE) is one of three instruments on the AIM (Aeronomy of Ice in the Mesosphere) satellite. The other two instruments are the Cloud Imaging and Particle Size (CIPS) instrument and the Cosmic Dust Experiment (CDE). The CDE instrument measures the size and flux of meteoric dust entering the Earth's atmosphere [Horanyi, 2007]. The CIPS instrument consists of four UV cameras positioned at different angles about the nadir to provide a panoramic picture of NLCs and to determine the size distribution of NLCs [Rusch et al., 2009]. The SOFIE instrument is a limb scanning instrument that measures the atmospheric extinction at 11 wavelengths between 0.33 and 5.01 μm [Gordley et al., 2009]. The SOFIE instrument is able to determine temperatures and abundances of five gaseous species (O_3 , H_2O , CO_2 , CH_4 , and NO). In addition, the SOFIE instrument can determine ice mass density, ice particle shape, effective radius, and parameters for a Gaussian size distribution [Hervig et al., 2009]. The SOFIE instrument vertical resolution is 1.6 km, the horizontal resolution is 4.3 km, the sample volume length along the limb view is 290 km, and hence the total field of view is very large, $\sim 2000 \text{ km}^3$.

The SOFIE data and the MASS data do not occur within a common volume and the NLC and PMSE observed during the two launch dates were highly variable in space and time. Furthermore, the optical measurements made by SOFIE are highly influenced by particles with large radii, while the MASS instrument is more susceptible to particles with smaller radii. However, for completeness the SOFIE data will be shown. The first MASS launch occurred on August 3, 2007 at 22:51:20 UTC (69°N , 16°E), while the two

SOFIE observations closest to the first MASS launch occurred at 20:35 UTC (71.3° N, 30.4° E) and at 22:12 UTC (71.3° N, 6.3° E). The data from these two limb scans are shown in Figure 18, which displays the concentration of water vapor, the concentration of water ice, and the NLC effective radius. The water ice concentration peaked at ~6 ppmv near 85 km and the NLC effective radius varied from 10 nm to 66 nm. Overall,

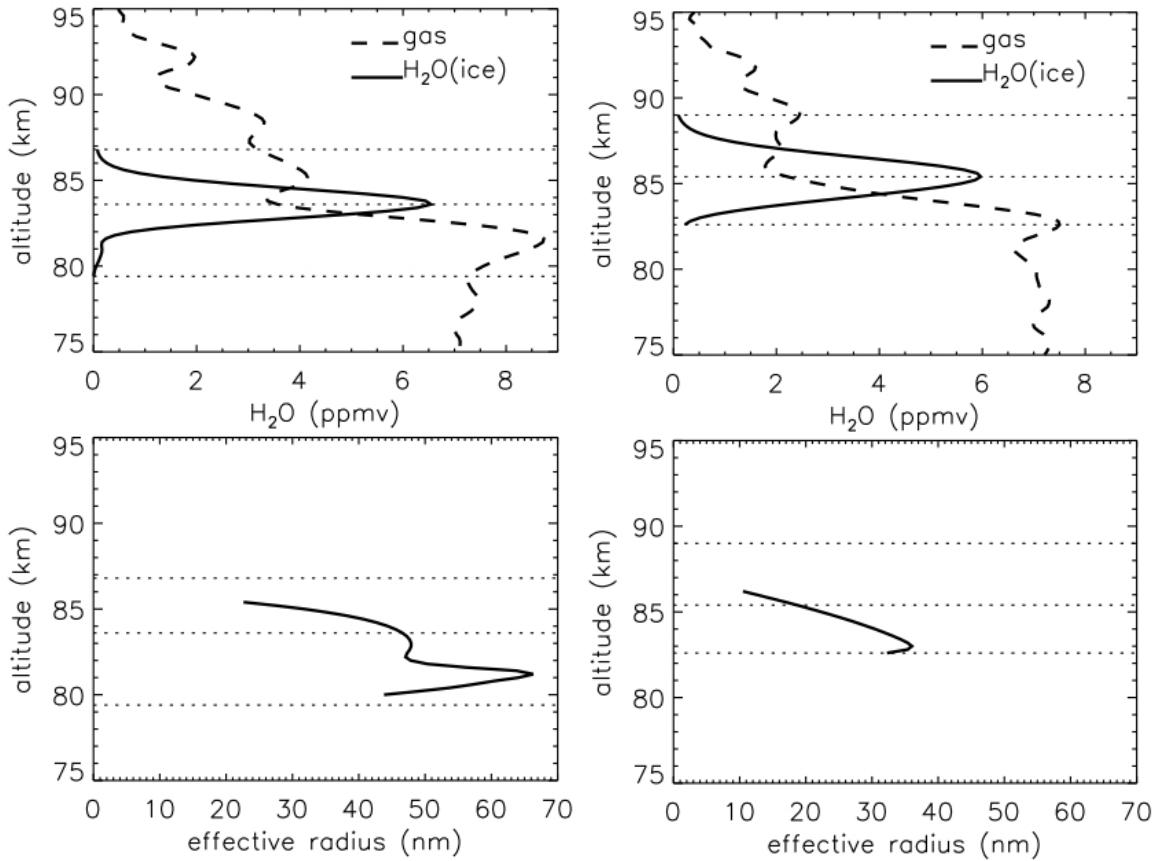


Figure 18. SOFIE observations on August 3, 2007 nearest to the first MASS flight, 20:35 UTC at 71.3 N, 30.4 E (left panel) and at 22:12 UTC at 71.3 N, 6.3 E (right panel). Horizontal dotted lines indicate Z_{top}, Z_{max}, and Z_{bottom} determined from H₂O(ice).

the SOFIE observations during the MASS flight indicate bright NLCs. The second MASS flight occurred on August 6, 2007 at 22:56:00 UTC, while the two closest SOFIE measurements occurred at 21:02 UTC (72.0° N, 22.6° E) and at 22:39 (72.0° N, 358.4° E).

The second MASS launch took place during a PMSE without NLC present, which is confirmed by the SOFIE measurements. The SOFIE data from the second MASS launch is shown in Figure 19. A NLC effective radius was not retrieved due to the poor extinction signal during the second MASS flight, as expected as there was no NLC present. The concentration of water ice was <2 ppmv indicating very tenuous NLCs.

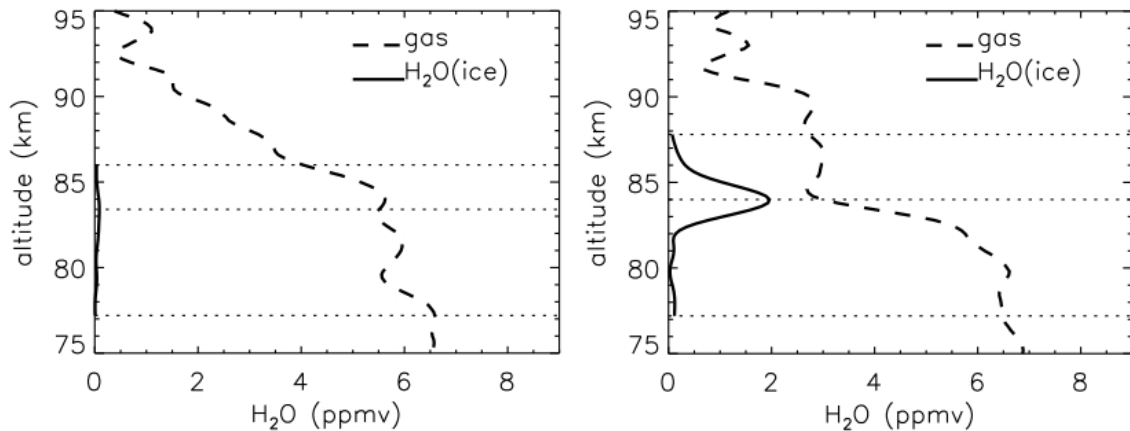


Figure 19. SOFIE observations on August 6, 2007 closes to the second MASS flight: 21:02 UTC at 72.0° N, 22.6° E (left panel) and 22:39 UTC at 72.0° N, 358.4° E (right panel). The horizontal dotted lines indicate Z_{top} , Z_{max} , and Z_{bottom} determined by $H_2O(ice)$.

3.8 MASS FLIGHT PERFORMANCE

Both flights of the MASS instrument successfully returned data between the altitudes of interest. The MASS instrument did experience unexpected noise during the firing of the ACS, identified as microphonic noise. In the design of the instrument the concept of spurious charge generation was a concern, but during the flight no data was consistent with spurious charge generation. The MASS instrument did record small unexpected periodic signals on the bottom channels 4+ and 4-, assumed to be

photoelectric charging within the instrument. These three phenomena: microphonic noise, spurious charge generation, and photoelectric currents are described below.

3.8.1 MICROPHONIC NOISE

During both flights of the MASS instrument unexpected microphonic noise occurred coincident with the firing of the ACS. The amplitude of the noise was most significant on the third pair of collection plates, the plate with the largest bias voltage (± 54 V). When the ACS fires the payload vibrates causing a variation in the capacitance to ground, which results in a current from the time derivative of CV where C is the capacitance and V is the bias voltage. The fact that the collection plate with the largest bias voltage was the most affected by the microphonic noise is consistent with the bias voltage dependence. The microphonic noise was removed from the MASS data using a Gaussian smoothing function. For future flights of the MASS instrument, the ACS should have limited firing during critical data-taking altitudes.

3.8.2 SPURIOUS CHARGE GENERATION

It is possible that the impact of neutral ice particles on collection plates may result in the formation of charged fragments and therefore create false signals in the MASS instrument [Vostrikov et al., 1987; Andersson et al., 1997; Havnes and Næsheim, 2007]. The probability of generating charged fragments from impact should increase with aerosol size and should be dependent upon impact angle. The top three collection plates in MASS are unlikely to produce charged fragments as they collect the smallest particles and are sloped away from the entrance of the instrument. However, the

channels 4+ and 4- collect the largest particles and are directly in the flow. The bottom two plates (channels 4±) measured a large number density of negative aerosols from 83 to 88 km. If neutral particles fragmented on impact of channels 4± and the negatively charged particles were collected on channels 4±, then it is expected that there would be positively charged particles collected elsewhere in the instrument. The collection plate most likely to detect the positively charged fragments from channels 4+ and 4- is channel 3+, which has the largest negative bias of -54 V. During the MASS1 flight, the channels 4+ and 4- recorded a large negative signal from 83 to 86 km in which there is no positive signal detected on the most positively biased collection plate (channel 3+) in MASS. This indicates that spurious charge is not significant within the MASS instrument.

3.8.3 PHOTOELECTRIC CURRENTS

The generation of photoelectric currents from solar ultraviolet light is possible within the MASS instrument. The MASS channels 4+ and 4- showed small spikes (~0.1 nA) periodic with the rocket rotation frequency of 2 Hz, possibly due to photoelectric emission. The periodic spikes on channels 4+ and 4- are 180° out of phase. The other MASS channels do not have signals which indicate photoelectric currents. The photoelectric currents generated on channels 4+ and 4- are small compared to the charged NLC particle signal between 83 and 88 km. Due to the geometry of the MASS instrument and its orientation relative to the sun during flight there is no direct

illumination of any MASS collection surface. The periodic current spikes on channels 4± must be due to scattered light within the MASS instrument.

3.9 MASS DATA DISCUSSION AND CONCLUSIONS

Previously, multiple instruments have been flown into the mesosphere to measure the charged fraction of NLC particles and various other species. Many of these instruments had a single detection channel such that the combined current from both positive and negative particles is collected. Thus a larger negative signal could mask any positive signal or vice versa. For the first time, simultaneous measurements of both positive and negative charge densities in the mesosphere have been made. The MASS instrument allows for the separation of the positive and negatively charged particles, while sorting each polarity into four mass bins. The first MASS flight on August 3, 2007 into a NLC and a PMSE recorded a surprising charge distribution: the smallest particles between 0.5 – 1 nm were positively charged, the medium sized particles between 1 – 2 nm had equal charge densities of positive and negative particles, and the largest particles greater than 3 nm were all negatively charged. This is the first time the mass distribution of NLC particles has been measured. The measured charge particle densities by the MASS instrument can be explained by the nucleation of NLC particles on positively charged particles, which then grow and become negatively charged. The positive condensation nuclei could be positive cluster ions or positively charged meteoric smoke particles. Comparing the MASS1 data to the MASS 2 data shows the difference between charged number densities with and without NLC present. The

observed change in charge number densities is an increase in large ($r > 3$ nm) negatively charged particles. In order to better interpret the MASS data, a complex charge model has been developed. This charge model will be introduced in the following chapter with more discussion on the MASS data in Chapter 5.

CHAPTER 4: CHARGE MODEL

The charging of particles in the mesosphere has major impacts on the formation of PMSE as well as the formation of NLC. As mentioned in Chapter 1, the formation of PMSE is directly related to the attachment of electrons to mesospheric particles, creating steep electron density gradients. The formation of NLC particles requires a condensation nucleus with a radius large enough to support continuous growth; however, if a condensation nucleus is charged, then the minimum radius for continuous growth is reduced. Thus the charging of condensation nuclei is especially important to the formation of NLC. The charge on mesospheric particles has been used to study NLC and PMSE by in-situ charge particle detectors. In addition, these charge particle detectors have measured unexplained positive charge and in the case of the MASS instrument the coexistence of positive and negative layers.

In this work, photodetachment and photoemission rates have been added to a set of kinetic rate equations that determine the charge probability distribution in a steady state. The model uses photo-charging rates corresponding to daytime and twilight conditions and a range of NLC particle densities. The model is solved for three types of materials: MSP, ice particles, and composite particles with ice having grown on a core of MSP. In Section 4.1 we introduce the kinetic rate equation, the attachment rates for electrons and ions, and the model for photoemission and photodetachment. In

Sections 4.2 and 4.3 the solutions to the kinetic charge model are presented and discussed for low and high aerosol densities. In Section 4.4 the model results are summarized.

Megner et al. [2008a and 2008b] and Bardeen et al. [2008] have performed transport model-calculations of meteoric smoke showing that MSP are transported away from the summer mesopause, which has recently been confirmed by the first global observation of meteoric smoke with the SOFIE instrument on the AIM satellite [Hervig et al., 2009]. As a consequence of this transport, the density of MSP with radii sufficiently large to be condensation nuclei appears to be limited. The radius of the MSP must be greater than or equal to a critical value to be a condensation nucleus. This critical radius is dependent upon temperature, water vapor concentration, and the wettability of the material [Keese, 1989]. A critical radius of ~ 1 nm corresponds to a temperature of 130 K, a water volume mixing ratio of 2 ppm, and a perfectly wettable surface. As MSP coagulate and grow in size, they can be transported out of the summer mesopause before reaching the critical radius. The modeled number density of MSP with $r > 1$ nm is approximately 10 cm^{-3} at 85 km in the polar summer mesosphere [Megner et al., 2008a], which is too small to account for NLC observations. Particles below the critical size may be condensation nuclei if they carry charge and the simulations do show a sufficient number of these smaller particles. The predicted number density of MSP for $r < 0.5$ nm is approximately $50,000 \text{ cm}^{-3}$ at 85 km in the polar summer mesosphere [Megner et al., 2008a]. If a small percentage of these particles are

charged, then a sufficient number of condensation nuclei exist to account for the formation of NLC.

The polarity of charge on MSP is important because positive and negative particles have different lifetimes before being neutralized. Charged particles with radii below the critical value will cease to be condensation nuclei if they are neutralized by the collection of an electron or ion. Particles with positive charge are neutralized more rapidly because the mobility of electrons is higher than that of ions. The formation of NLC on positively charged MSP may be negligible because the neutralization time is shorter than the time for growth past the critical radius [Gumbel and Megner, 2009].

In the D-region of the ionosphere, the electron thermal velocity is larger than the ion thermal velocity resulting in aerosol particles charging negatively in the absence of photo-charging. Rapp [2009] compared the rate of photodetachment and photoemission (photoionization) for MSP to the rate of electron attachment and found that MSP are probably charged positively during daytime conditions or may be neutral, depending on the electron number density [Rapp et al., 2010]. Rapp was motivated to include photodetachment and photoionization due to multiple in-situ charged particle detectors measuring small positively charged particles. These observations include the Gerdien condenser [Croskey et al., 2001; Mitchell and Croskey, 2001], the Colorado Dust Detector (CDD) [Smiley et al., 2006], the MASS instrument [Robertson et al., 2009], and a combination of numerical modeling and measurements made by the ECOMA particle detector and several plasma probes on the same sounding rocket [Brattli et al., 2009].

The positive charging of MSP limits the probability of them acting as condensation

nuclei because of the high probability of neutralization, but it helps explain the coexistence of positive and negative particles.

It is known that small ($r < 1$ nm) MSP particles exist in sufficient abundance to be condensation nuclei for NLC, if they are charged as they grow past the critical radius [Megner et al., 2009]. The charging rates for MSP have previously been addressed by Rapp et al. [2009]; however, charge probabilities were only presented for daytime conditions and only for a particle with a radius of 1 nm. In this work, MSP charging during twilight and daytime conditions are compared and the previously modeled size range is expanded. In addition, composite particles consisting of a core of MSP coated in ice are modeled to address the question of how ice growing on a MSP can modify the total particle charging properties. This addresses whether or not MSP remain charged as ice grows on the MSP up to the critical radius. Composite NLC particles may also have implications for the formation of positive charge layers. These positive charge layers have been observed by the MASS instrument coexisting with negative charge layers; however, it is unclear how they form.

4.1 KINETIC CHARGE MODEL

The number density of aerosol particles $N_{r,Z}$ having a charge number Z and radius r is calculated by solving the standard kinetic rate equation [Draine and Sutin, 1987; Jensen and Thomas, 1991; Lübken and Rapp, 2001]:

$$\frac{dN_{r,Z}}{dt} = n_e \alpha_{r,Z+1}^e N_{r,Z+1} - (v_{r,Z}^+ + n_e \alpha_{r,Z}^e) N_{r,Z} + v_{r,Z-1}^+ N_{r,Z-1}, \quad (4.1)$$

where n_e is the electron density, $\alpha_{r,z}^e$ is the rate coefficient for electron collection and $\nu_{r,z}^+$ is the rate of aerosols charging positively. The positive charging rate is the combined rate for ion collection, photodetachment and photoemission given by

$$\nu_{r,z}^+ = n_i \alpha_{r,z}^i + \nu_{r,z}^{emis} + \nu_{r,z}^{det} \quad (4.2)$$

where n_i is the ion density, $\alpha_{r,z}^i$ is the ion attachment coefficient, $\nu_{r,z}^{emis}$ is the rate of photoemission, and $\nu_{r,z}^{det}$ is the rate of photodetachment. The kinetic rate equation is solved by iteration until an equilibrium solution is reached for the charged number density. The equilibrium solution was verified by setting the time derivative to zero and solving the resulting matrix equation.

The charge model is solved assuming quasi-neutrality. The condition for quasi-neutrality is satisfied using either of two methods depending on the number density of aerosols compared to the number density of electrons and ions. The first method, the low density case, assumes the electron and ion densities are constant and equal. This is appropriate when the number of charged aerosol particles is sufficiently small to leave the electron and ion densities unchanged. If the number of aerosol particles in the simulation is on the order of the electron and ion density, then the aerosols can deplete the electron and ion densities requiring the aerosol charge to be included in the quasi-neutrality condition. The second method for satisfying quasi-neutrality, the high density case, implies the electron and ion density differential equations 4.3 and 4.4 are solved simultaneously with the aerosol kinetic equation

$$\frac{dn_e}{dt} = Q - \alpha_{ie} n_i n_e - \sum_Z \sum_r (n_e \alpha_{r,Z}^e - v_{r,Z}^{emis} - v_{r,Z}^{det}) N_{r,Z} \quad (4.3)$$

$$\frac{dn_i}{dt} = Q - \alpha_{ie} n_i n_e - \sum_Z \sum_r n_i \alpha_{r,Z}^i N_{r,Z} \quad (4.4)$$

where Q is the electron ion pair production rate, and α_{ie} is the recombination rate for ions and electrons. This equation allows the electron and ion densities to be reduced as they attach to the aerosol particles. In our model the electron-ion pair production rate is $10 \text{ cm}^{-3}\text{s}^{-1}$ and the electron ion recombination rate is $10^{-6} \text{ cm}^3\text{s}^{-1}$. These values are for an altitude of 87 km during the daytime with a mixture of water cluster ions and molecular ions [Leu et al., 1973; Jensen and Thomas, 1991]. The equilibrium electron and ion density is 3162 cm^{-3} , calculated using the above electron ion pair production and recombination rate neglecting photo-charging and electron ion attachment to aerosols.

In the kinetic charge model, spherical particles with radius from 1 to 100 nm in increments of 1 nm are used. The lower limit of 1 nm in radius is used as suggested by Rapp [2009] due to large uncertainty in the applicability of the electron and ion charging rates as well as the photo-charging rates for particles approaching molecular size. The low density case of aerosols is modeled using a number density of 1 cm^{-3} . The high density case of NLC particles is modeled using a monomodal distribution with a number density corresponding to a water vapor concentration of 5 ppm. Monomodal distributions were modeled using 100 different radii from 1 to 100 nm, corresponding to a range in number density from $\sim 10^7$ to $\sim 10 \text{ cm}^{-3}$. The number density of ice particles, $n(r)$ having a given radius is calculated from:

$$n(r) = \frac{n_{H_2O}}{N_{H_2O}(r)} = \frac{5 \text{ ppm} \cdot n_{air} \cdot m_{H_2O}}{4/3 \pi r^3 \rho}, \quad (4.5)$$

where n_{H_2O} is the density of water molecules in the mesosphere at an altitude of 85 km, $N_{H_2O}(r)$ is the number of water molecules in an ice aerosol with a given radius r , n_{air} is the number density of air molecules at 85 km, m_{H_2O} is the molecular mass of water, and ρ is the mass density of ice ($\rho = 0.93 \text{ g/cm}^3$).

Once the charge number density of aerosols is found, the charge probability distribution, and the average charge number are calculated. The charge probability distribution $P_{r,Z}$ is calculated by dividing the charge number density by the total particle number density N_{total} :

$$P_{r,Z} = N_{r,Z} / N_{total}. \quad (4.6)$$

Similarly, the average charge number is calculated by multiplying the charge number by the charge number density and dividing by the total particle number density.

$$\langle Z \rangle = \sum_Z Z \cdot N_{r,Z} / N_{total} \quad (4.7)$$

4.1.1 ELECTRON AND ION ATTACHMENT COEFFICIENTS

The electron and ion attachment coefficients are derived using the Coulomb interaction, the image force, and basic gas kinetics (Natanson, 1960). For an overview of electron and ion attachment coefficients the reader is referred to the original derivation by Natanson (1960) and a more recent review by Rapp (2000). The electron attachment

coefficient is separated into three cases depending on if the aerosol particle is initially neutral, negatively charged, or positively charged:

$$\alpha_{r,Z=0}^e = \pi r^2 c_e \left[1 + \sqrt{\frac{e^2}{8\varepsilon_0 k_B T r}} \right], \quad (4.8)$$

$$\alpha_{r,Z<0}^e = \pi r^2 c_e g^2 \text{Exp} \left[\frac{-|Z|e^2}{4\pi\varepsilon_0 k_B T r} \cdot \left(1 - \frac{1}{2g(g^2 - 1)Z} \right) \right], \quad (4.9)$$

$$\alpha_{r,Z>0}^e = \pi r^2 c_e \left[1 + \frac{|Z|e^2}{4\pi\varepsilon_0 k_B T r} \right], \quad (4.10)$$

where T is the temperature, c_e is the electron thermal velocity of the plasma, e is the electron charge, ε_0 is the permittivity of free space, and k_B is Boltzmann's constant. The electron thermal velocity is defined as $c_e = \sqrt{8k_B T / \pi m_e}$, where m_e is the mass of the electron. Natanson's coefficient is also dependent upon a dimensionless factor g , which is defined by the distance where the force changes sign between repulsion (Coulomb) and attraction (image force), given by Equation 4.11:

$$Z = \frac{2g^2 - 1}{g(g^2 - 1)} \quad (4.11)$$

The ion attachment rate coefficient is given by expressions analogous to the electron rate coefficient where the electron mass is replaced with the ion mass in the thermal velocity. The ion mass used in our model is 50 amu corresponding to an average ion species dominated by water cluster ions. The above calculation for electron and ion attachment is independent of material. That is ice particles, MSP and composite particles of the same radius all have the same attachment rates.

4.1.2 PHOTODETACHMENT AND PHOTOEMISSION RATES

Previous charge models have omitted photoemission for pure ice particles as the work function is very large, making the photoemission rate for ice completely negligible [Jensen and Thomas, 1991]. The workfunction of ice can be reduced due to a fresh contamination by atomic sodium due to a large meteoroid influx; however this event occurs rarely [Vondrak et al., 2006]. Photoemission can play a role in mesospheric charging for materials with lower workfunctions than ice, such as hematite.

Photodetachment is the removal of an electron from a negatively charged particle by photon absorption. Even at large solar zenith angles (SZA), photodetachment has a large effect upon the charge state of mesospheric particles as both ice and hematite have low electron affinities. In our charging model, three types of particles are included: MSP, NLC ice particles, and MSP covered in layers of ice. Photo-charging of MSP is modeled using hematite (Fe_2O_3), which is a likely candidate for meteoritic smoke [Plane, 2003; Rapp, 2009]. The NLC particles are modeled in two ways: pure ice particles and as hematite cores covered in ice for both the low density and high density cases.

The photoemission and photodetachment rates are calculated using [Rapp, 2009]:

$$v_{r,Z}^{photon} = \int_0^{\lambda_0} F(\lambda) \cdot \sigma(r, n, \lambda) \cdot Y \cdot d\lambda \quad (4.12)$$

where $F(\lambda)$ is the solar flux of photons as a function of wavelength, $\sigma(r, n, \lambda)$ is the Mie absorption cross-section as a function of radius r , complex index of refraction n , and wavelength λ , Y is the quantum yield, and the integral is bounded by a cutoff

wavelength λ_0 determined by the workfunction W or electron affinity EA of the bulk material. The electron affinity is the minimum amount of energy needed to remove an electron from a bulk material with a charge number $Z \leq -1$. Equation 4.12 assumes that photodetachment (photoemission) occurs when a single photon is absorbed by a particle, if the photon has energy greater than the electron affinity (workfunction) an electron has a probability of being detached (emitted), where the probability is given by the quantum yield. The absorption of a photon in Equation 4.12 is based on the Mie absorption cross-section, which is dependent upon the material's index of refraction. In the above calculation, an index of refraction for a bulk material has been used, rather than one for nanometer sized particles due to a lack of laboratory measurements on nanometer sized particles. As particles approach molecular sizes their absorption properties become quantum mechanical and standard theories do not apply. By limiting our calculation to particles greater than or equal to 1 nm in radius, it is assumed that the bulk index of refraction can appropriately describe the absorption properties. The electron affinity for hematite is 2.0 eV and is 0.8 eV for ice. The workfunction for hematite is 5.5 eV and is 8.7 eV for ice [Baron et al., 1978; Wang et al., 1996; do Couto et al., 2006]. The assumed quantum yields for hematite and ice are 1 and 0.01 respectively [Baron et al., 1978; Rapp et al., 2007]. The high quantum yield of 1 for hematite is used to derive maximum estimates for photoemission and photodetachment rates. The complex index of refraction for ice is taken from Warren [1984] and the complex index of refraction for hematite is taken from the internet data base of the

Astrophysical Laboratory of the University of Jena, Germany (see <http://www.astro.unijena.de/Laboratory/OCDB/oxsul.html>).

The solar flux used in these calculations is at 85 km with a SZA of 0° or 93° so that daytime and twilight conditions are modeled. Many rocket campaigns occur during twilight conditions, e.g. MASS, ECOMA, and DROPPS [Goldberg et al., 2001; Rapp et al., 2009; Robertson et al., 2009]. The solar spectrum is taken from the World Meteorological Organization [WMO, 1985] and the solar flux simulation used is based on the parameterization used in the NRL CHEM2D model [Summers et al., 1997].

The Mie absorption cross-section is calculated using two separate routines adapted from Bohren and Huffman [1983]. The first is a standard Mie scattering routine of a plane wave scattering from a spherical object that has a complex index of refraction. The second routine calculates a plane wave scattering from a composite spherical object with a spherical core that has a complex index of refraction and a coating with a given thickness and a different index of refraction. The first routine is used to calculate the Mie cross-section for a sphere of pure hematite or ice, while the second routine is used to calculate the cross-section for hematite cores coated with increasing layers of ice.

Four absorption cross-sections are shown in Figure 20: a hematite sphere with $r = 1$ nm, an ice sphere with $r = 2$ nm, and two composite particles with 1 nm hematite cores layered with 1 nm of ice and 99 nm of ice. A transition might be expected for the composite particle as the ice becomes larger and masks the hematite core. However, as shown in Figure 20, there is no transition. Both of the materials contribute to the cross-section independent of coating thickness. As the electric and magnetic fields must

satisfy boundary conditions at each interface between differing indices of refraction, the hematite core always affects the scattered fields. As a result, the composite particle's cross-section is increased relative to a pure ice particle for wavelengths greater than 170 nm. This increase in the absorption cross-section causes an increase in the photodetachment and photoemission rate for a hematite core coated with ice.

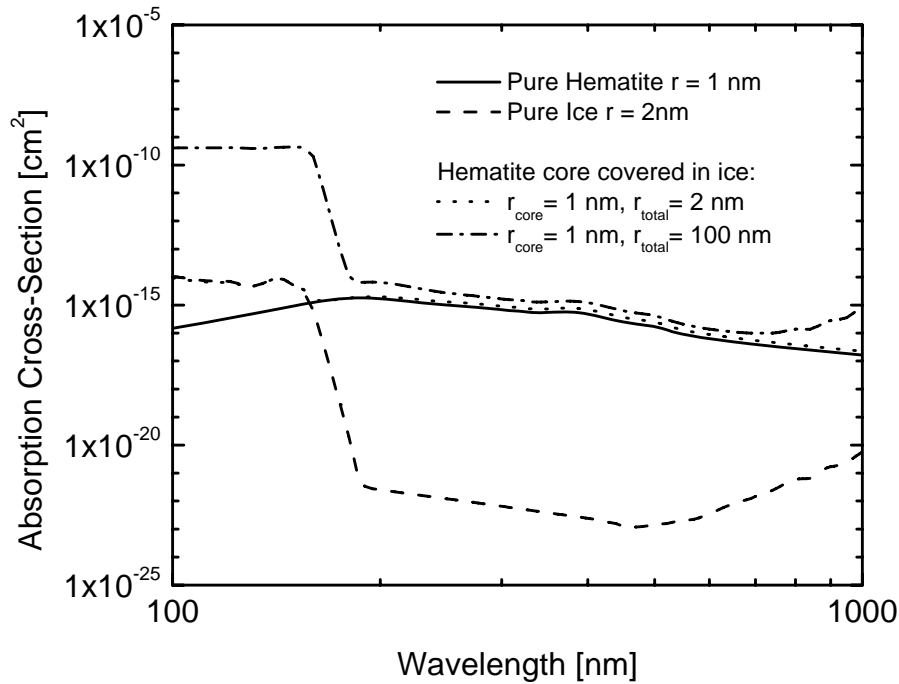


Figure 20. A plot of the Mie absorption cross-section as a function of wavelength for four types of spherical particles: a 1 nm in radius particle of hematite, a 2 nm in radius particle of ice, and a 1 nm in radius composite particle with a core of hematite covered in 1 nm of ice and 99 nm of ice for total radii of 2 nm and 100 nm. The plot shows that the hematite core increases the absorption cross-section for a composite NLC particle thus increasing photoemission and photodetachment rates.

In calculating the rates of photodetachment or photoemission for a composite particle three variables in the rate equation are uncertain: the electron affinity, the workfunction, and the quantum yield. The uncertainty in the above quantities is due to a lack of experimental data and a lack of a theoretical basis for describing the emission

of an electron from a composite particle. As the absorption cross-section is increased by the hematite core, it is more likely that the core will absorb a photon than the ice mantle and thus emit an electron. The probability that the electron passes through the ice mantle and is emitted from the particle is unknown. In order to address this uncertainty, three different models for the electron affinity, the workfunction, and the quantum yield were used in calculating the photodetachment and emission rates for composite particles. The first two models use the values for hematite (hematite: $EA = 2.0$ eV, $W = 5.5$ eV and $Y = 1$) or for ice (Ice: $EA = 0.8$ eV, $W = 8.7$ eV and $Y = 0.01$). The third model uses a volume averaged value for all three of these quantities. The volume averaged condition is based upon Rapp et al. [2009], in which the photoelectric current is linearly proportional to the volume density of the aerosol particle.

4.2 LOW AEROSOL DENSITY RESULTS

The results from the kinetic charge model for the low aerosol density case are shown and discussed in the next three sections: ice, MSP, and composite particles.

4.2.1 ICE PARTICLES

The ice model was run with and without photo-charging. Figure 21 shows the average charge number on the ice particle as a function of radius for both models. The photodetachment calculation was done using both daytime and twilight conditions. For ice without photo-charging, the average charge number is constant at -1 for $r < 10$ nm and it grows more negative approximately linearly with the aerosol radius for $r > 10$ nm.

nm. This is in agreement with previous charge models [Jensen and Thomas, 1991]. For photo-charging Figure 21 shows the reduction in the average number of attached electrons for the largest ice particles ($r > 20$ nm) for both conditions due to photodetachment. The reduced electron attachment is also apparent by comparing Figures 22A and 22B, which show the charge probability distribution for several ice

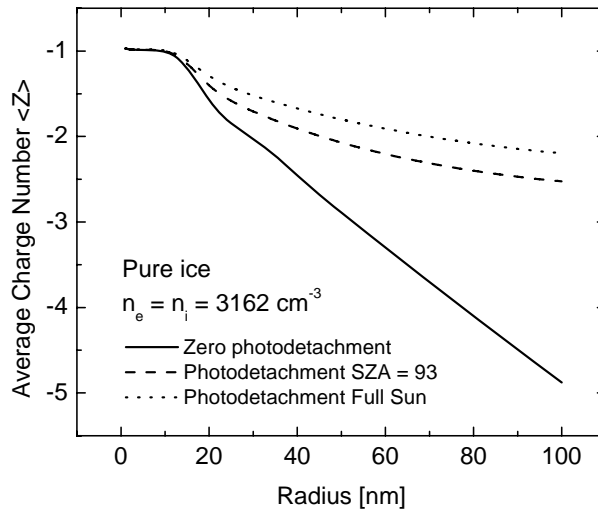


Figure 21. The average charge number on an ice particle as a function of radius for three different conditions: no photodetachment, photodetachment with a SZA of 93° , and photodetachment with a SZA of 0° . The average charge becomes less negative with increasing photoemission.

particle radii without photo-charging and with twilight photo-charging. The daytime condition is not shown since the two charge probability distributions with photodetachment are nearly identical. For the twilight condition, photodetachment competes with electron attachment limiting how negatively charged large ice particles can become. The twilight rates for photodetachment are reduced compared to the daytime rate, but they are still significant. For both photodetachment conditions NLC particles of pure ice still charge negatively.

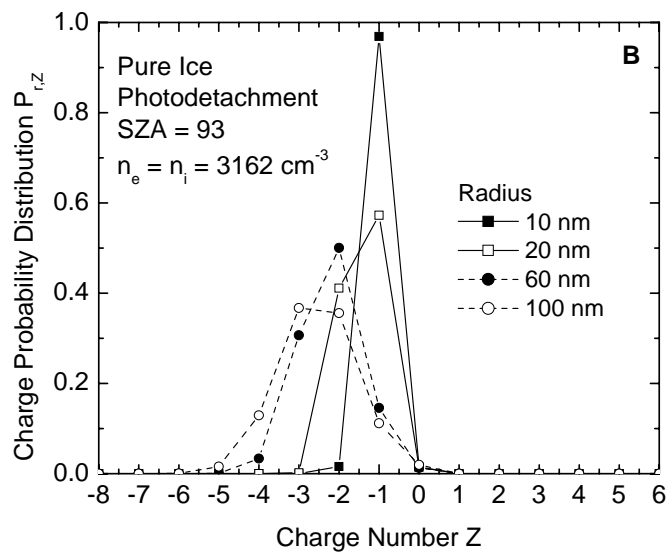
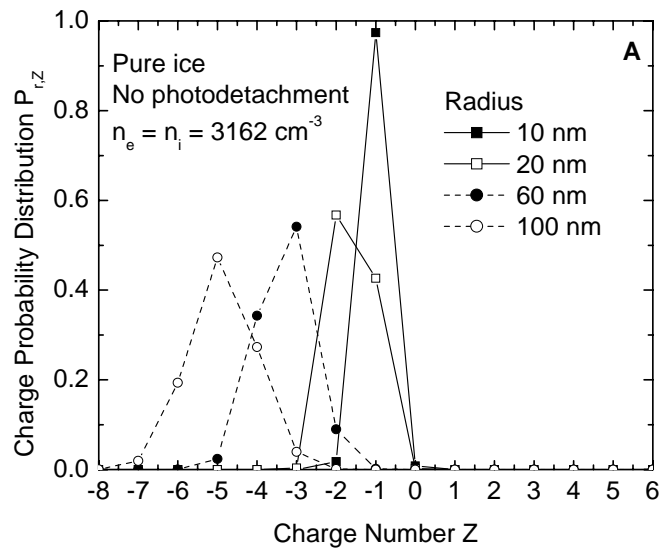


Figure 22. (A) the charge probability distribution for an ice particle with no photodetachment for several different radii is shown. The electron and ion density is 3162 cm^{-3} . (B) shows the charge probability distribution for an ice aerosol particle for several different radii. Photodetachment is included for a SZA of 93° . For both cases, the number density of ice particles is assumed much smaller than the electron and ion density of 3162 cm^{-3} .

4.2.2 METEORIC SMOKE PARTICLES

The low density results for photo-charging of MSP are shown in Figure 23 for a SZA of 93° . These results are nearly identical to the results for a SZA of 0° , which are not shown. A 1 nm radius MSP has a 91% probability of being neutral and a 9% probability of charging positive; while a 10 nm radius MSP has a 14% probability of being neutral and an 86% probability of charging positive. MSP charge more positive with increasing radius due to increased photo-charging. The low density results indicate that during daytime and twilight conditions the majority of MSP will be neutral, a small fraction will be positively charged, and a negligible fraction will be negatively charged. Note that these results are specific to a large electron and ion density of 3162 cm^{-3} . The electron and ion density in the mesosphere varies depending on the electron and ion pair production rate and their recombination rate, which can vary by orders of magnitude [Lübken and Rapp, 2001].

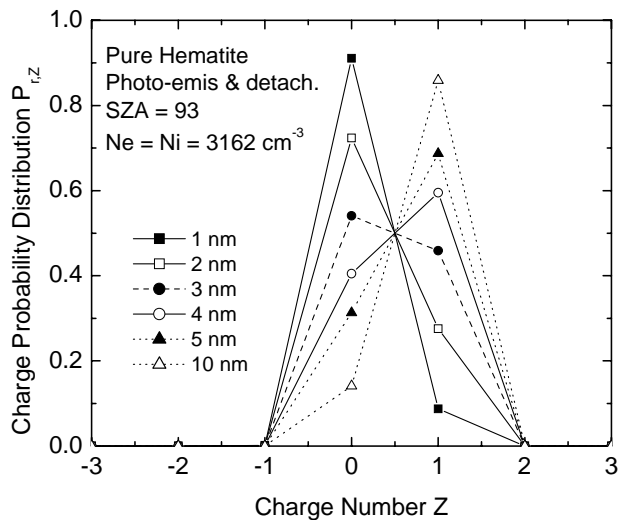


Figure 23. The charge probability distribution for hematite particles of several different radii including photoemission and photodetachment rates with a SZA of 93° . If the SZA is 0° , the charge probability is nearly unchanged.

The charging of MSP has major implications for the formation of NLC on MSP as well as the coexistence of positive and negative particles in the mesosphere. The polarity of charge on MSP also plays an important role in the growth of NLC. The above low density charge model of MSP including photo-charging implies that MSP are positively charged and hence are poor condensation nuclei for NLC. This implication has limited impact as a larger number density ($\sim 50,000 \text{ cm}^{-3}$) of MSP with radii below 1 nm needs to be modeled. Both the number of particles and the size can have significant effects on the charge state of small MSP.

4.2.3 COMPOSITE PARTICLES

The charging of composite NLC particles including photo-charging was studied using both SZAs and using three different models for the electron affinity, workfunction, and the quantum yield. These models are called ice, hematite, and volume averaged as discussed in section 4.1.2. The charge probability distributions using the hematite and volume averaged models are shown in Figure 24. The ice model and the volume averaged model gave similar results and all of the models had minor dependence upon SZA. All three photo-charging models for composite NLC particles show that the particles are predominantly neutral for $r < 10 \text{ nm}$ and negative for greater r . Only the hematite model, which has the greatest photo-charging rates, leads to a very small fraction (3%) of the 2 nm in radius composite particles charging positively. For the hematite model, the enhanced photo-charging leads to a diminished negative

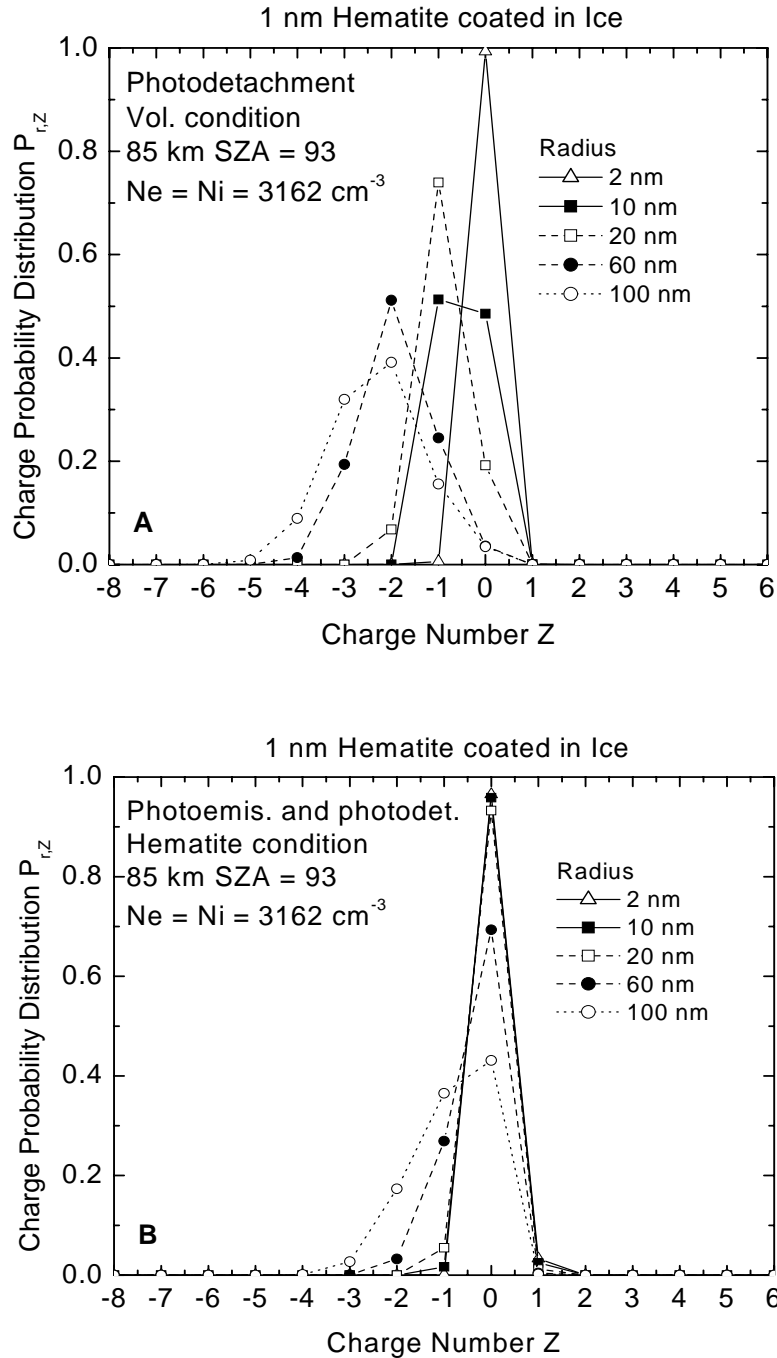


Figure 24. Two plots of the charge probability for a 1 nm radius hematite particle coated in layers of ice with an outer radius of 2, 10, 20, 60, 100 nm. In (A) the charge probability is calculated using the volume averaged model for the photodetachment rate and with a SZA of 93°. In (B) the charge probability is calculated using the hematite model for the photodetachment rate.

charge probability distribution for the largest particles, especially compared to the volume averaged and ice models.

A comparison of the composite particle models to the previous pure ice model with photodetachment shows how the core of hematite further increases the rate of photodetachment for NLC particles. The increased photo-charging results in a more neutral charge probability distribution for $r < 10$ nm and limits how negatively charged particles are for $r > 10$ nm. For example, the pure ice model with photodetachment has a 97% probability of having a charge number $Z = -1$ for an $r = 10$ nm pure ice NLC particle. For $r = 10$ nm, a composite NLC particle with the volume average model for photodetachment has a 51% probability of having a charge number $Z = -1$ and with the hematite model for photodetachment it has a 2% probability of having a charge number $Z = -1$. All three modeled composite particles had an increased photodetachment rate due to the hematite core, which further diminished the attachment of electrons to the NLC particles.

Due to the lack of experimental data on small particle charging as well as the uncertainty in the theoretical charging rates [Rapp, 2009]; we chose to limit our modeled radii for composite particles from 2 nm to 100 nm. The smallest composite particles in our model being neutral suggests that smaller composite particles will also be neutral. If neutrality holds for composite particles with $r < 1$ nm (i.e. the critical radius), then NLC will not nucleate on these particles. Experimental data on photo-charging of small particles is needed to confirm the possibility of NLC nucleating on meteoric smoke particles.

4.3 HIGH AEROSOL DENSITY RESULTS

If the number density of NLC particles has grown large enough to significantly deplete either the electron or the ion density via attachment, then the electron and ion densities can no longer be considered constant and equations for their evolution must be included in the kinetic rate equations. Rocket-borne instruments have shown that electron and ion bite-outs can occur during the formation of NLC when the aerosol particle density is not small in comparison with the electron and ion densities.

The high aerosol density results from two cases will be presented. Both models have NLC particles with 5 ppm number densities and equations 4.3 and 4.4 are used for the electron and ion densities with initial values of 3162 cm^{-3} . The number density of ice particles for 1, 5, and 10 ppm water vapor concentrations are shown in Figure 25. The

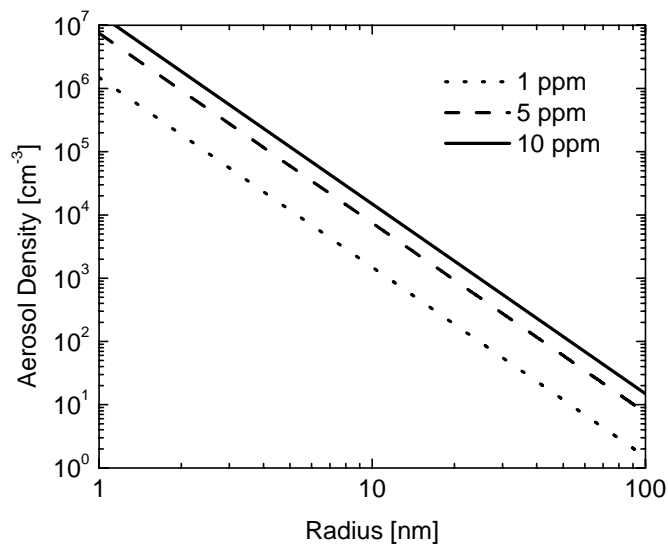


Figure 25. Plot of the number density of ice particles as a function of radius assuming a monomodal distribution for three water vapor mixing ratios: 1, 5, and 10 ppm.

first high density aerosol case is for pure ice NLC particles neglecting photodetachment. The second case is for composite NLC particles with a core of hematite coated in ice. The photo-charging is calculated using the volume averaged model for photoemission and photodetachment at a SZA of 93° for the composite particle.

4.3.1 PURE ICE PARTICLES

The charge probability distribution and charge number densities for the first case are shown in Figure 26A and 26B. Only a small fraction of the $r = 1$ nm pure ice particles becomes positively or negatively charged as seen in the charge probability distribution. However, due to the large number density of NLC particles this small percentage equates to the coexistence of positive and negatively charged pure ice particles with large densities of ~ 3000 cm^{-3} . These large number densities of charged NLC particles correspond to a complete electron and ion bite-out, as seen in Figure 26B. In this high density model, electron and ion bite-outs and a large population of positive and negative particles coexist for $r < 10$ nm NLC particles. A large number density of small NLC particles is another possible explanation for the coexistence of positive and negative densities of aerosols in the mesosphere. Initially electrons attach to the small ice particles reducing the electron density. With the reduced electron density the recombination of ions with electrons is decreased, enhancing the ion density. The increased ion density leads to the attachment of ions to NLC particles, which eventually reduces the density of ions. With both electron and ion densities reduced, the recombination rate of electrons with positively charged NLC and ions with negatively

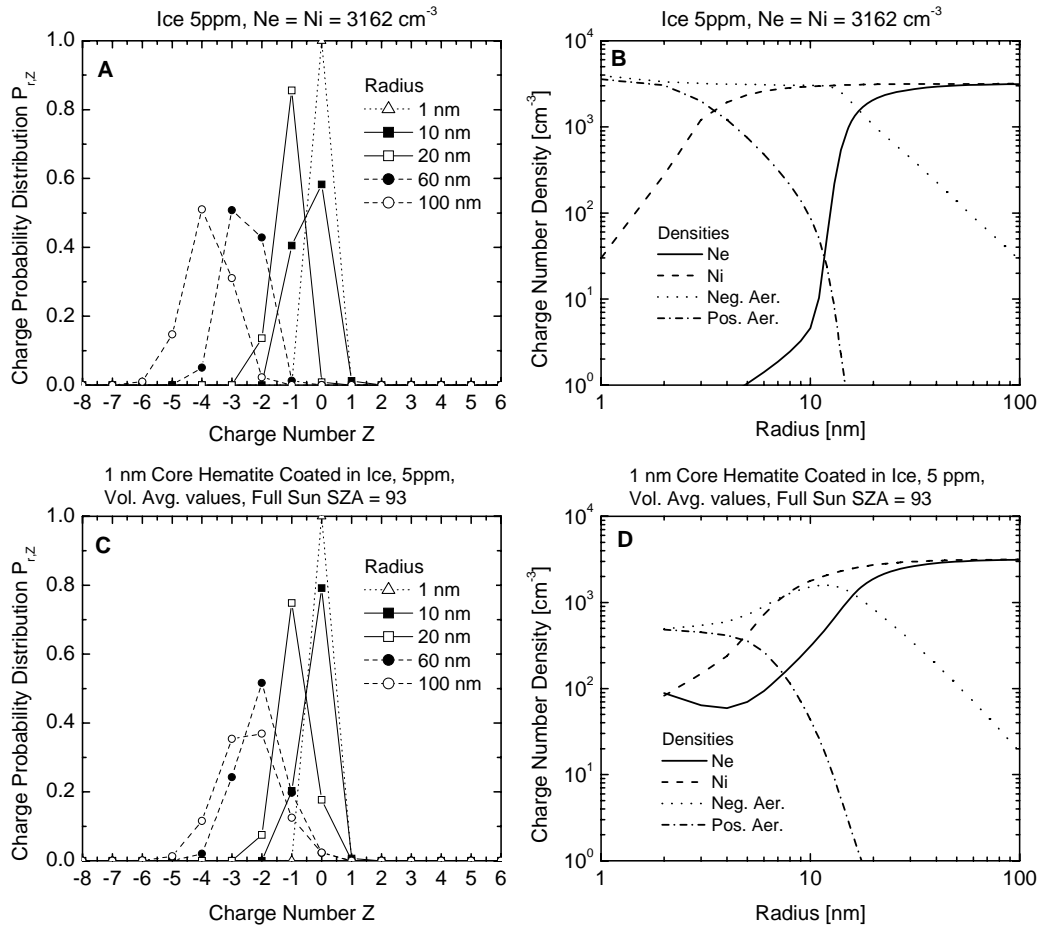


Figure 26. Model result for the high number density model of ice particles with 5 ppm water vapor. Plots A and B show the charge probability distribution and charge number densities for pure ice particles. Plots C and D show the charge probability distribution and charge number densities for composite particles using the volume averaged model for photo-charging. Plots B and D display the number densities a function of particle radius for the electrons, the ions, the positive NLC particles, and the negative NLC particles.

charged NLC are diminished. The end result is the coexistence of positive and negatively charged small, $r < 10$ nm, NLC particles. In the solutions for larger ice particles, $r > 10$ nm, whose average charge is negative, there is no bite-out in the electron or ion density as the number density of large ice particles is limited by the availability of water to a value well below the electron and ion densities. This

demonstrates the limitation of large NLC particles from creating electron and ion bite-outs. It must be noted that the formation of bite-outs is heavily dependent upon multiple variables, such as the number density of aerosols, the recombination rate, and the electron ion pair production rate [Lübken and Rapp, 2001].

Pure ice particles including photodetachment were also modeled and the results were nearly identical to pure ice particles without photodetachment. Since the inclusion of photodetachment is negligible for particles below 10 nm in radius, the number densities of ice particles below 10 nm is nearly identical for both pure ice with and without photodetachment. The charged number densities for the two models for particles above 10 nm are also nearly identical. This is due to the low number densities of ice particles, which limits their ability to deplete the electron and ion densities.

4.3.2 COMPOSITE PARTICLES

The composite NLC particles are modeled with volume averaged photodetachment and photoemission rates. The composite particles consist of a 1 nm in radius hematite core coated in layers of ice, ranging in total radius from 2 to 100 nm. Figure 26C shows a calculation of the charge probability distribution as a function of particle radius. The distribution is similar to the low density case. Figure 26D shows the number densities of electrons, ions, positively charged NLC, and negatively charged NLC for different radii. Although the results show a complete electron and ion bite-out does not occur, the electron and ion densities are significantly reduced. Also, a

population of positive and negative NLC particles coexist, but not with large enough densities to account for the large reduction in the electron and ion densities.

The model shows that the inclusion of the hematite core raises the photodetachment rate to the point where it competes with the attachment of electrons, thus making the charge probability distributions more neutral. Although the attachment of electrons is reduced, due to the high number density of NLC particles a small fraction of electrons are still able to attach. The attachment of electrons lowers the electron density, makes a small population of negatively charged NLC, and makes ion attachment possible. The positive NLC particles recombine with electrons quickly due to the large remaining electron density. The recombination rate of electrons and ions is increased by the presence of NLC particles, reducing both of their densities. Eventually, the system reaches equilibrium as the recombination rate decreases due to the decreasing electron and ion density. As the recombination rate decreases, the lifetime of positive NLC particles increases resulting in a small population of positive particles alongside the previous negative NLC population. The reductions in the electron and ion densities are the result of electron and ion attachment to NLC and are due to the increased recombination of electrons with positively charged NLC.

Composite particles with the ice model for photo-charging are not shown since they are nearly identical to the volume averaged model. The hematite model for photo-charging of composite particles was also modeled in the high density limit and found to be unphysical due to the large resulting electron density. The increase in photoemission for the hematite model increased the electron density to over $10,000 \text{ cm}^{-3}$, which is not

seen at an altitude of 85 km. The photo-charging rate from NLC particles must not be large enough to create an over abundance of electrons.

4.4 CONCLUSION AND DISCUSSION

Multiple charging distribution results have been presented on the charging of MSP, pure ice NLC particles and composite NLC particles including photodetachment and photoemission rates. The kinetic charge model consisted of a low aerosol density model and a high aerosol density model. The low density model showed that photodetachment is significant for pure ice particles with $r > 10$ nm in radius for twilight and daytime conditions, a new result. Fewer electrons were able to attach to pure ice NLC particles due to photodetachment. For the first time, the charging of a composite NLC particle has been considered. The addition of a hematite core in an ice NLC particle in the low density model leads to an increased Mie absorption cross-section, which increases photo-charging rates compared to pure ice NLC particles. The increased rate of photo-charging affected all sizes of NLC particles and neutralized small composite NLC particles with $r = 2$ nm. The neutralization of small composite particles and the results for charging of MSP may have significant implications for the formation of NLC on meteoric smoke particles.

Previously, MSP photo-charging rates for daytime and nighttime conditions have been compared to electron and ion attachment rates and a charge distribution was calculated for an $r = 1$ nm MSP [Rapp, 2009]. In our MSP model, we studied MSP ranging in radius from 1 nm to 100 nm and we included photo-charging rates at

twilight conditions. The low density model showed that MSP become neutralized as their radius is decreased and that only a small percentage (9%) of $r = 1$ nm MSP are charged positively. MSP below the modeled value of $r = 1$ nm would likely have an even smaller percentage of particles charging positively. Particles must be charged in order to grow to the critical radius and to be considered condensation nuclei for NLC particles [Gumbel and Megner, 2009]. The majority of small ($r < 1$ nm) MSP are neutral and the composite particle model shows that particles below the critical radius are likely to be neutralized as well. This implies that MSP are poor condensation nuclei due to their limited ability to charge and to remain charged as ice grows on them. However, more experimental data are needed to confirm the charging properties of MSP, NLC particles, and composite particles, especially at molecular scales. In-situ observations at various SZA outside of the NLC season will also help verify charge models and laboratory experiments for MSP. Suggested instruments for these observations include the MASS instrument, which have measured positive charge layers in the past. The most important information required to improve our understanding of MSP charging is knowledge of their composition. Once the composition of MSP is known, then laboratory studies can focus on measuring photo-charging rate as well as electron and ion attachment rates.

The high density model focused on the charging of NLC particles modeled by pure ice particles and on the charging of composite particles with volume averaged photo-charging rates. This is the first time that photodetachment rates have been included in a high density charge model. These simulations demonstrate the

coexistence of positive and negatively charged particles can be due to large number densities of NLC aerosols. Photo-charging can limit the formation of electron and ion bite-outs, but in both high density NLC models positive and negatively charged NLC particles coexist. This high density result may explain observations by rocket-borne instruments of the simultaneous occurrence of small positive and negative NLC particles measured by the MASS instrument. If the consequence of having a large number density of aerosols is to have a population of both positive and negative particles, then this high density result may play a role in the charging of small MSP. Hence, the charging of $r < 1$ nm meteoric smoke particles with high number densities may greatly affect the formation of NLC.

CHAPTER 5: CONCLUSION AND DISCUSSION

The MASS instrument is a rocket-borne electrostatic mass spectrometer designed to measure the charge density of aerosols in the mesosphere. The instrument was calibrated using a RF ion beam and a series of numerical simulations. The calibration results quantified the effect of aerodynamics on the collection efficiency of charged particles. The MASS instrument was able to overcome previous charged particle detector difficulties such as having a minimum radius for detection of 2 nm for charged particles. The MASS instrument was flown on two sounding rockets in the NLC Summer season of 2007 and it successfully returned data on both the upleg and the downleg of both flights. The MASS data is the first in which both negative and positive charge densities were measured in coexistence simultaneously. In addition, the MASS instrument collected each polarity in four coarse mass bins: < 0.5 nm, $0.5 - 1$ nm, $1 - 2$ nm, and > 3 nm in radius. The first MASS flight into a NLC and a PMSE measured a layer of small positively charged particles with radii between $0.5 - 1$ nm, a positive and negative charge layer with radii between $1 - 2$ nm, and a very broad negative charge layer with particles > 3 nm.

Two possible explanations exist to account for the charge transition from small positively charged particles to large negatively charged particles measured by the MASS instrument. The first scenario is the NLC particles grow on positively charged

condensation nuclei and as the NLC grow larger they collect more electrons and charge negatively. In this scenario, the most likely condensation nuclei are water cluster ions or positively charged MSP. From the discussion on NLC nucleation in Chapter 1, water cluster ions have not been observed to grow large enough to be condensation nuclei [Gumbel et al., 2003] and their growth is limited by dissociative electron recombination [Rapp and Thomas, 2003]. As for MSP, it was shown in Chapter 4 that MSP are unlikely to be charged positively below 1 nm in radii; however, more information is needed to properly model the charging of MSP in this size range.

The second scenario is that NLC particles exist in such large number densities; they deplete the electron density allowing ion attachment to compete with electron attachment. Demonstrated in the high aerosol charge model calculations, the existence of large number densities of NLC particles allows the formation of both a positive and negative charge density. In the high aerosol density charge model calculations there were equal densities of positive and negative particles at radii near 1-2 nm, which is in agreement with the MASS instrument. In addition, as the NLC radii increase, the number density of negative particles remains high as the positive density decreases, again in agreement with the MASS data. However, the charge model was limited to particles larger than 1 nm, so it is difficult to explain the existence of only small positive particles. The small positive population again could be explained by positive condensation nuclei. It could also be explained by a decreased electron attachment rate, allowing the growth of water cluster ions. In order to understand the formation of NLC and the formation of positive and negative charge layers, more measurements are

needed from instruments similar to the MASS instrument. For example, measurements of the charge density of MSP at various solar zenith angles could be used to determine photoemission and photodetachment rates of MSP.

BIBLIOGRAPHY

- Amyx, K., Sternovsky, Z., Knappmiller, S., Robertson, S., Horányi, M., and Gumbel, J., In-situ measurements of smoke particles in the wintertime polar mesosphere between 80 and 85 km altitude, *J. Atmos. Sol. Terr. Phys.*, 70(1), 61-70, 2008.
- Andersson, P. U., and Pettersson, J. B. C., Ionization of water clusters by collisions with graphite surfaces, *Z. Phys. DL At., Mol. Clusters* 41, 57, 1997.
- Balsiger, F., Kopp, E., Friedrich, M., Torkar, K. M., Walchli, U., Witt, G., Positive ion depletion in a noctilucent cloud, *Geophys. Res. Lett.*, 23, 93-96, 1996.
- Bardeen, C.G., Toon, O.B., Jensen, E.J., Marsh, D.R., Harvey, V.L., Numerical simulations of the three-dimensional distribution of meteoric dust in the mesosphere and upper stratosphere, *J. Geophys. Res.*, 113(D17202), doi:10.1029/2007JD009515, 2008.
- Baron, B., Hoover, D., and Williams, F., Vacuum ultraviolet photoelectric emission from amorphous ice, *J. Comp. Phys.*, 68, 1997-1999, 1978.
- Baumgarten, G., Fielder, J., Fricke, K. H., Gerding, M., Hervig, M., Hoffmann, P., Muller, N., Pautet, P.-D., Rapp, M., von Savigny, C., Singer, W., and Thomas, G. E., The noctilucent cloud (NLC) display during the ECOMA/MASS sounding rocket flights on August 3, 2007: morphology on global to local scales, *Ann. Geophys.*, 27, 953-965, 2009.
- Bennett, F. D. G., Hall, J. E., and Dickinson, P. H., D-region electron densities and collision frequencies from Faraday rotation and differential absorption, *J. Atmos. Terr. Phys.*, 34, 1321-1335, 1972.
- Bird, G. A., *Molecular Gas Dynamics and the Direct Simulation of gas Flows*, Oxford University Press, New York, 1994.
- Bird, G. A., Aerodynamic effects on the atmospheric composition measurements from rocket vehicles in the thermosphere, *Planet. Space Sci.* 36, 921, 1988.

- Bjorn, L. G., and Arnold, F., Mass spectrometric detection of precondensation nuclei at the arctic summer mesopause, *Geophys. Res. Lett.*, 8, 1167-1170, 1981.
- Blix, T. A., Bekkeng, J. K., Latteck, Rl., Lübken, F.-J., Rapp, M., Schöch, A., Singer, W., Smiley, B., and Strelnikov, B., Rocket probing of PMSE and NLC – results from the recent MIDAS/MACWAVE campaign, *Adv. Space Res.*, 31(9), 2061-2067, 2003.
- Bohren, C.F. and Hoffman, D.R., *Absorption and Scattering of Light by Small Particles*, Wiley, New York, 1983.
- Brasseur, G., and S. Solomon, *Aeronomy of the Middle Atmosphere*, D. Reidel Publishing Co., Dordrecht, Holland, 1986.
- Brattli, A., Lie-Svendsen, O., Svenes, K., Hoppe, U.-P., Strelnikova, I., Rapp, M., Latteck, R., and Friedrich, M., The ECOMA 2007 campaign: rocket observations and numerical modeling of aerosol particle charging and plasma depletion in a PMSE/NLC layer, *Ann. Geophys.*, 27, 781-796, 2009.
- Burkholder, J., Mills, M., and McKeen, S., Upper limit for the UV absorption cross sections of H₂SO₄, *Geophys. Res. Lett.*, 27, 2493-2496.
- Cho, J. Y. N. and Kelley, M. C., Enhancement of Thomson scatter by charged aerosols in the polar mesosphere: measurements with a 1.29-GHz radar, *Geophys. Res. Lett.*, 19, 1097-1100, 1992.
- Cho, J. Y. N. and Röttger, J., An updated review of polar mesosphere summer echoes: observation, theory, and their relationship to noctilucent clouds and subvisible aerosols, *J. Geophys. Res.*, 102, 2001-2020, 1997.
- Croskey, C., Mitchell, J., Friedrich, M., Schmidlin, F.J., Meriwether, J.W., Initial results of a rocket-based study of gravity wave effects on photoionization in the middle atmosphere, *Adv. Space Res.*, 32(5), 741-746, 2003.
- Croskey, C., Mitchell, J., Friedrich, M., Torkar, K., Hoppe, U.-P., and Goldberg, R., Electrical structure of PMSE and NLC regions during the DROPPS program, *Geophys. Res. Lett.*, 28, 1427-1430, 2001.
- Croskey, C. L., Mitchell, J. D., Goldber, R. A., Blix, T. A., Rapp, M., Latteck, R., Friderich, M., and Smiley, B., Corrdinated investigation of plasma and neutral density fluctuations and particles during the MacWAVE/MIDAS summer 2002 program, *Geophys. Res. Lett.*, 31, L24S08, doi:10.1029/2004GL020169, 2004.

- Deland, M. T., Shettle, E. P., Thomas, G. E., and Olivero, J. J., A quarter-century of satellite polar mesospheric cloud observations, *J. Atmos. Sol. Terr. Phys.*, 68, doi:10.1016/j.jastp.2005.08.003, 2006.
- Deland, M. T., Shettle, E. P., Thomas, G. E., and Olivero, J. J., Latitude-dependent long-term variations in polar mesospheric clouds from SBUV version 3 PMC data, *J. Geophys. Res.*, 112, D10315, doi:10.1029/2006JD007857, 2007.
- do Couto, P. C., Cabral, B. J. C., and Canuto, S., Electron binding energies of water clusters: implications for the electronic properties of liquid water, *Chem. Phys. Lett.*, 429, 129-135, doi:doi:10.1016/j.cplett.2006.08.046, 2006.
- Draine, B. T., and Sutin, B., Collisional charging of interstellar dust grains, *Astrophys. J.*, 320, 803-817, 1987.
- Epstein, P. S., On the Resistance Experienced by Spheres in Their Motion Through Gases, *Phys. Rev.* 23, 710, 1924.
- Feuerbacher, B., and Fitton, B., Experimental investigation of photoemission from satellite surface materials, *J. Appl. Phys.*, 43, 1563-1572, 1972.
- Friedrich, M., Torkar, K. M., Goldberg, R. A., Mitchell, J. D., Croskey, C. L., and Lehmacher, G., *Proceedings of the 13th ESA Symposium on European Rocket and Balloon Programmes and Related Research*, ESA paper No. SP-397, 381, 1997.
- Friedrich, M., Torkar, K. M., Singer, W., Strelnikova, I., Rapp, M., and Robertson, S., Signature of mesospheric particles in ionospheric data, *Ann. Geophys.*, 27, 823-829, 2009.
- Gordley, L. L., Hervig, M. E., Fish, C., Russell, J. M., Bailey, S., Cook, J., Hansen, S., Shumway, A., Paxton, G., Deaver, L., Marshall, T., Burton, J., Magill, B., Brown, C., Thompson, E., and Kemp, J., The solar occultation for ice experiment, *J. Atmos. Sol. Terr. Phys.*, 71, 300-315, doi:10.1016/j.jastp.2008.08.012, 2009.
- Gumbel, J., and Megner, L., Charged meteoric smoke as ice nuclei in the mesosphere: part 1-a review of basic concepts, *J. Atmos. Sol. Terr. Phys.*, 71, 1225-1235, 2009.
- Gumbel, J., Siskin, D. E., Witt, G., Torkar, K. M., and Friedrich, M., Influences of ice particles on the ion chemistry of the polar summer mesosphere, *J. Geophys. Res.*, 108, D8, 8436-8452, 2003.
- Gumbel, J., and Witt, G., Rocket-borne photometry of NLC particle populations, *Adv. Space Res.*, 28(7), 1053-1058, 2001.

- Havnes, O., and Næsheim, L. I., On the secondary charging effects and structure of mesospheric dust particles impacting on rocket probes, *Ann. Geophys.*, 25, 623, 2007.
- Hayes, W. D., and Probstein, R. F., *Hypersonic Flow Theory*, Academic, New York, Chapter 10.3, 1959.
- Hedin, J., et al., On the efficiency of rocket-borne particle detection in the mesosphere, *Atmos. Chem. Phys.*, 7, 3701-3711, 2007.
- Hervig, M. E., Gordley, L. L., Stevens, M. H., Russell, J. M., Bailey, S. M., and Baumgarten, G., Interpretation of SOFIE PMC measurements: Cloud identification and derivation of mass density, particle shape, and particle size, *J. Atmos. Sol. Terr. Phys.*, Vol. 71, 316-330, doi:10.1016/j.jastp.2008.07.009, 2009.
- Holzworth, R. H. and R. A. Goldberg, Electric field measurements in noctilucent clouds, *J. Geophys. Res.*, 109, D16203, 2004.
- Holzworth, R. H., Pfaff, R. F., Goldberg, R. A., Bounds, S. R., Schmidlin, F. J., Voss, H. D., Tuzzolino, A. J., Croskey, C. L., Mitchell, J. D., von Cossart, G., Singer, W., Hoppe, U.-P., Murtagh, D., Witt, G., Gumbel, J., and Friedrich, M., Large electric potential perturbations in PMSE during DROPPS, *Geophys Res. Lett.*, 28, 1435-1438, 2001.
- Horányi, M., et al., Simulation of Rocket-Borne Particle Measurements in the Mesosphere, *Geophys. Res. Lett.*, 26(11), 1537-1540, 1999.
- Horányi, M., Hoxie, V., James, D., Poppe, A., Bryant, C., Grogan, B., Lamprecht, B., Mack, J., Bagenal, F., Batiste, S., Bunch, N., Chantanowich, T., Christensen, F., Colgan, M., Dunn, T., Drake, G., Fernandez, A., Finley, T., Holland, G., Jenkins, A., Krauss, C., Krauss, E., Krauss, O., Lankton, M., Mitchell, C., Neeland, M., Resse, T., Rash, K., Tate, G., Vaudrin, C., Westfall, J., The student dust counter on the new horizons mission, *Space Sci. Rev.*, 10.1007/s11214-00709250-y, 2007.
- Hunten, D.M., Turco, R.P., Toon, O.B., Smoke and dust particles of meteoric origin in the mesosphere and stratosphere, *J. Atmos. Sci.* 37, 1342-1357, 1980.
- Jacobsen, T. A., and Friedrich, M., Electron density measurements in the lower D-region, *J. Atmos. Terr. Phys.*, 41(12), 1195-1200, 1979.
- Jensen, E. and Thomas, G. E., Charging of mesospheric particles: implications of electron density and particle coagulation, *J. Geophys. Res.*, 96, 18603-18615, 1973.

- Karlsson, B., Randall, C. E., Benze, S., Mills, M., Harvey, V. L., Bailey, S. M., and Russell III, J. M., Intra-seasonal variability of polar mesospheric clouds due to inter-hemispheric coupling, *Geophys. Res. Lett.*, 36, L20802, doi:10.1029/2009GL040348, 2009.
- Keesee, R.G., Nucleation and particle formation in the upper atmosphere, *J. Geophys. Res.* 94, 14683-14692, 1989.
- Keneshea, T. J., Narcisi, R. S., and Swider, W., Diurnal model of the E region, *J. Geophys. Res.*, 75, 845, 1970.
- Knappmiller, S., Robertson, S., Sternovsky, Z., and Friedrich, M., A rocket-borne mass analyzer for charged aerosol particles in the mesosphere, *Rev. Sci. Instrum.*, 79, 1, 2008.
- Knappmiller, S., Rapp, M., Robertson, S., and Gumbel, J., Charging of meteoric smoke and ice particles in the mesosphere including photoemission and photodetachment rates, *J. Atmos. Solar Terr. Phys.*, in press.
- Latteck, R., Singer, W., and H. Bardey, The ALWIN MST Radar – Technical Design and Performance, *Proceedings of the 14th ESA Symposium on European Rocket and Balloon Programmes and Related Research*, ESA SP-437, 179-184, 1999.
- Leu, M.T., Biondi, M.A., and Johnson, R., Measurements of the recombination of electrons with $H_3O^+(H_2O)_n$ -series ions, *Phys. Rev. A*, 7, 292-298, 1973.
- Lübken, F.-J., Thermal Structure of the Arctic Summer Mesosphere, *J. Geophys. Res.*, 104, 9135-9149, 1999.
- Mechtly, E. A., Accuracy of rocket measurements of lower ionosphere electron density concentration, *Radio Sci.*, 9, 373-378, 1974.
- Mechtly, E. A., Bowhill, S. A., Smith, L. G., and Knoebel, H. W., Lower ionosphere electron concentrations and collision frequency from rocket measurements of Faraday rotation, differential absorption, and probe current, *J. Geophys. Res.*, 72, 5239-5245, 1967.
- Megner, L., and Gumbel, J., Charged meteoric smoke as ice nuclei in the mesosphere: Part 2-A feasibility study, *J. Atmos. Solar-Terr. Phys.*, 71, 1236-1244, 2009.
- Megner, L., Gumbel, J., Rapp, M., and Siskind, D.E., Reduced meteoric smoke particle density at the summer pole-implications for mesospheric ice particle nucleation, *Adv. in Space Res.* 41, 41-49, 2008.

- Megner, L., Khaplanov, M., Baumgarten, G., Gumbel, J., Stegman, J., Strelnikov, B., and Robertson, S., Large mesospheric ice particles at exceptionally high altitudes, *Ann. Geophys.*, 27, 943-951, 2009.
- Mills, M.J., Toon, O.B., Thomas, G.E., Mesospheric sulfate aerosol layer, *J. Geophys. Res.*, 110, D24208, 2005.
- Mitchell, J.D. and Croskey, C.L., Electrical structure of Noctilucent cloud and polar mesosphere summer echo regions, *Adv. Space Res.*, 28, 1027-1036, 2001.
- Mott-Smith, H. M., and Langmuir, I., The Theory of Collectors in Gaseous Discharges, *Phys. Rev.* 28, 727-763, 1926.
- Murray, B. J., and Jensen, E. J., Homogeneous nucleation of amorphous solid water particles in the upper mesosphere, *J. Atmos. Solar-Terr. Phys.*, 72, 51-61, 2010.
- Natanson, G.L., On the theory of the charging of amicroscopic aerosol particles as a result of capture of gas ions, *Sovient Physics Technical Physics* 5, 538-551, 1960.
- Pedersen, A., Tröim, J., and Kane, J. A., Rocket measurements showing removal of electrons above the mesopause in summer at high latitude, *Planet. Space Sci.*, 18, 945-947, 1970.
- Press, W. H., Teukolsky, S. A., Vetterling, W. T., and Flannery, B. P., Numerical Recipes, Cambridge University Press, Cambridge, England, 2007.
- Probstein, R. F., Society for Industrial and Applied Mathematics (SIAM), J. W. Arrowsmith, Ltd. Bristol, England, 1969.
- Pueschel, R., Verma, S., Rohatschek, H., Ferry, G., Boiadjieva, N., Howard, S., Strawa, A., Vertical transport of anthropogenic soot aerosol into the middle atmosphere, *J. Geophys. Res.* 105, 3727-3736, 2000.
- Rapp, M., Charging of mesospheric aerosol particles: the role of photodetachment and photoionization from meteoric smoke and ice particles, *Ann. Geophys.*, 27, 2417-2422, 2009.
- Rapp, M., et al., Observations of Positively Charged Nanoparticles in the Nighttime Polar Mesosphere, *Geophys. Res. Lett.*, 32, L23821, 2005.
- Rapp, M., and Lübken, F.-J., Modeling of particle charging in the polar summer mesosphere: Part 1 – general results, *J. Atmos. Sol. Terr. Phys.*, 63, 759-770, 2001.

- Rapp, M., and Lübken, F.-J., Polar mesosphere summer echoes (PMSE): review of observations and current understanding, *Atmos. Chem. and Phys.*, 4, 2601-2633, 2004.
- Rapp, M., Strelnikova, I., and Gumbel, J., Meteoric smoke particles: evidence from rocket and radar techniques, *Adv. Space Res.*, 40, doi:10.1016/j.asr.2006.11.021, 809-817, 2007.
- Rapp, M., Strelnikova, I., Strelnikov, B., Latteck, R., Baumgarten, G., Li, Q., Megner, L., Gumbel, J., Friedrich, M., Hoppe, U.-P., Robertson, S., First in situ measurement of the vertical distribution of ice volume in a mesospheric ice cloud during the ECOMA/MASS rocket-campaign, *Ann. Geophys.*, 27, 755-766, 2009.
- Rapp, M., and Thomas, G. E., Modeling the microphysics of mesospheric ice particles: assessment of current capabilities and basic sensitivities, *J. Atmos. Sol. Terr. Phys.*, 68, 715-744, 2006.
- Rapp, M., Thomas, G. E., and Baumgarten, G., Spectral properties of mesospheric ice clouds: evidence for nonspherical particles, *J. Geophys. Res.*, 112, D03211, doi:10.1029/2006JD007322, 2007.
- Rinsland, C.P., Gunson, M. R., Ko, M. K. W., Weisensten, D. W., Zander, R., Abrams, M. C., Goldman, A., Sze, N. D., and Yue, G. K., H₂SO₄ photolysis: A source of sulfur dioxide in the upper stratosphere, *Geophys. Res. Lett.*, 22, 1109-1112, 2003.
- Robertson, S., Horányi, M., Knappmiller, S., Sternovsky, Z., Holzworth, R., Shimogawa, M., Friedrich, M., Torkar, K., Gumbel, J., Megner, L., Baumgarten, G., Latteck, R., Rapp, M., Hoppe, U.-P., and Hervig, M.E., Mass analysis of charged aerosol particles in NLC and PMSE during the ECOMA/MASS campaign, *Ann. Geophys.*, 27, 1213-1232, 2009.
- Robertson, S., and Sternovsky, Z., Monte Carlo Method of Ion Mobility and diffusion for Low and High Electric Fields, *Phys. Rev. E* 67, 046405, 2003.
- Rusch, D. W., Thomas, G. E., McClintock, W., Merkel, A. W., Bailey, S. M., Russell III, J. M., Randall, C. E., Jeppesen, C., and Callan, M., The Cloud Imaging and Particle Size experiment on the Aeronomy of Ice in the Mesosphere Mission: cloud morphology for the northern 2007 season, *J. Atmos. Solar-Terr. Phys.*, doi:10.1016/j.jastp.2008.11.005, 2009.
- Seele, C., and Hartogh, P., Water vapor of the polar middle atmosphere: annual variation and summer mesosphere conditions as observed by ground-based microwave spectroscopy, *Geophys. Res. Lett.*, 26, 1517-1520, 1999.

- Smiley, B., Rapp, M., Blix, T. A., Robertson, S., Horányi, M., Latteck, R., and Fiedler, J., Charge and size distribution of mesospheric aerosol particles measured inside NLC and PMSE during MIDAS MaCWAVE 2002, *J. Atmos. Sol. Terr. Phys.*, 68, 114-123, 2006.
- Smiley, B., Robertson, S., Horányi, M., Blix, T., Rapp, M., Latteck, R., and Gumbel, J., Measurement of positively and negatively charged particles inside PMSE during MIDAS SOLSTICE 2001, *J. Geophys. Res.*, vol. 108, 8444-8454, 2003.
- Sternovsky, Z., Holzworth, R. H., Horányi, M., and Robertson, S., Potential distribution around sounding rockets in mesospheric layers with charged aerosol particles, *Geophys. Res. Lett.*, 31, L22101, 2004.
- Sternovsky, Z., Horányi, M., and S. Robertson, Collision cross sections of small water clusters, *Phys. Rev. A* 64, 023203, 2001.
- Thomas, G. E., Is the polar mesosphere the miner's canary of global change?, *Adv. Space Res.*, 18(3), 149-158, 1996.
- Thomas, G. E., and Olivero, J. J., Noctilucent clouds as possible indicators of global change in the mesosphere, *Adv. Space Res.*, 28, 937-946, 2001.
- Turco, R. P., Toon, O. B., Whitten, R. C., Keesee, R. G., and Hollenbach, D., Noctilucent clouds: simulation studies of their genesis, properties, and global influences, *Planet. Space Sci.*, 30(11), 1147-1181, doi:10.1016/0032-0633(82)90126-X, 1982.
- Ulwick, J. C., Baker, K. D., Kelley, M. C., Balsley, B. B., and Ecklund, W. L., Comparison of simultaneous MST radar and electron density probe measurements during STATE, *J. Geophys. Res.*, 93(D6), 6986-7000, 1988.
- Viehland, L. A. and E. A. Mason, Transport Properties of Gaseous Ions over a Wide Energy Range, IV., *Atomic Data and nuclear Data Tables*, Vol. 60, Issue 1, 37-95, 1995.
- von Cossart, G., Fiedler, J., and von Zahn, U., Size distributions of NLC particles as determined from 3-color observations of NLC by ground-based lidar, *Geophys. Res. Lett.*, 26(11), 1513-1316, 1999.
- Vondrak, T., Plane, M. M. C., and Meech, S.R., Photoemission from sodium on ice: a mechanism for positive and negative charge coexistence in the mesosphere, *Phys. Chem. B Lett.*, 110, 3860-3863, 2006.

- von Zahn, U., Are Noctilucent clouds truly a “miner’s canary” for global change?, *Eos Trans. AGU*, 84(28), 2003.
- von Zahn, U., von Cossart, G., Fiedler, J., Fricke, K. H., Nelke, G., Baumgarten, G., Rees, D., Hauchecorne, A., and K. Adolfsen, The ALOMAR Rayleigh/Mie/Raman lidar: objectives, configuration, and performance, *Ann. Geophys.* 18, 815-833, 2000.
- Vostrikov, A. A., Yu Dubov, D., and Predtechenskiy, M. R., Ionization of water clusters by surface collision, *Chem. Phys. Lett.* 139, 124, 1987.
- Wang, L. S., Wu, H., and Desai, S. R., Sequential oxygen atom chemisorption on surfaces of small iron clusters, *Phys. Rev. Lett.*, 76, 4853-4856, 1996.
- Warren, S. G., Optical constants of ice from the ultraviolet to the microwave, *Appl. Optics*, 23, 1206-1225, 1984.
- Witt, G., The nature of noctilucent clouds, *Space Res.* 9, 157-169, 1969.
- Yang, X., and Castleman, A. W., Temperature and cluster size dependence studies of reactions of protonated water clusters with acetonitrile, *J. Chem. Phys.*, 95, 1, 130-135, 1991.

APPENDIX A: AERODYNAMIC SIMULATION RESULTS

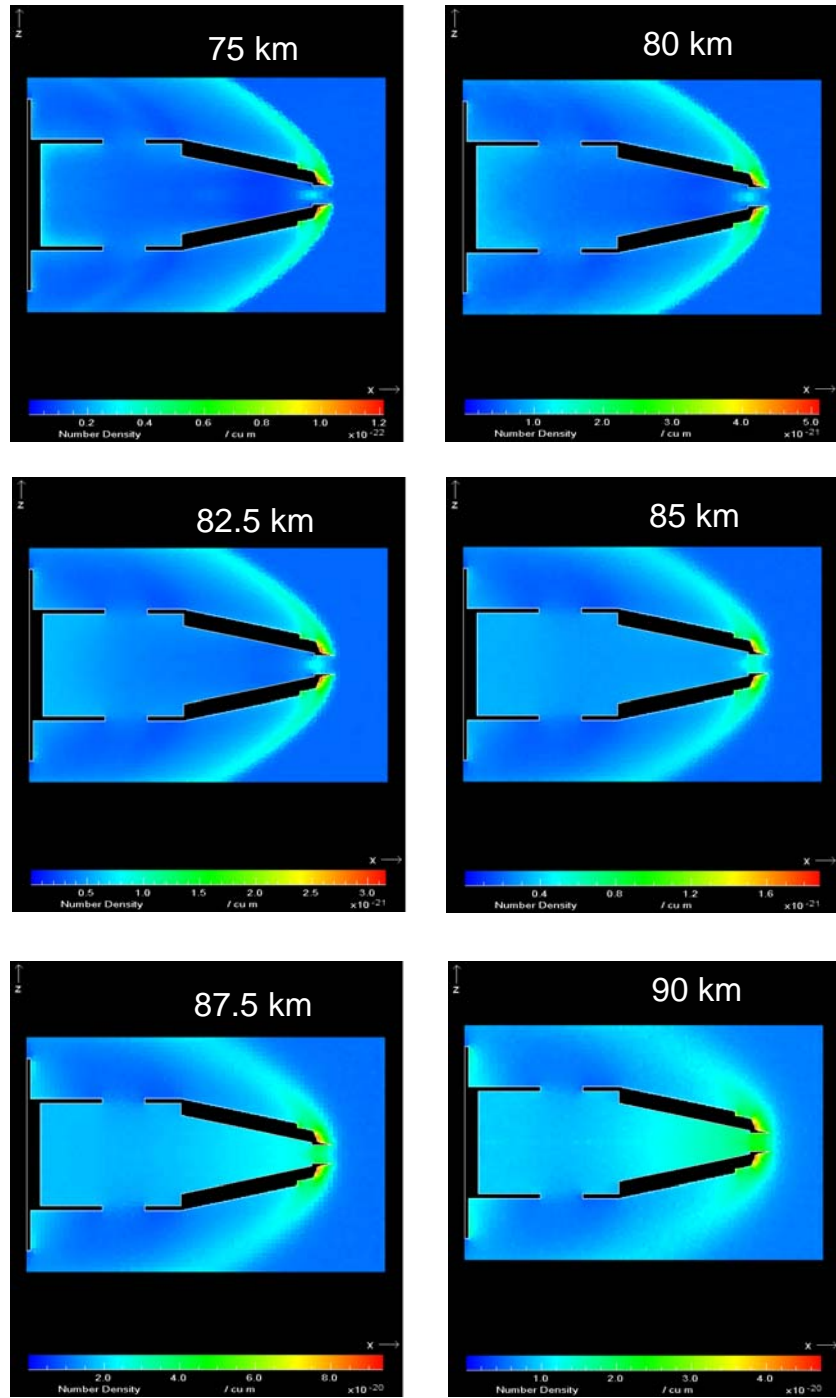


Figure 27. The number density results from the DSMC calculations for all 6 altitudes. The plot is a 2-D slice through the MASS instrument. Note: the scale differs on each graph.

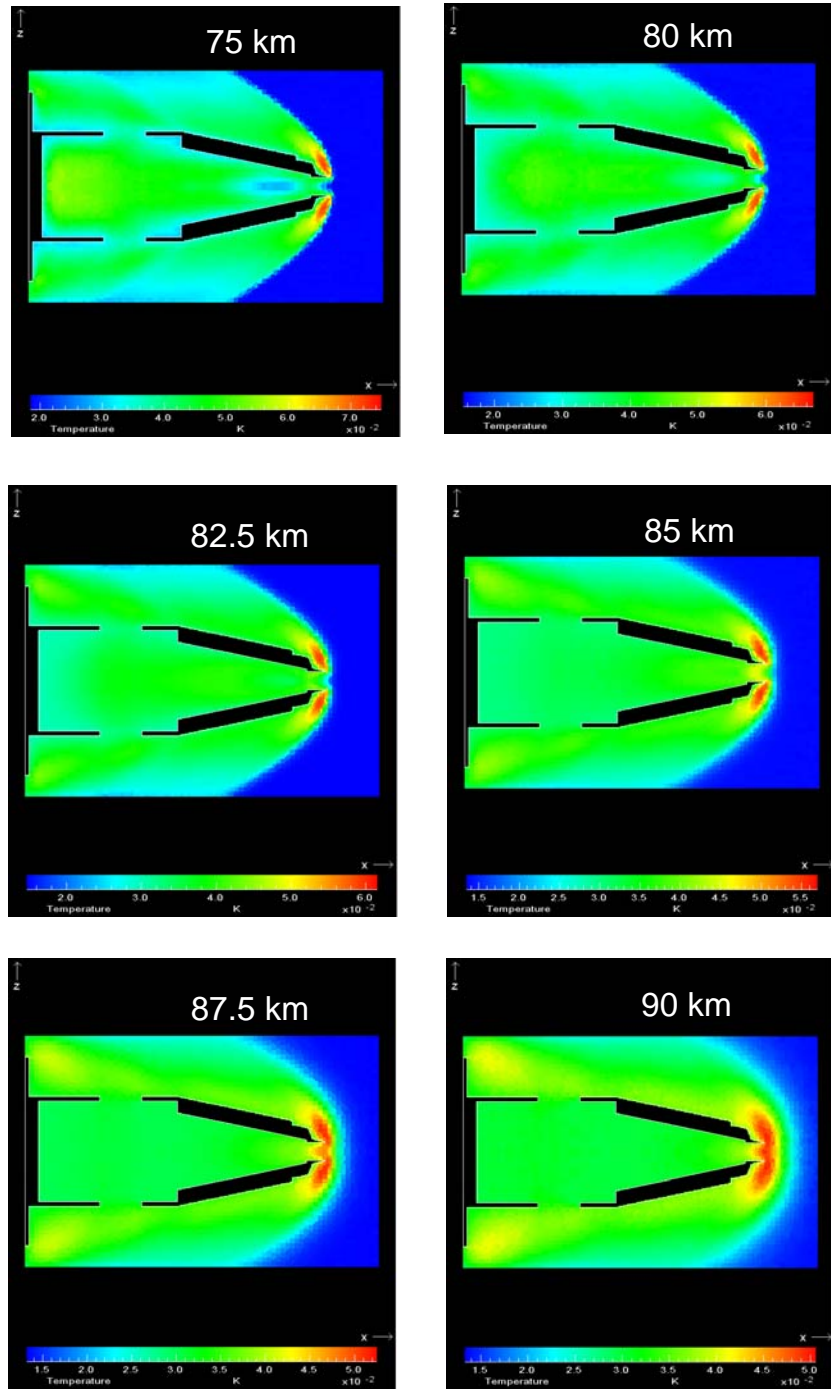


Figure 28. The temperature results from the DSMC calculations for all 6 altitudes. The plot is a 2-D slice through the MASS instrument. Note: the scale differs on each graph.

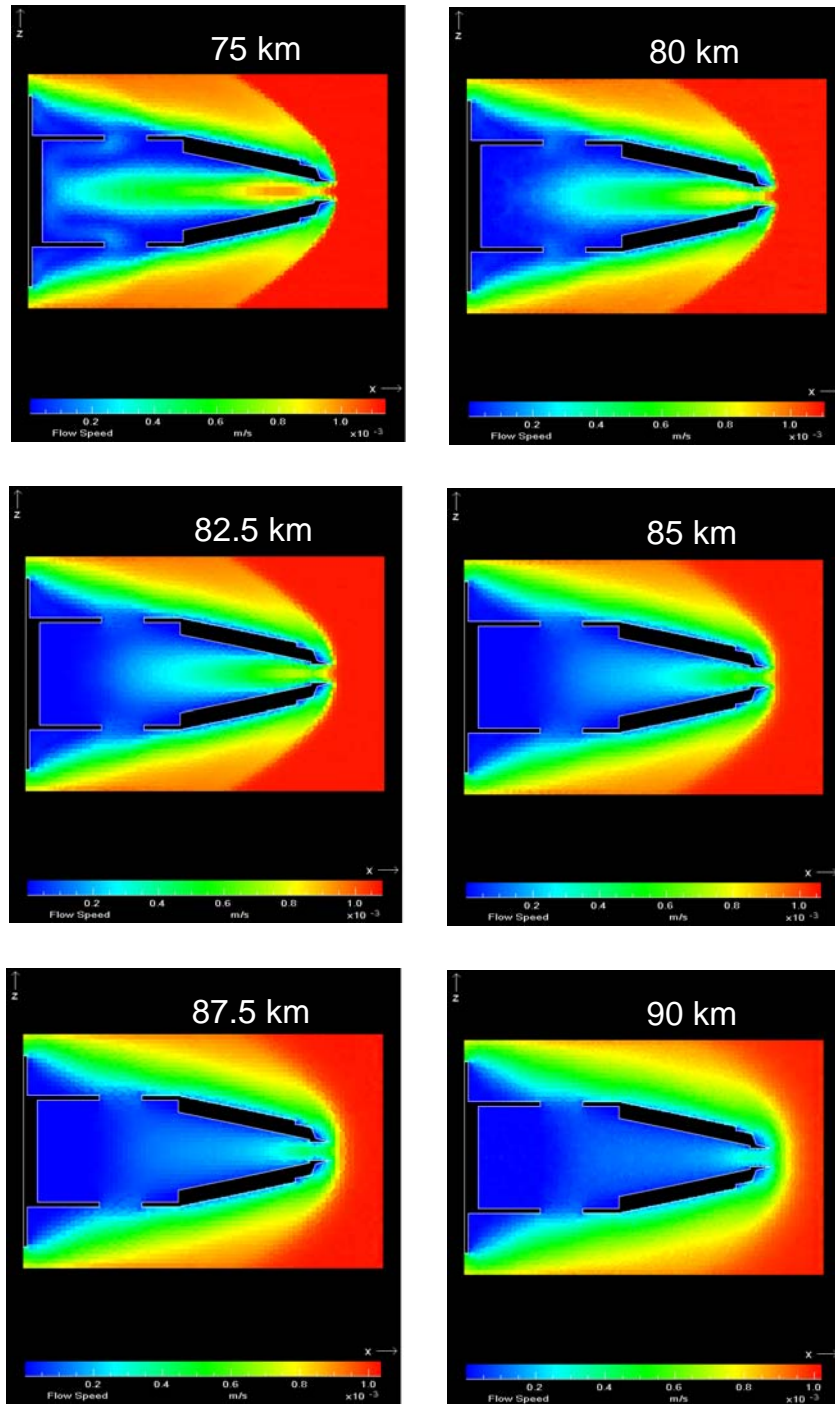


Figure 29. The air flow speed results from the DSMC calculations for all 6 altitudes. The plot is a 2-D slice through the MASS instrument. Note: the scale differs on each graph.

APPENDIX B: MASS CALIBRATION RESULTS

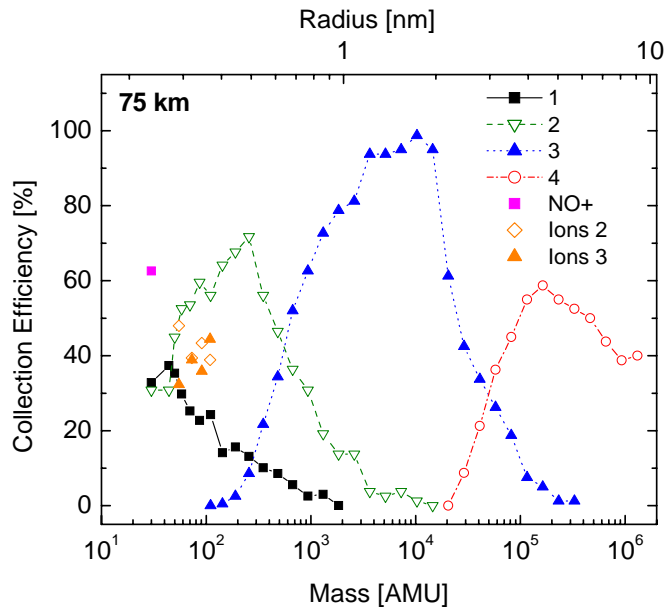


Figure 30. Calibration curves for an altitude of 75 km.

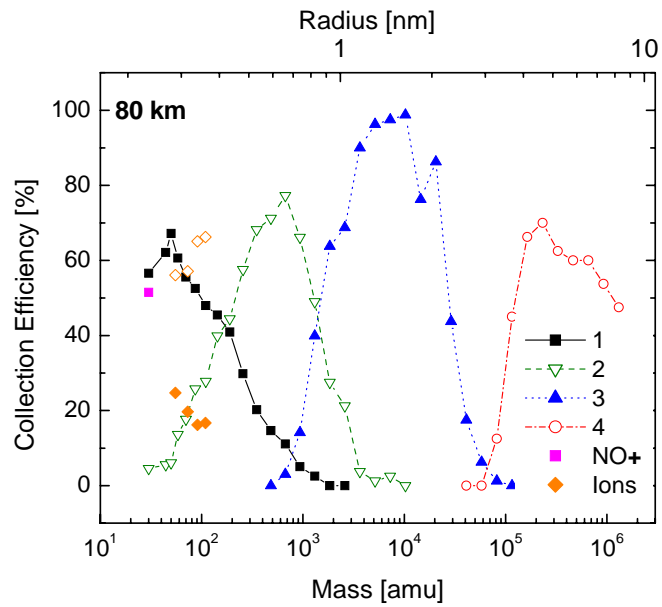


Figure 31. Calibration curves for an altitude of 80 km.

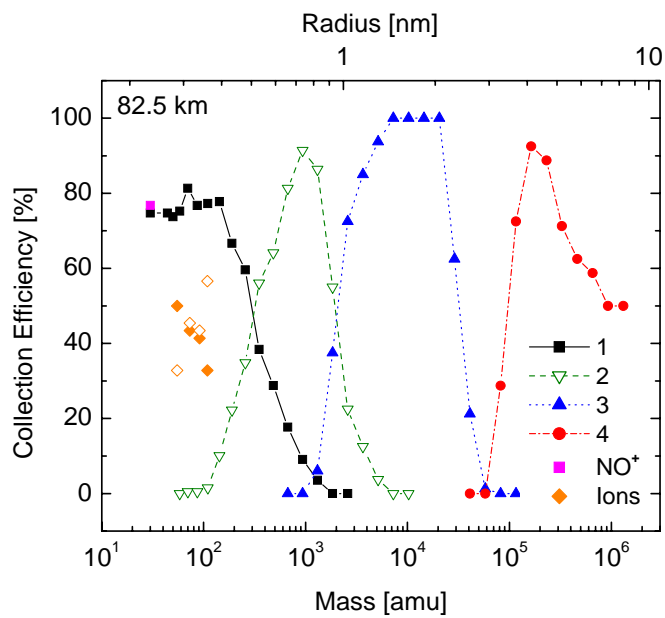


Figure 32. Calibration curves for an altitude of 82.5km.

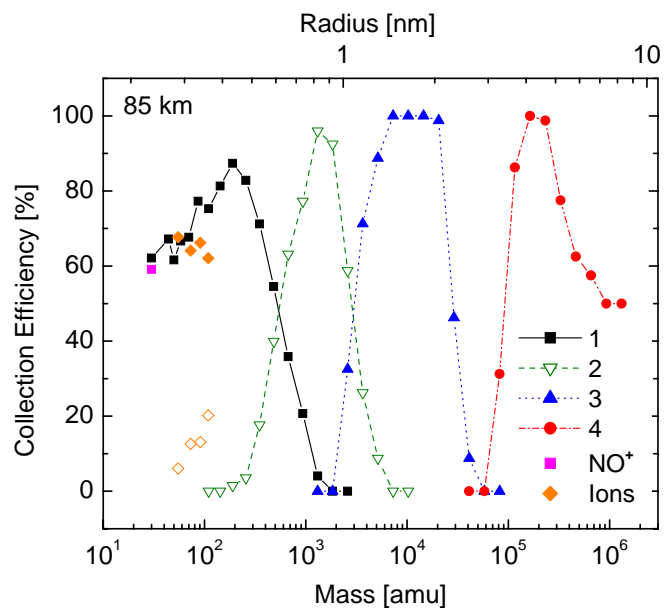


Figure 33. Calibration curves for an altitude of 85km.

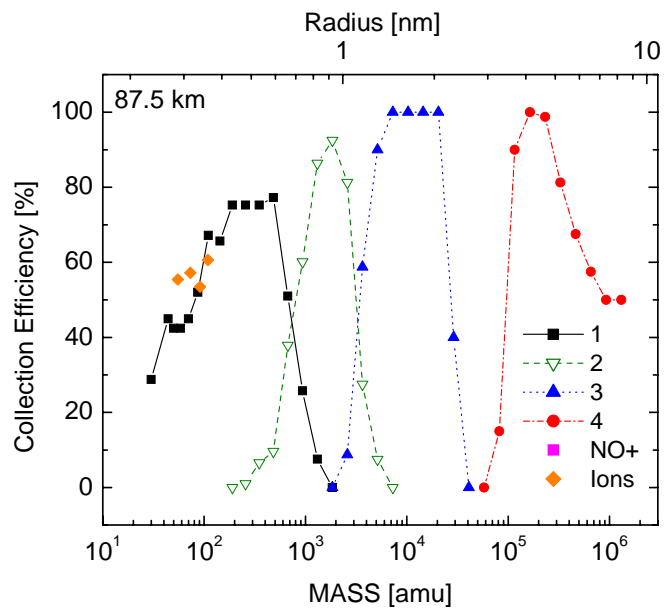


Figure 34. Calibration curves for an altitude of 87.5 km.

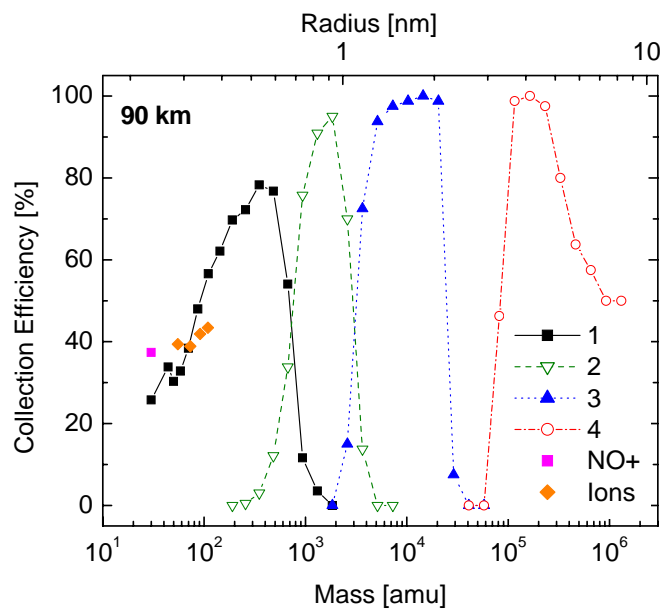


Figure 35. Calibration curves for an altitude of 90 km.

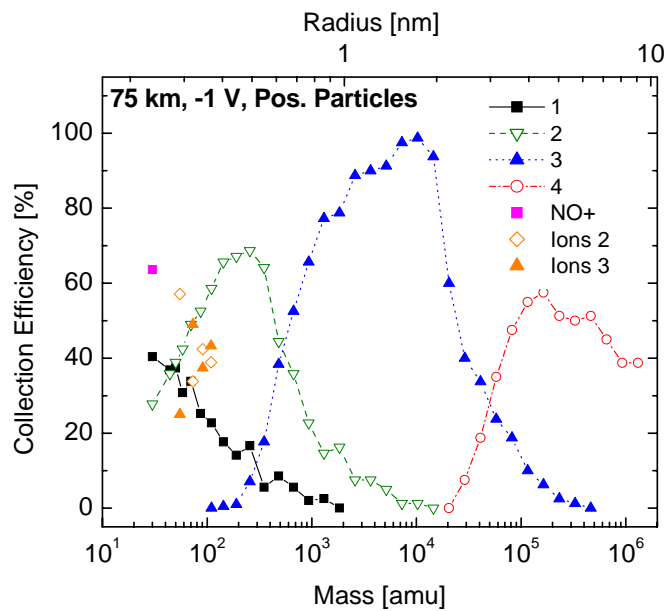


Figure 36. Calibration curves for positive particles at an altitude of 75 km with a payload potential of -1 V.

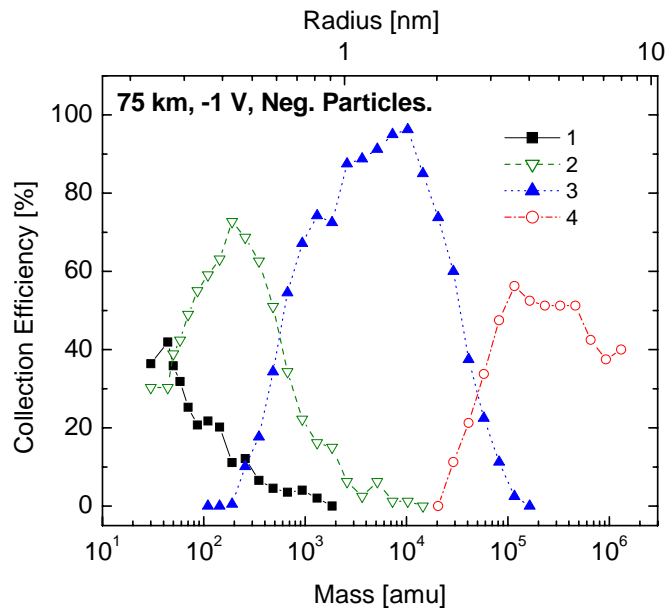


Figure 37. Calibration curves for negative particles at an altitude of 75 km with a payload potential of -1 V.

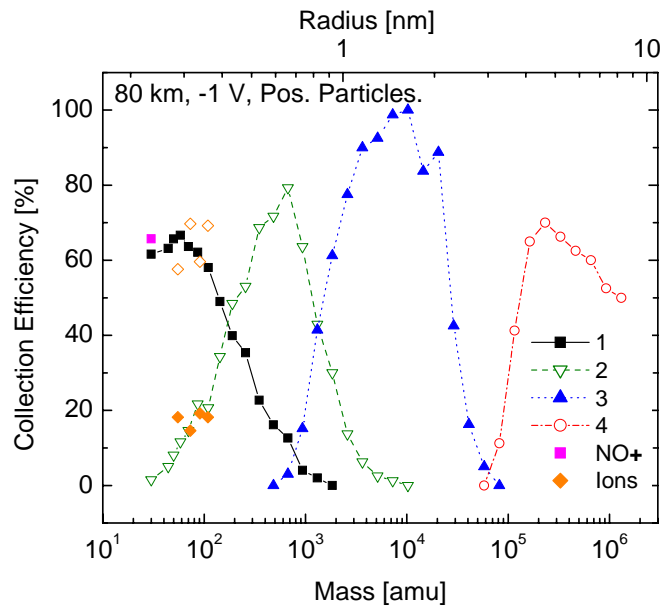


Figure 38. Calibration curves for positive particles at an altitude of 80 km with a payload potential of -1 V.

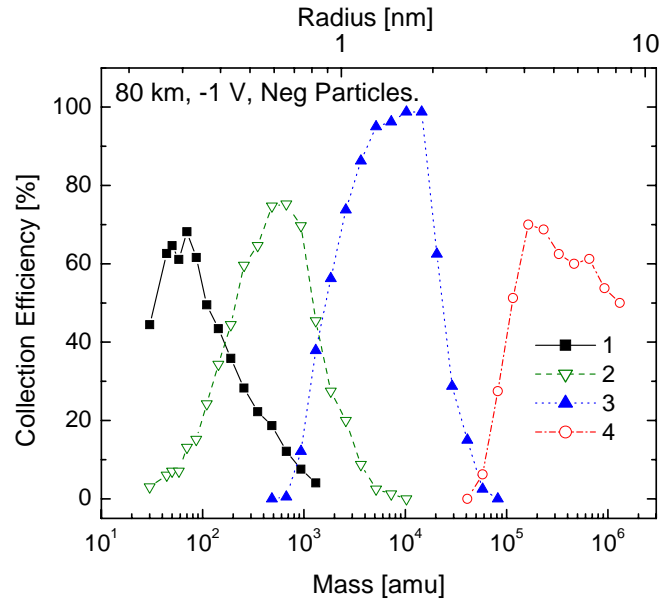


Figure 39. Calibration curves for negative particles at an altitude of 80 km with a payload potential of -1 V.

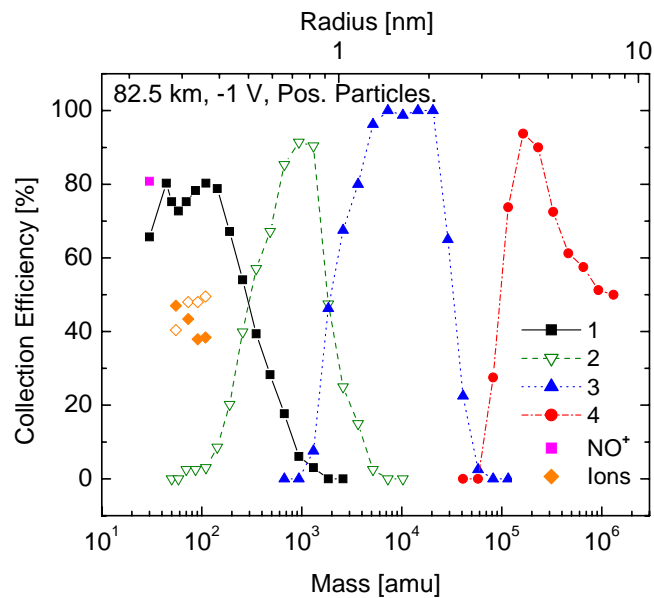


Figure 40. Calibration curves for positive particles at an altitude of 82.5 km with a payload potential of -1 V.

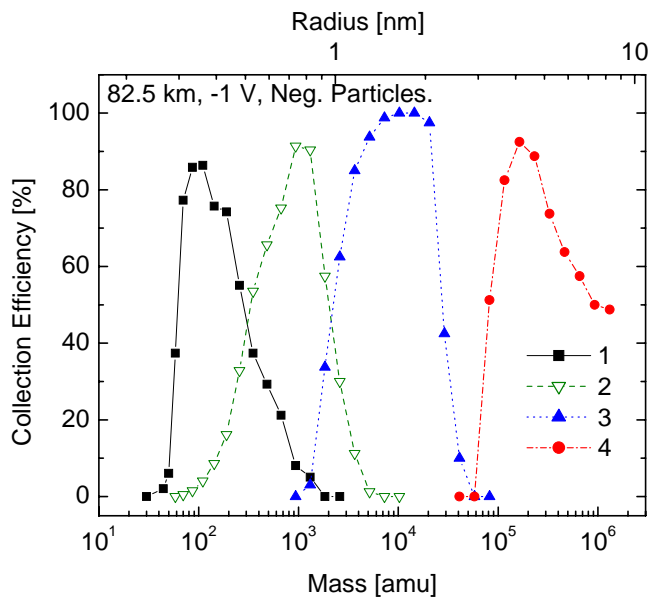


Figure 41. Calibration curves for negative particles at an altitude of 82.5 km with a payload potential of -1 V.

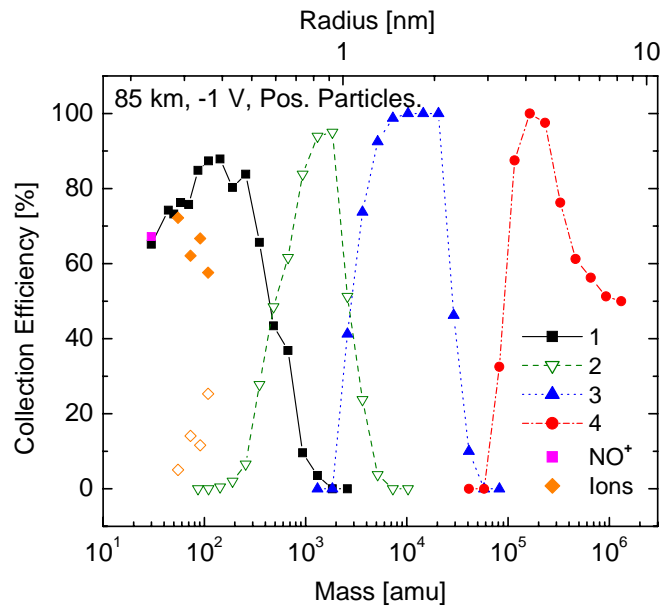


Figure 42. Calibration curves for positive particles at an altitude of 85 km with a payload potential of -1 V.

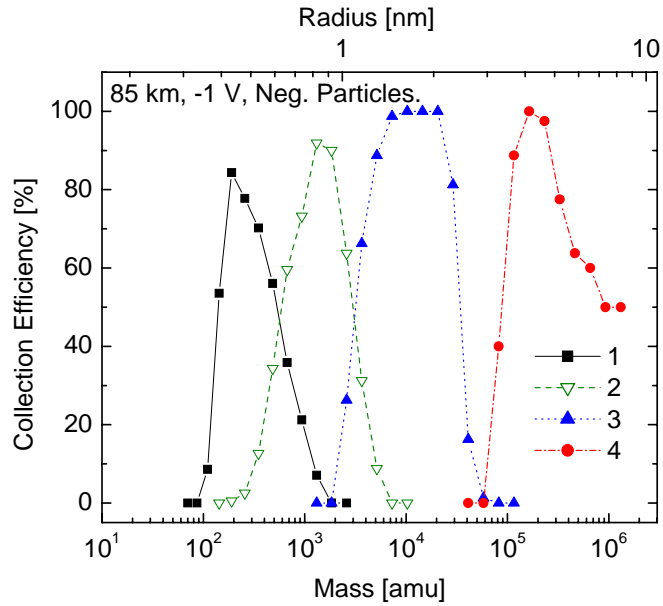


Figure 43. Calibration curves for negative particles at an altitude of 85 km with a payload potential of -1 V.

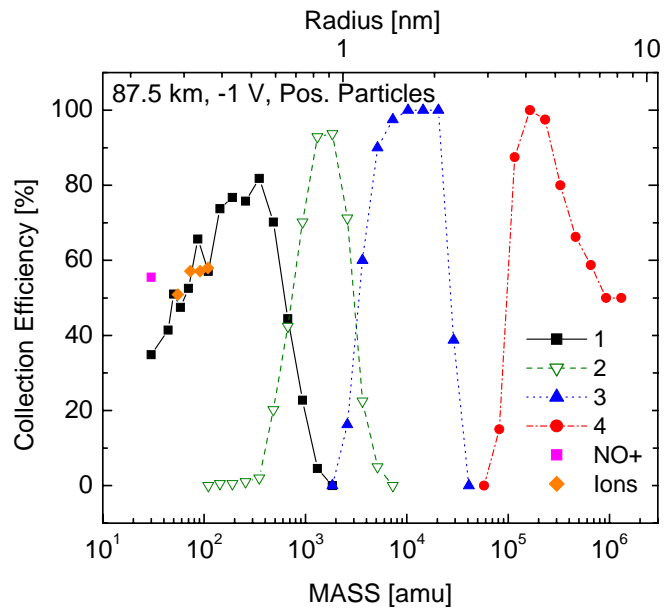


Figure 44. Calibration curves for positive particles at an altitude of 87.5 km with a payload potential of -1 V.

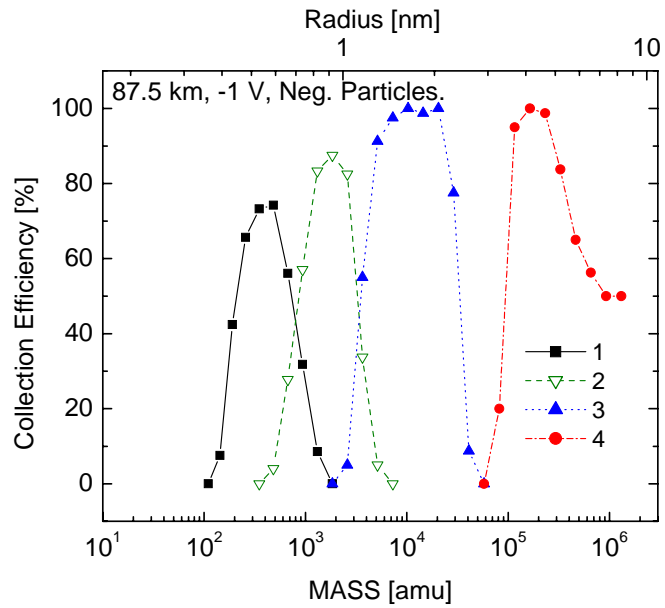


Figure 45. Calibration curves for negative particles at an altitude of 87.5 km with a payload potential of -1 V.

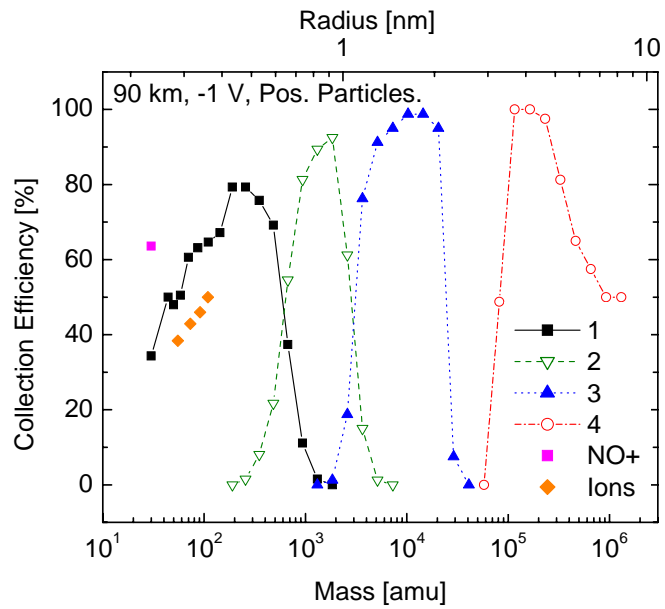


Figure 46. Calibration curves for positive particles at an altitude of 90 km with a payload potential of -1 V.

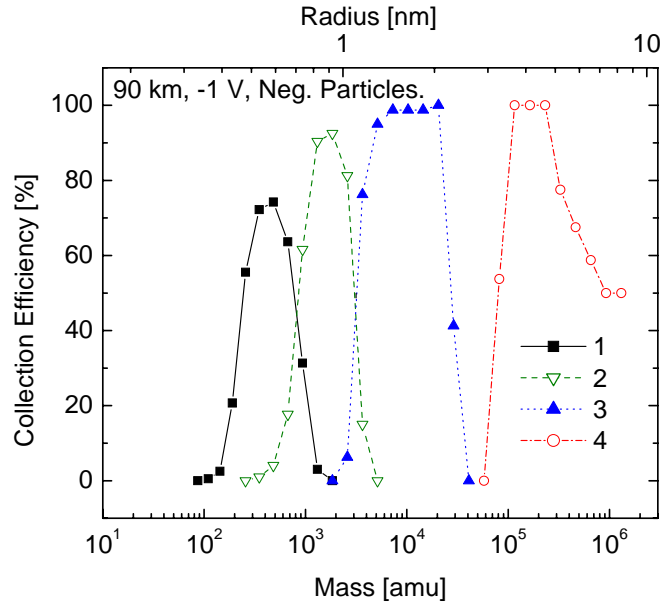


Figure 47. Calibration curves for negative particles at an altitude of 90 km with a payload potential of -1 V.